Role of impurity deposition in the formation of silicon nanocone by using low energy helium plasma irradiation

A thesis submitted to

Nagoya University

for the degree of Doctor of Engineering

in Electrical Engineering

By

Quan Shi

Graduate School of Engineering

Nagoya University

Nagoya, Japan

June 2021

Contents

Chapter 1. Introduction

1.1 Energy crisis and global warming

As the development of the modern world becomes faster, energy issue has been raised up as a crisis. The release of greenhouse gas from the consumption fossil fuel has contributed to increasing of the average surface temperature of this planet for 1.18 degrees Celsius since the late 19th century, as shown in figure 1.1 [1]. One of the promising renewable and harmless sources is the solar energy. The global solar energy consumption has been raised from 0.06% to 1.1% since 2000 [2]. However, there is still a far way to meet the goal of carbon neutrality which humans expect to achieve the goal by the mid-century. Thus, it is in high demand to improve the fabricating technique of solar cells and promote the usage of the technique. One of the conventional methods to suppress the reflectance is coating an antireflection layer above the silicon (Si) substrate [3]. However, the reflection loss from the coating layer cannot be ignored and the manufacture of this layer is expensive because of the requirement of high precision. Surface texturing with nanocone structure on the Si substrate (so called black Si) is another method to reduce the optical loss due to the multiple reflections of light among the nanocone. This is a promising method to increase the solar energy conversion efficient without the deposition of an antireflection layer [4–7].

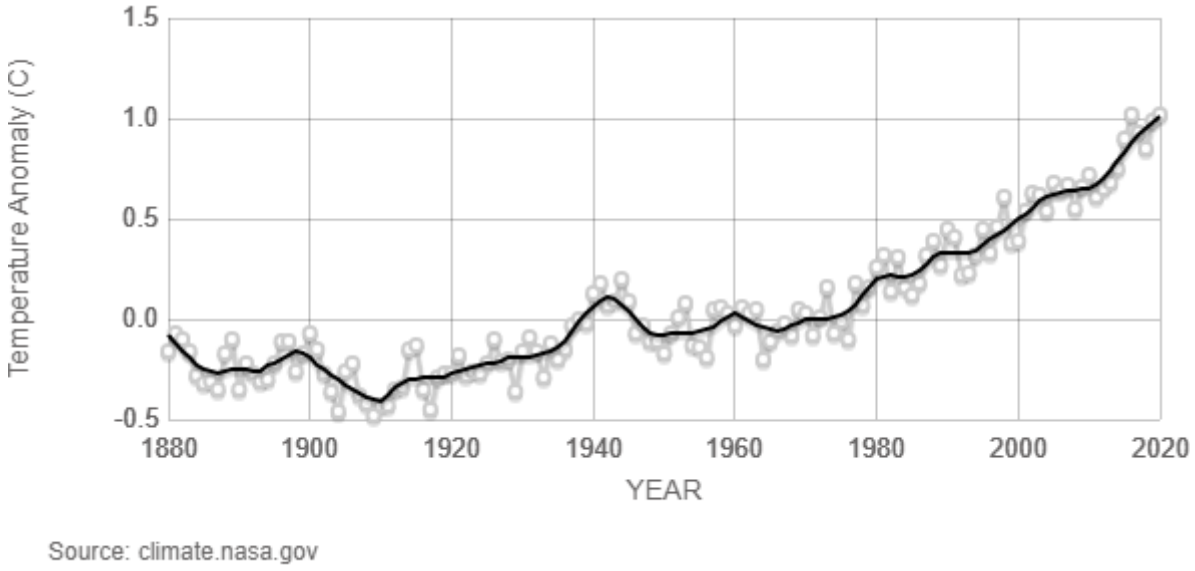

Figure 1.1 The change in global surface temperature from 1880 to 2020 relative to 1951–1980 average temperatures [1].

1.2 Application of Si-nanocone (NCs)

Nanocone structure is a conical structure with a size of 0.1 to 10 μm, as shown in figure 1.2. It can be fabricated on many materials to improve the physical or optical performance. To improve properties of the material, density of nanocone laid on the surface is usually over 10 μm^{-2}.

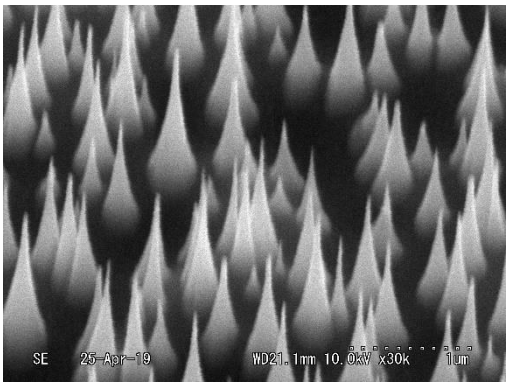

Figure 1.2 A scanning electron micrograph of nanocone structure on silicon surface in a tilted view of 30°.

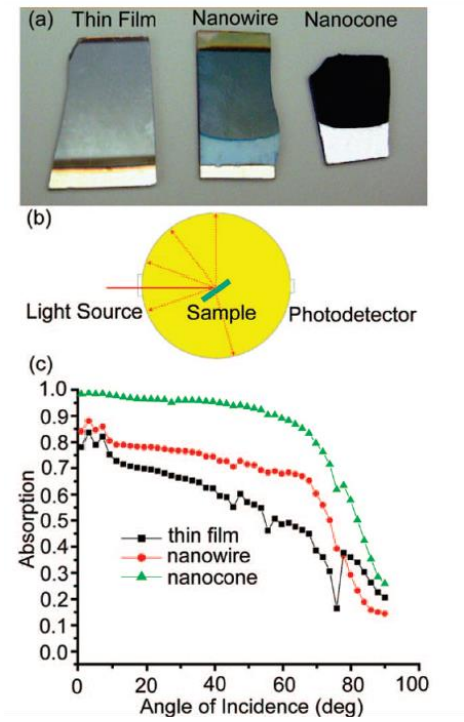

Figure 1.3 (a) Photographs of amorphous Si thin film (left), nanowire arrays (middle), and nanocone arrays (right). (b) Schematic illustration of hemispherical measurement using integrating sphere. (c) Measured results of absorption on samples with amorphous thin film, nanowire arrays, and nanocone arrays as top layer over different angles of incidence (at wavelength of 488 nm). Reprinted with permission from [8].Copyright 2009 American Chemical Society.

Nanocones array can significantly increase the absorption of the incident light. J. Zhu et al. have compared the absorption ability among silicon thin film, nanowires array, and nanocones array. At incident angles up to 60°, the absorption for Si-NCs was more than 90% which is much better than thin films (45%) and nanowire arrays (70%), as shown in figure 1.3 [8]. Nanocones structure has also been designed on the double-side of an ultrathin (1736 nm) Si film for the light trapping [9]. After optimizing the structure, the photocurrent of the solar cell reached 34.6 mA/cm^2, which is close to the Yablonovitch limit [10, 11]. Jeong coated conductive polymer on the Si-NCs as a hybrid Si / organic solar cell. This

nanocones structure enhanced the light absorption leading to a power conversion efficiency above 11% [12]. One year later in 2013, they have increased the efficiency to 13.7% by designing the Si-NCs on the front side of the device, but the emitter layer at the back, as shown in figure 1.4, to prevent the Auger and surface recombinations of charge carriers [13].

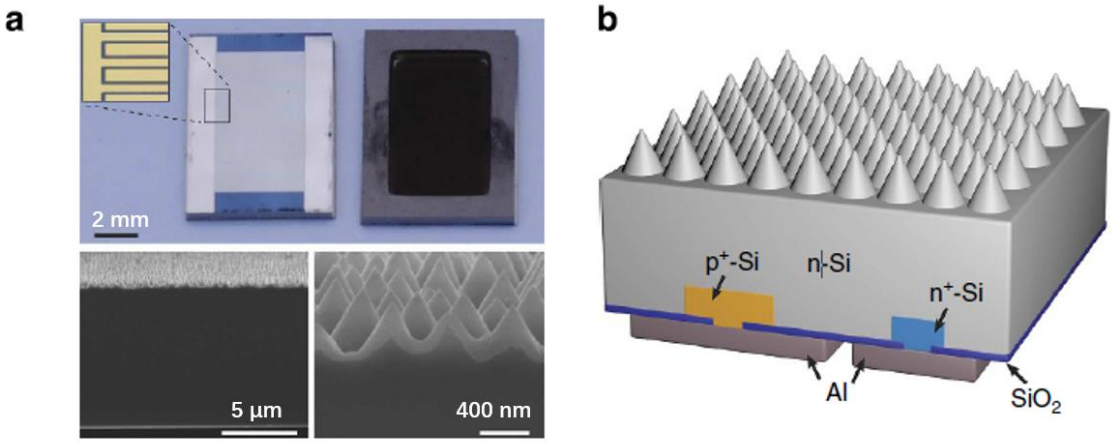

Figure 1.4 (a) Optical image of the back (top, left) and front (top, right) side of the 10-µm-thick Si solar cell. Inset shows the optical microscope image of the interdigitated metal electrodes. Scanning electron microscope (SEM) images of cross-sectional view of the device (bottom, left) and cross-sectional view of the nanocones (bottom, right). The thin layer at the top of the nanocones is an 80-nm-thick SiO_2 layer. Scale bars are 2 mm (top), 5 µm (bottom, left) and 400 nm (bottom, right). (b) Schematic illustration of the device. Reprint by permission from Springer Nature Communications [13], Copyright 2013.

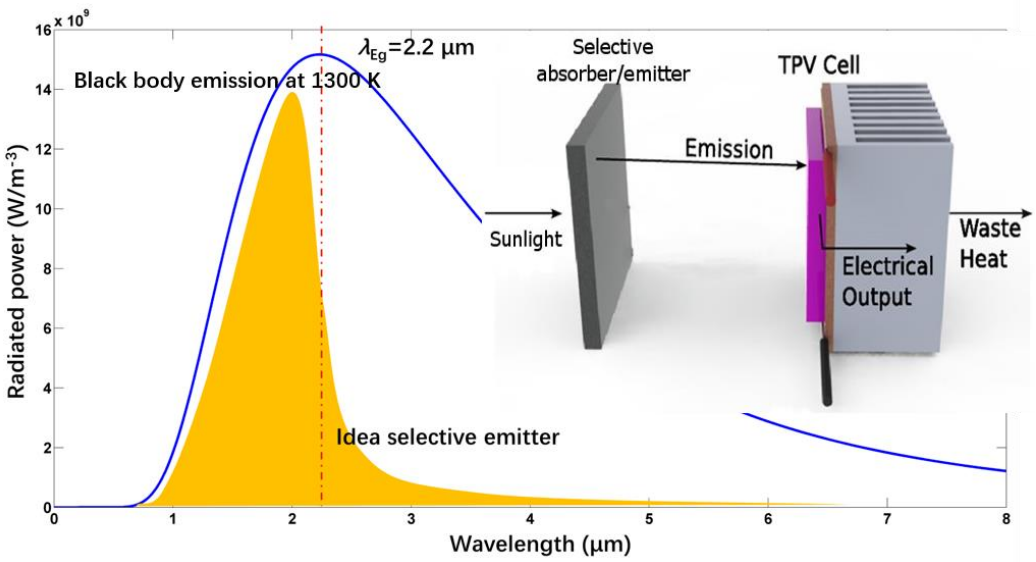

Figure 1.5 Emission from blackbody at 1300 K (blue line) and a selective emitter (yellow). Schematic of a thermophotovoltaic cell is shown in the inset [14].

Besides the solar cell, Si nanocones can be applied on many other fields. Similar to the solar cell, a thermophotovoltaic cell can transfer the heat energy to the electron energy via the thermal radiation [15, 16]. Matters with temperature radiate light to the outside due to the Plank law. As shown in the inset of Figure 1.5, the light emitted from a thermal emitter can be converted to electricity through a photovoltaic cell with a band gap energy defined by the corresponding wavelength λ_{Eg}. Figure 1.5 shows a spectrum curve of the blackbody radiation at 1300 K (blue line). Suppose that λ_{Eg} for a specific photovoltaic cell is 2.2 μm. Then, only the emission light of which wavelength shorter than 2.2 μm can contribute to the energy conversion. Thus, if the thermal radiation spectrum of a selective emitter almost concentrates in the yellow region shown in Figure 1.5, the conversion coefficient can be increased. Si-NCs was designed as the thermal emitter for the thermophotovoltaic system in [17]. The system efficiency is 11.2% at an emitter temperature of 1338 K.

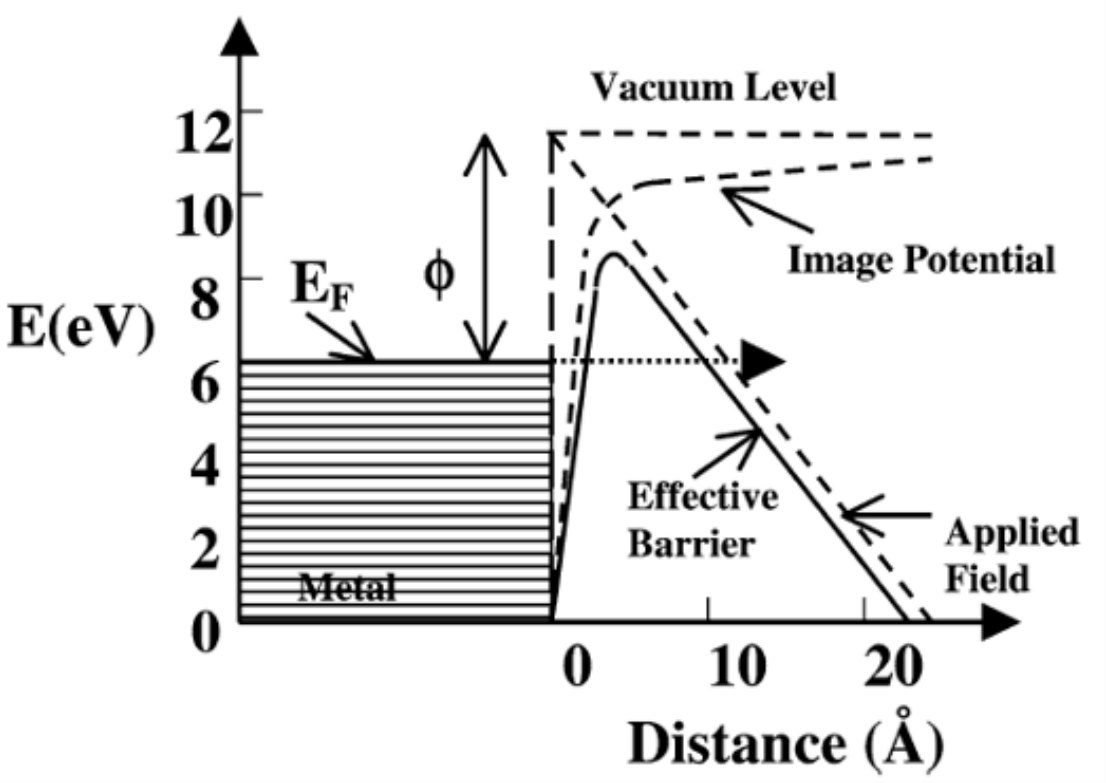

Figure 1.6 Potential-energy diagram illustrating the effect of an external electric field on the energy barrier for electrons at a metal surface. Reproduced from [19]. Copyright © 2003 Elsevier Masson SAS. All rights reserved.

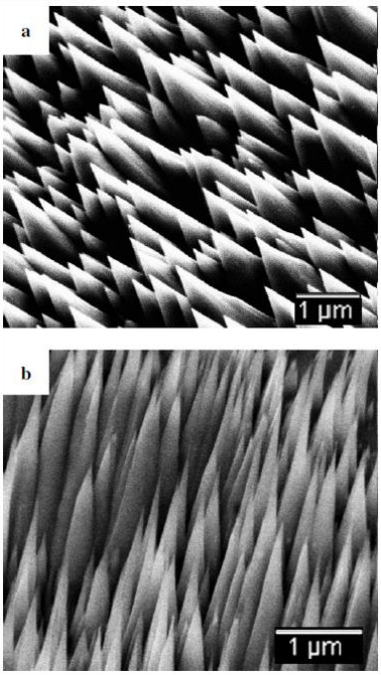

Figure 1.7 SEM images of the Si cone arrays (a) on silicon and (b) on porous Si [19]. © IOP Publishing. Reproduced with permission. All rights reserved. The porous structure can be seen in a higher resolution image.

Another application of the Si-NCs is field emitter. Electrons can be extracted from the material under a strong electric field via the quantum tunneling effect as shown in Figure 1.6 [18, 19]. Electrons close to the Fermi level will escape to vacuum with a potential smaller than the barrier energy. On the nanocone structure, the high curvature tip will strongly increase the electric potential around. Q. Wang demonstrated that properties of field emission of Si-NCs on porous Si are much better than those of the Si-NCs on Si due to their higher aspect ratio as shown in Figure 1.7 [20]. Moreover, coating with carbon thin layer enhanced the field emission ability of Si-NCs. A field emitter with Si-NCs structure performed high current density of 100 A cm^{-1} and long-life time over than 100 h, demonstrated by S. A. Guerrera et al. [21].

1.3 Fabrication of Si-NCs

1.3.1 Chemical process

The mainstream techniques of making Si-NCs are based on the etching process in dry or wet environment due to the chemical properties of Si. For dry etching, one of the typical methods is reactive ion etching (RIE) [22–24]. As shown in Figure 1.8, gas with fluorine, such as SF_6, is ionized in a vacuum chamber with a radio frequency (RF) power. Fluorine radicals will erode both the Si substrate and the oxide layer above and generate volatile SiF_4 with the following reaction:

$$Si+4F^{\bullet} \rightleftharpoons SiF_4 . \quad (1.1)$$

With the support of oxygen, etching products SiF_y will react with oxygen radicals forming a passivated layer on the sample surface

$$SiF_y+xO^{\bullet} \rightleftharpoons SiO_xF_y . \quad (1.2)$$

However, this silicon oxyfluoride layer is unstable and dissociates under the ion bombardment of plasma. Thus, anisotropic etching can be accomplished with substate bias which leads to the incident ions vertical to the substrate. The formation of the passivation layer on the vertical side wall keeps the Si substrate from further erosion by fluorine radicals, while on the horizontal surface the oxyfluoride layer is removed by the impinging of ions. Jansen used $SF_6/O_2/CHF_3$ mixture gases for the RIE of silicon and polymers with aluminum mask on the surface [25]. The tilted angle of the sidewall of the trench can be easily changed by adjusting the RF power and gas mixture. Si-NCs with the height of 300-500 nm and distance between the structures of 300–500 nm have been made by mask-less RIE method [26]. O_2 and SF_6 gas with a flow ratio of O_2:SF_6= 1:1 was employed and ionized by a RF platen with power of 100 W. Savin fabricated Si-NCs with a typical height of 800 nm and width of 200 nm by RIE for making a solar cell [27]. They demonstrated that the efficiency of the solar cell can reach 22% after a Al_2O_3 layer of 20 nm was coated on the top of the cone.

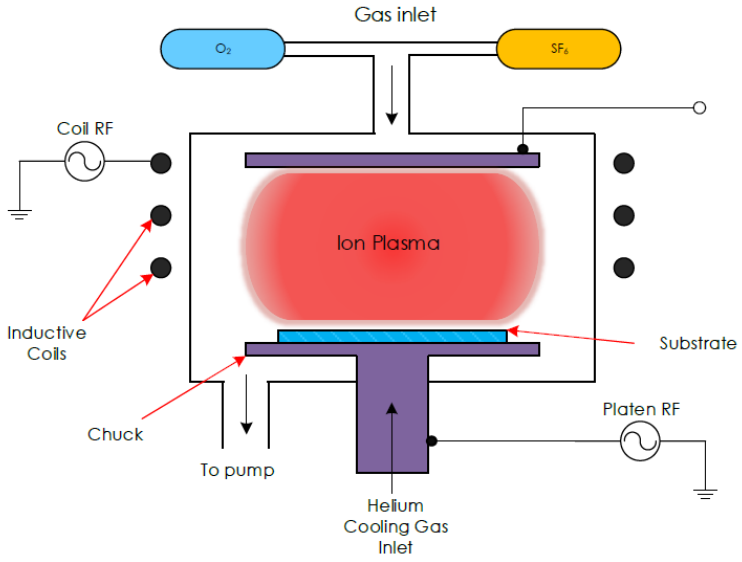

Figure 1.8 Schematic of inductive coupled plasma system used for RIE [28].

Surface texturing of Si in a wet process is called wet chemical etching [29–31]. The solution consists of HF and some oxidizing agents such as HNO_3. Reaction processes of the Si dissolution are described by following equations:

$$3Si+4HNO_3 \rightleftharpoons SiO_2+4NO+2H_2O \quad (1.3)$$

$$SiO_2+6HF \rightleftharpoons H_2SiF_6+2H_2O \quad (1.4)$$

$$3Si+4HNO_3+18HF \rightleftharpoons 3H_2SiF_6+4NO+8H_2O \quad (1.5)$$

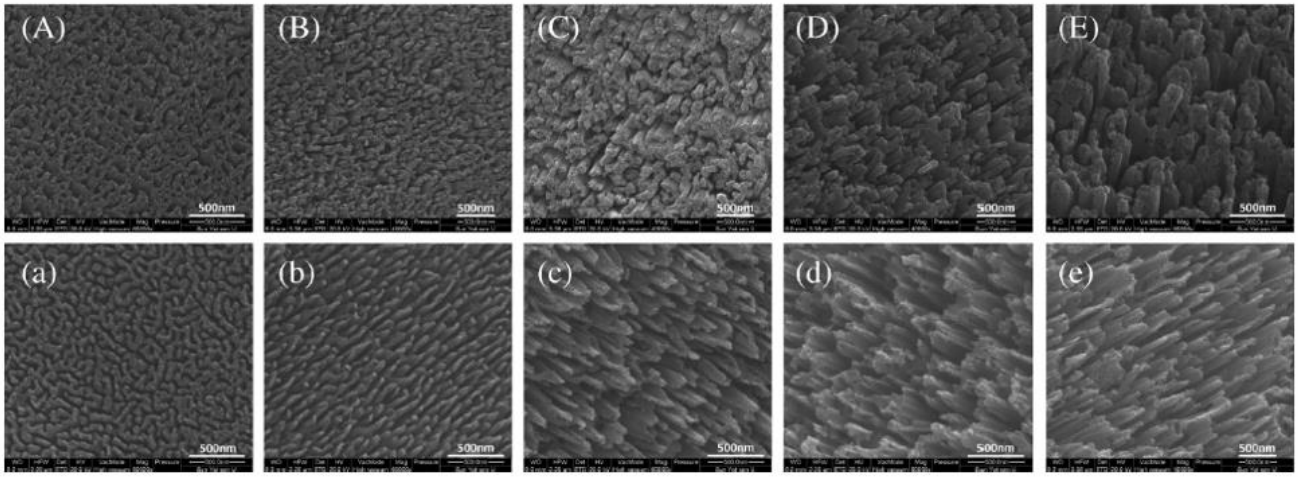

Figure 1.9 SEM images of the silicon wafers without (etching time being (A) 10 s, (B) 30 s, (C) 50s, (D) 70 s, and (E) 90 s) and with (etching time being (a) 10 s, (b) 30 s, (c) 50s, (d) 70 s, and (e) 90 s) HF treatment [30].

In order to form a nanocones structure, Koynov deposited a small amount of metal (Au) with a nominal thickness of 1-2 nm on the Si before the etching [32]. Nanometer size clusters of Au can be formed discontinuously on the Si surface and partially protect the surface from etching. Chen prepared a mixed solution of 15 vol. % HF and 5 vol. % H_2O_2 for the texturing of silicon surface. As shown in Figure 1.9, the length of nanocones and the space between them increase with the etching time [30].

1.3.2 Irradiation of noble gas plasma

Different from the chemical etching, surface texturing by helium (He), argon (Ar), or neon (Ne), plasma is primarily driven by physical processes. Cone structure has been reported over a wide range of materials and bombardment conditions. For example, Wehner has observed cone formation on more than 10 materials including molybdenum (Mo), iron (Fe), copper (Cu), and gold (Au) with Ar or xenon (Xe) plasma irradiation [33]. Kajita have observed cone structure on the surface of titanium (Ti) and stainless steel at surface temperature of 550 K, as shown in Figure 1.10 [34]. The impinging ion was He with an energy of 75 eV. Figure 1.11 (b) shows the nanocones structure formed on chromium (Cr) with He plasma irradiation at a low ion energy of ~80 eV [35]. Sputtering yield represented by the light emission intensity of Cr decreased as the time passes, as shown in Figure 1.11 (a). However, Ne plasma exposure did not lead to the formation of nanocones structure. Tanyeli exposed Cu into high flux ($5–7\times10^{23}$ $m^{-2}s^{-1}$) and low energy (<100 eV) He plasma [36]. Surface of Cu was roughened at the temperature of 500 ℃. Cone structures appeared when the surface temperature is higher than 650 ℃.

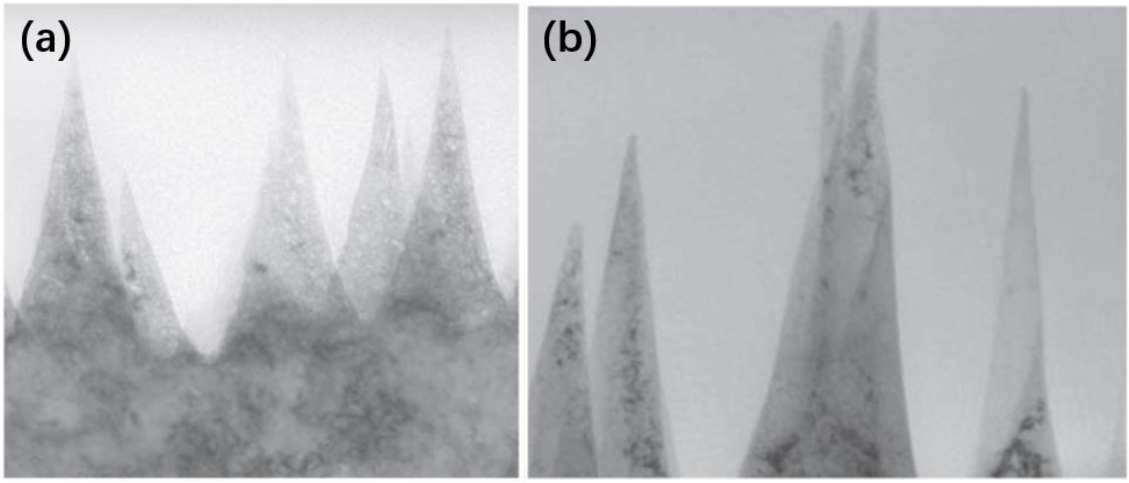

Figure 1.10 TEM micrographs of the (a) Ti and (b) stainless-steel samples, respectively, exposed to the He plasma. Reprinted from [34], with the permission of AIP Publishing.

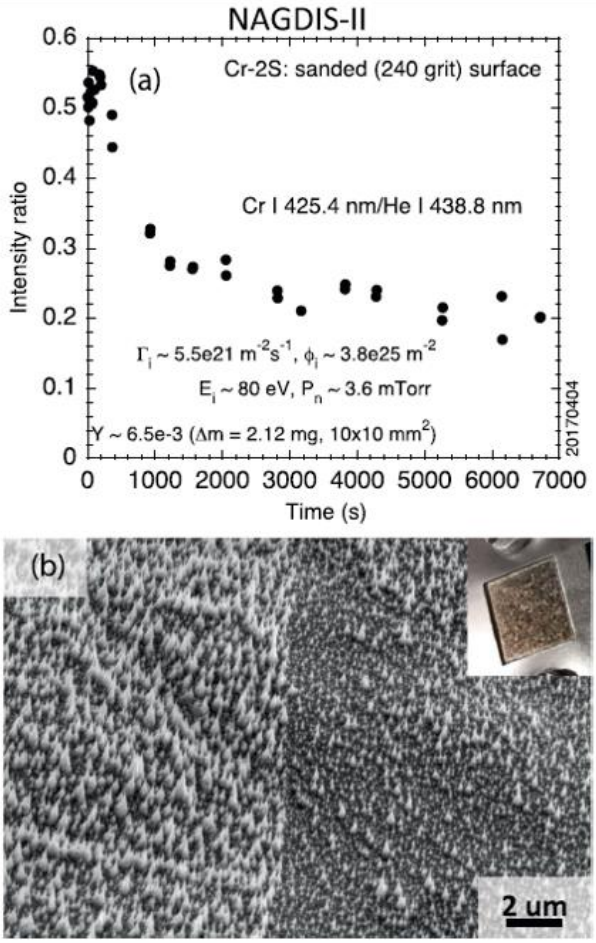

Figure 1.11 Typical Cr sputtering experimental result in NAGDIS-II. (a) Time evolution of the intensity ratio, Cr I 425.4 nm/He I 438.8, measured in front of a Cr sample during He plasma exposure. (b) SEM image of the Cr sample after the He plasma exposure. A photograph of the entire Cr sample is shown in the inset [35].

Si-NCs structure is also of great interest to be fabricated by plasma irradiation especially with low ion energy. Under the bombardment of He ion over an energy of 55 eV, nanocones structure was formed on the Si surface conducted by Takamura [37]. The density and diameter of the nanocones were quite different when changing the surface temperature and the ion fluence. Because the bombardment energy was low, the main body of the cone structure remained good crystalline structure which is the same as the substrate. By comparing the covered region and the exposed region of the Si surface, physical sputtering was concluded as the main process of the Si-NCs formation. Thompson observed nanostructure on the Si surface at even lower He ion energy (24 eV) which is closed to the threshold of sputtering yield [38]. However, significant modification can be observed only when the surface temperature is over 600 ℃. Moreover, the morphology was nonuniform which is likely due to the present of sample mask, as shown in Figure 1.12. Wu et al. conducted Si sputtering experiment in CH_4, N_2, and H_2 mixed plasma. Morphology of formed Si-NCs was significantly influenced by the ratio of CH_4 / (H_2 + N_2) [39]. The increase of plasma temperature and ion fluence can enhance the growth of Si-NCs. In Ar plasma with high ion energy (1.5 keV), Si-NCs structure was formed resulting in the suppression of optical reflectance less than 11% over the wavelength of 350–2000 nm [40].

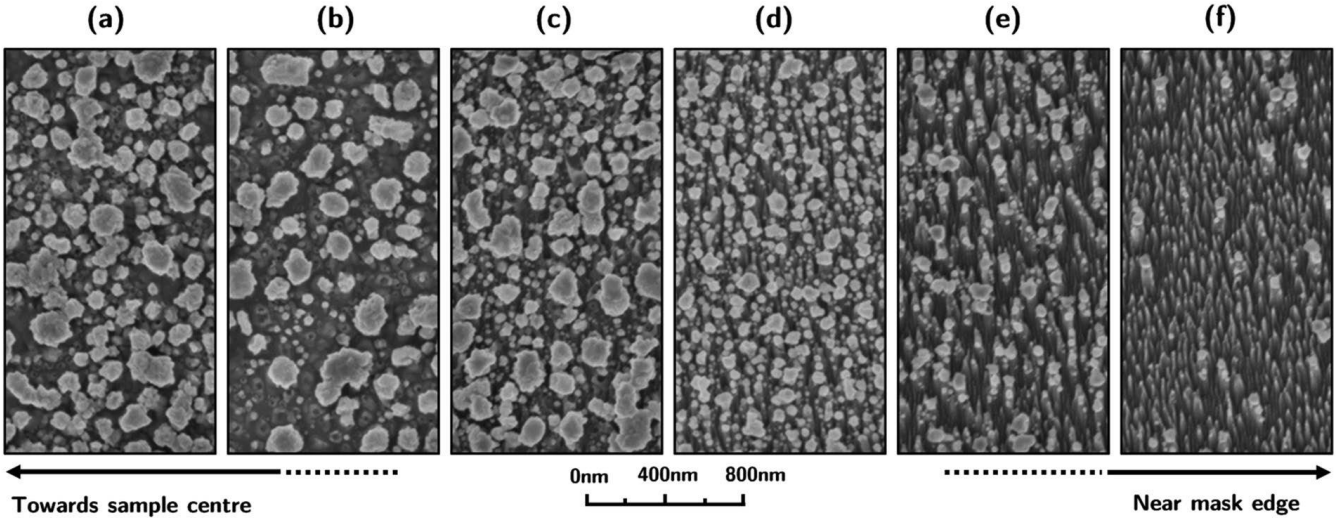

Figure 1.12 Silicon surface exposed to 24 eV helium plasma at 600 ± 6 ℃ in the region near the sample mask. Region close to the sample center (a), in intermediate position (b–e), and close to the mask (f) [38].

The formation the Si-NCs with plasma irradiation is broadly explained by the impurity during the ion bombardment. Tanemura have reported that nanocone structure cannot be identified without Mo impurity introduced [41]. Figure 1.13 shows the surface morphology of Si after 1.5 keV Ar ion irradiation for 45 min with and without metal incorporation. Si-NCs were observed only when samples were fixed by a stainless-steel cap from which Fe and Cr originate [40]. In a similar plasma condition, cone structure was formed on the silicon surface covered by a stainless-steel mask [42]. However, the mechanism of impurity-induced Si-NCs is still in discussion. In [42], Fe and Cr or Ni impurities are seemed as melted catalytic-sphere to lead the nanocone growth. This mechanism is called vapor-liquid-solid (VSL) proposed by R. S. Wagner and Ellis, as shown in figure 1.14 [43]. Zhou believed that the initial protrusions on the surface were formed by the protection of impurity atoms cluster due to the surface diffusion [40]. Tanemura depicted the cone formation process in 4 steps: (1) the deposition of impurity

atoms on the substrate surface, (2) the nucleation of impurity cluster or island due to the surface diffusion, (3) formation of protrusions with the proception of impurity clusters during the sputtering, (4) evolution of conical structures from the protrusions due to the angular dependence of the sputtering yield [41]. At a lower Ar ion energy (300 eV), impurity-induced tensile stress was suggested that plays a dominant role in driving the nanocone formation, because the stress changed from compressive to tensile after Mo was introduced [44, 45]. However, in Novakowski's study of 100 eV He ion irradiation, he preferred the growth of Si-NCs is because of the formation of SiC during exposure rather than the small amount (relative concentration is ~0.18%) of examined Ta.

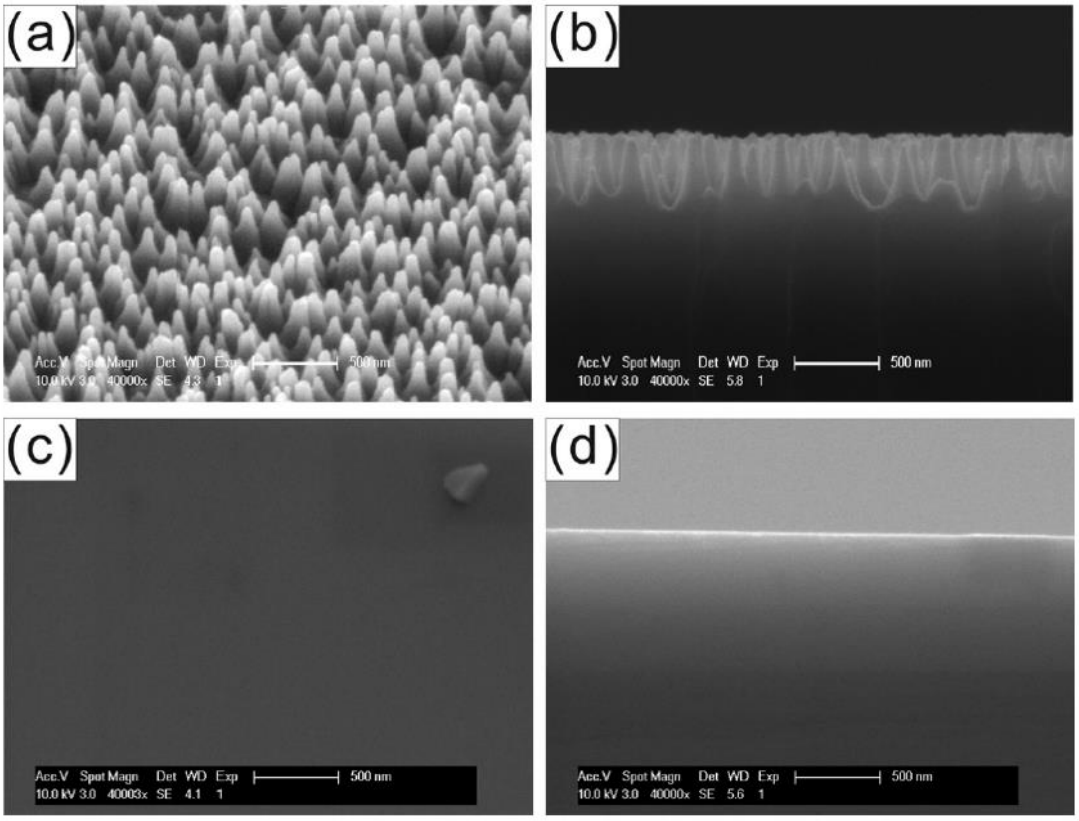

Figure 1.13 SEM images of the Si samples irradiated by 1.5 keV Ar ions at a current density of 1000 μA cm^{-2} for 45 min with [in (a), (b)] and without [in (c), (d)] metal incorporation. Bird's-eye view [in (a), (c)]. Cross-section view [in (b), (d)]. Reprinted from [40], with the permission of AIP Publishing.

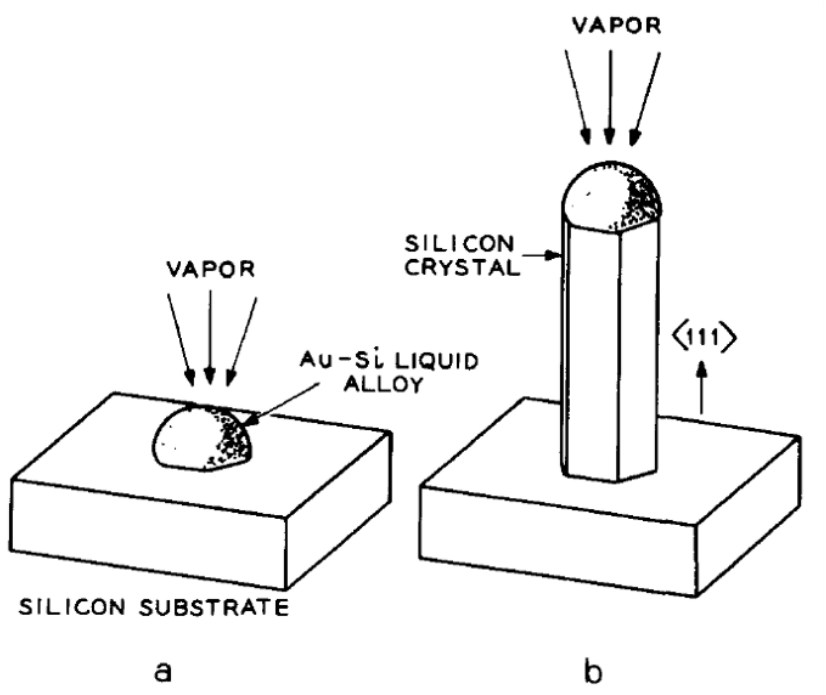

Figure 1.14 Schematic illustration: Growth of a silicon crystal by VLS. (a) Initial condition with liquid droplet on substrate. (b) Growing crystal with liquid droplet at the tip. Reprint from [43], with the permission of AIP Publishing.

1.3.3 Remaining issues

Compared with the conventional method (RIE, wet chemical etching) of Si-NCs fabrication, plasma irradiation has several advantages such as, toxicity-free environment, economical, mask-less, one step simple process, and rare surface damage. However, this technology is not mature enough. Some of the issues yet to be solved are listed below:

1. The mechanism of Si-NCs formation by low energy He plasma irradiation has not been fully understood. Although sputtering is the major process during the ion bombardment, to explain the formation of conical structure, more mechanisms should be taken into account.
2. It is difficult to form a uniform morphology in a large area because of the design of the sample stage/holder.
3. The relation between experiment parameters and features of Si-NCs have not been found. Thus, it is difficult to predict and customize the irradiated structure to meet the industrial requirement.
4. The performance of plasma-induced Si-NCs structure in applications, such as solar cell system or field emitter, have not been reported.

1.4 Purpose of the thesis

The purpose of this research is to discuss part of the issues mentioned above by investigating the Si-NCs formation under He plasma irradiation. It is beneficial to both the fabrication of Si-NCs and the understanding of plasma material interaction. The main research is outlined as follow and structured in figure 1.15:

1. (Chapter 3) Form the Si-NCs by low energy He plasma irradiation with different sample temperature, He ion fluence, and species of impurity seed, so as to find out the main factors which influence the Si surface morphology. Besides, the material of sample cover was changed to introduce different species of impurity seed, because impurity effect has been reported in many studies. After irradiation, real sputtering yields for different morphology of Si-NCs have been calculated via the erosion depth and compared with value on a flat surface. The mechanism of low energy plasma-induced Si-NCs formation was elementarily discussed.

2. (Chapter 4) Using Mont-Carlo method to simulate the formation of Si-NCs. Clusters of Mo were set at on the surface to represent the deposited Mo impurities. Growth of nanocone under the ion bombardment in both vertical and tilted direction was compared with the phenomena observed in experiments to verify the hypothetical mechanism. Line-of-sight redeposition effect of Si was involved in the simulation.

3. (Chapter 5) Design of experiment was improved in a more controllable manner by installing a Mo sputtering wire in front of the Si substrate. Parameters which significantly change the Si surface morphology can be quantified. It revealed the relation between experimental parameters and features of Si-NCs. By comparing the energy dispersive X-ray spectrometer (EDX) mapping result of nanocones with different features, a model that illustrate the process of Si-NCs formation was build up. The relation between optical reflection of the irradiated surface and features of Si-NCs was also discussed.

The mechanism of Si-NCs formation by low energy He plasma irradiation can be built by synthesizing each small piece of the mechanism summarized in the individual study. By the understanding of the mechanism, this study concludes that the control of impurity (Mo) ratio to He flux can be a potential method to fabricate Si-NCs with tunable structure.

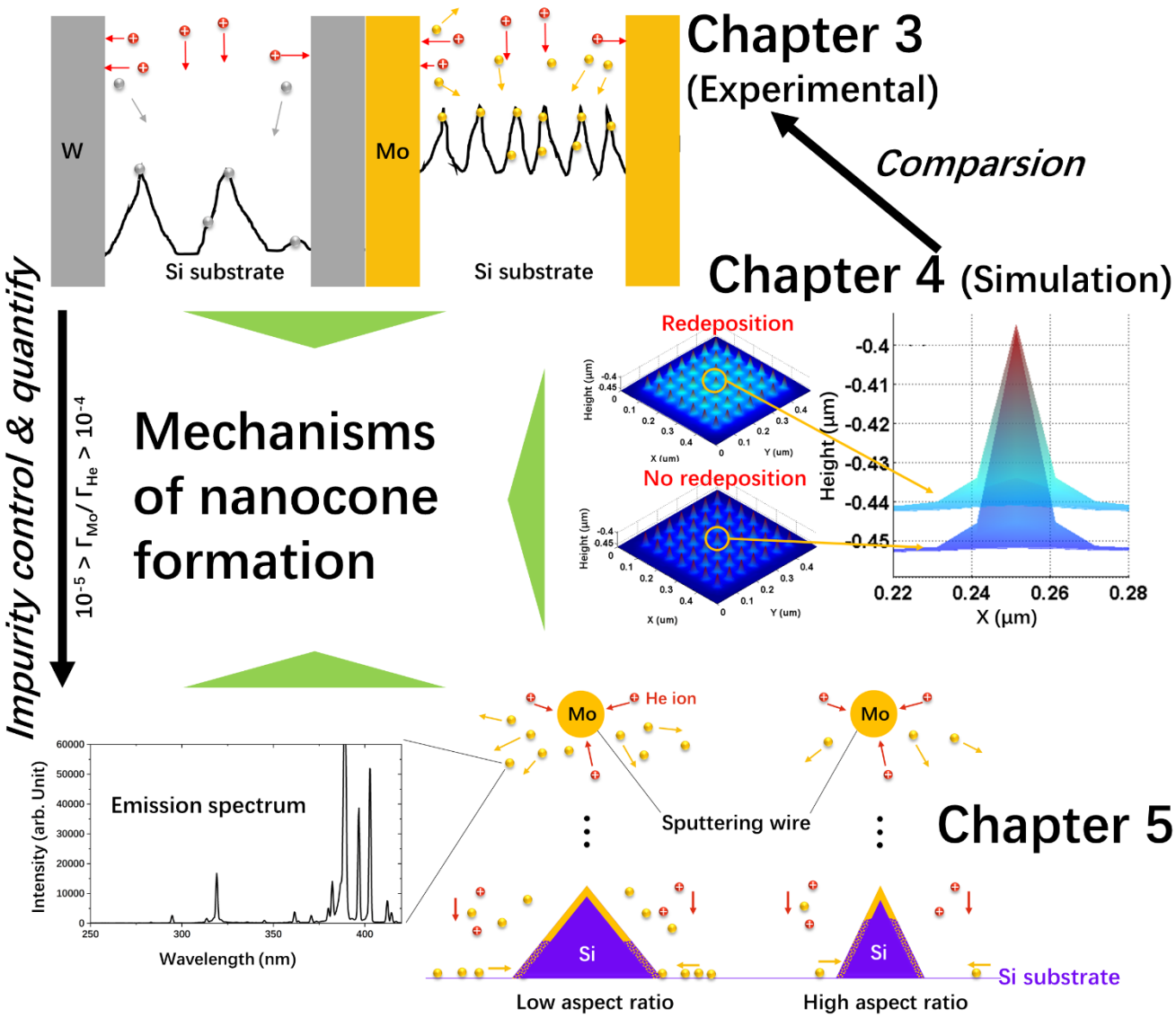

Figure 1.15 Outline of the purpose of this research and the relation between each work.

References

[1] O. Gaffney, & W. Steffen, The Anthropocene Equation, The Anthropocene Review **4** (2017) 53–61.

[2] H. Ritchie, Energy Mix, Published online at OurWorldInData.org. Retrieved from: https://ourworldindata.org/energy-mix.

[3] S. Chhajed, M. F. Schubert, J. K. Kim, & E. F. Schubert, Nanostructured Multilayer Graded-index Antireflection Coating for Si Solar Cells with Broadband and Omnidirectional Characteristics, Applied Physics Letters **93** (2008) 251108.

[4] S. J. Fonash, Solar Cell Device Physics, Academic Press: New York, London, 1981.

[5] A. Mavrokefalos, S. E. Han, S. Yerci, M. S. Branham, & G. Chen, Efficient Light Trapping in Inverted Nanopyramid Thin Crystalline Silicon Membranes for Solar Cell Applications, Nano Letters **12** (2012) 2792–2796.

[6] J. Zhu, C-M. Hsu, Z. Yu, S. Fan, & Y. Cui, Nanodome Solar Cells with Efficient Light Management and Self-cleaning, Nano Letters **10** (2010) 1979–1984.

[7] J. Wallentin, N. Anttu, D. Asoli, M. Huffman, I. Aberg, M. H. Magnusson, G. Siefer, P. Fuss-Kailuweit, F. Dimroth, B. Witzigmann, H. Q. Xu, L. Samuelson, K. Deppert, & M. T. Borgstrom, InP Nanowire Array Solar Cells Achieving 13.8% Efficiency by Exceeding the Ray Optics Limit, Science **17** (2013) 1230969.

[8] J. Zhu, Z. Yu, G. F. Burkhard, C-M. Hsu, S. T. Connor, Y. Xu, Q. Wang, M. Mcgehee, S. Fan, & Y. Cui, Optical Absorption Enhancement in Amorphous Silicon Nanowire and Nanocone Arrays, Nano Letters **9** (2009) 279–282.

[9] K. X. Wang, Z. Yu, V. Liu, Y. Cui, & S. Fan, Absorption Enhancement in Ultrathin Crystalline Silicon Solar Cells with Antireflection and Light-trapping Nanocone Gratings, Nano Letters **12** (2012) 1616–1619.

[10] E. Yablonovitch, Statistical Ray Optics, Journal of the Optical Society of America **72** (1982) 899−907.

[11] E. Yablonovitch, & G. D. Cody, Intensity Enhancement in Textured Optical Sheets for Solar Cells, IEEE Transactions on Electron Devices **29** (1982) 300−305.

[12] S. Jeong, E. C. Garnett, S. Wang, Z. Yu, S. Fan, M. L. Brongersma, M. D. Mcgehee, & Y. Cui, Hybrid Silicon Nanocone–polymer Solar Cells, Nano Letters **12** (2012) 2971–2976.

[13] S. Jeong, M. McGehee, & Y. Cui, All-back-contact Ultra-thin Silicon Nanocone Solar Cells with 13.7% Power Conversion efficiency, Nature Communications **4** (2013) 2950.

[14] Z. Zhou, E. Sakr, Y, Sun, & P. Bermel, Solar Thermophotovoltaics: Reshaping the Solar Spectrum, Nanophotonics **5** (2016) 1–21.

[15] B. Wedlock, Thermo-photo-voltaic Energy Conversion, Proceeding of the IEEE **51** (1963) 694−698.

[16] D. G. Baranov, Y. Xiao, I. A. Nechepurenko, A. Krasnok, A. Alù, & M. A. Kats, Nanophotonic Engineering of Far-field Thermal Emitters, Nature Materials **8** (2019) 920−930.

[17] M. Suemitsu, T. Asano, T. Inoue, & S. Noda, High-Efficiency Thermophotovoltaic System that Employs an Emitter Based on a Silicon Rod-Type Photonic Crystal, ACS Photonics **7** (2020) 80−87.

[18] R. Gomer, Field Emission and Field Ionization, Harvard University Press: Cambridge, MA, 1961.

[19] Y. Cheng, & O. Zhou, Electron Field Emission from Carbon Nanotubes, Comptes Rendus Physique **4** (2003) 1021–1033.

[20] Q. Wang, J. J. Li, Y. J. Ma, X. D. Bai, Z. L. Wang, P. Xu, C. Y. Shi, B. G. Quan, S. L. Yue, & C. Z. Gu, Field Emission Properties of Carbon Coated Si Nanocone Arrays on Porous Silicon, Nanotechnology **16** (2005) 2919.

[21] S. A. Guerrera, & A. I. Akinwande, Nanofabrication of Arrays of Silicon Field Emitters with Vertical Silicon Nanowire Current Limiters and Self-aligned Gates, Nanotechnology **27** (2016) 295302.

[22] C. Fischer, J. W. Menezes, S. A. Moshkalev, C. VeríSsimo, A. R. Vaz, & J. W. Swart, Fabrication of High-aspect Ratio Silicon Nanopillars and Nanocones Using Deep Reactive Ion Etching, Journal of Vacuum Science & Technology B: Microelectronics and Nanometer Structures **27** (2009) 2732.

[23] L. Schneider, N. Feidenhans'l, A. Telecka, & R. J. Taboryski, One-step Maskless Fabrication and Optical Characterization of Silicon Surfaces with Antireflective Properties and a White Color Appearance, Scientific Reports **6** (2016) 35183.

[24] G. Fischer, E. Drahi, M. Foldyna, T. A. Germer, & E. V. Johnson, Plasma Nanotexturing of Silicon Surfaces for Photovoltaics Applications: Influence of Initial Surface Finish on the Evolution of Topographical and Optical Properties, Optics Express **25** (2017) A1057–A1071.

[25] H. Jansen, M. de Boer, R. Legtenberg, & M. Elwenspoek, The Black Silicon Method: A Universal Method for Determining the Parameter Setting of a Fluorine-based Reactive Ion Etcher in Deep Silicon Trench Etching with Profile Control, Journal of Micromechanics and Microengineering **5** (1995) 115–120.

[26] R. S. Davidson, H. Li, A. To, X. Wang, A. Han, J. An, J. Colwell, C. Chan, A. Wenham, M. S. Schmidt, A. Boisen, O. Hansen, S. Wenham, & A. Barnett, Black Silicon Laser-doped Selective Emitter Solar Cell with 18.1% Efficiency, Solar Energy Materials and Solar Cells **144** (2016) 740–747.

[27] H. Savin, P. Repo, G. von Gastrow, P. Ortega, E. Calle, M. Garin, & R. Alcubilla, Black Silicon Solar Cells with Interdigitated Back-contacts Achieve 22.1% Efficiency, Nature Nanotech **10** (2015) 624–628.

[28] M. Plakhotnyuk, R. S. Davidson, M. S. Schmidt, R. Malureanu, E. Stamate, & O. Hansen, Lifetime of Nano-structured Black Silicon for Photovoltaic Applications, In the 32nd European Photovoltaic Solar Energy Conference and Exhibition **2AV.2.34** (2016) 764–767.

[29] H. Lin, H. Y. Cheung, F. Xiu, F. Wang, S. P. Yip, N. Han, T. Hung, J. Zhou, J. C. Ho, & C. Y. Wong, Developing Controllable Anisotropic Wet Etching to Achieve Silicon Nanorods, Nanopencils and Nanocones for Efficient Photon Trapping, Journal of Materials Chemistry A **1** (2013) 9942–9946.

[30] S. R. Chen, Z. C. Liang, & D. L. Wang, Nano Silver-catalyzed Chemical Etching of Polycrystalline Silicon Wafer for Solar Cell Application, AIP Advances **6** (2016) 035320.

[31] X. Li, & P. W. Bhon, Metal-assisted Chemical Etching in HF/H_2O_2 Produces Porous Silicon, Applied Physics Letters **77** (2000) 2572–2574.

[32] S. Koynov, M. S. Brandt, & M. Stutzmann, Black Nonreflecting Silicon Surfaces for Solar Cells, Applied Physics Letters **88** (2006) 203107.

[33] G. K. Wehner, Cone Formation as a Result of Whisker Growth on Ion Bombarded Metal Surfaces, Journal of Vacuum Science & Technology A **3** (1985) 1821–1835.

[34] S. Kajita, T. Yoshida, D. Kitaoka, R. Etoh, M. Yajima, N. Ohno, H. Yoshida, N. Yoshida, & Y. Terao, Helium Plasma Implantation on Metals: Nanostructure Formation and Visible-light Photocatalytic Response, Journal of Applied Physics **113** (2013) 134301.

[35] D. Nishijima, A. Kreter, M. J. Baldwin, D. Borodin, A. Eksaeva, D. Hwangbo, S. Kajita, M. Miyamoto, N. Ohno, M. Patino, A. Pospieszczyk, M. Rasinski, T. Schlummer, A. Terra, & R. P.

Doerner, Influence of Heavier Impurity Deposition on Surface Morphology Development and Sputtering Behavior Explored in Multiple Linear Plasma Devices, Nuclear Materials and Energy **18** (2019) 67–71.

[36] İ. Tanyeli, L. Marot, D. Mathys, C. M. M. Van De Sanden, & G. De Temmerman, Surface Modifications Induced by High Fluxes of Low Energy Helium Ions, Scientific Reports **5** (2015) 9779.

[37] S. Takamura, T. Aota, H. Iwata, S. Maenaka, K. Fujita, Y. Kikuchi, & Y. Uesugi, Black Silicon with Nanostructured Surface Formed by Low Energy Helium Plasma Irradiation, Applied Surface Science **487** (2019) 755–765.

[38] M. Thompson, L. Magyar, & C. Corr, Nanoscale Modification of Silicon and Germanium Surfaces Exposed to Low-energy Helium Plasma, Scientific Reports **9** (2019) 10099.

[39] Z. C. Wu, L. L. Guan, H. Li, J. D. Wu, J. Sun, & N. Xu, Growth of Single-Crystalline Silicon Nanocone Arrays by Plasma Sputtering Reaction Deposition, Chinese Physics Letters **34** (2017) 025202.

[40] J. Zhou, M. Hildebrandt, & M. Liu, Self-organized Antireflecting Nano-cone Arrays on Si (100) Induced by Ion Bombardment, Journal of Applied Physics **109** (2011) 053513.

[41] M. Tanemura, H. Yamauchi, Y. Yamane, T. Okita, & S. Tanemura, Controlled Fabrication of Mo-seeded Si Microcones by Ar^{+}-ion Bombardment, Nuclear Instruments and Methods in Physics Research Section B: Beam Interactions with Materials and Atoms **215** (2004) 137–142.

[42] Y. Qiu, H. C. Hao, J. Zhou, & M. Liu, A Close to Unity and All-solar-spectrum Absorption by Ion-sputtering Induced Si Nanocone Arrays, Optics Express **20** (2012) 22087–22094.

[43] R. S. Wagner, & W. C. Ellis, Vapor-liquid-solid Mechanism of Single Crystal Growth, Applied Physics Letters **4** (1964) 89–90.

[44] G. Ozaydin, K. F. Ludwig, H. Zhou, & R. L. Headrick, Effects of Mo Seeding on the Formation of Si Nanodots during Low-energy Ion Bombardment, Journal of Vacuum Science & Technology B: Microelectronics and Nanometer Structures Processing, Measurement, and Phenomena **26** (2008) 551–558.

[45] L. B. Begrambekov, A. M. Zakharov, & V. G. Telkovsky, Peculiarities and Mechanism of the Cone Growth under Ion Bombardment, Nuclear Instruments and Methods in Physics Research Section B: Beam Interactions with Materials and Atoms **115** (1996) 456–460.

Chapter 2. Experimental devices and basic theories

2.1 Linear plasma device Co-NAGDIS

Experiments were conducted by a linear plasma device Compact-Nagoya University divertor plasma simulator (Co-NAGDIS) [1–3]. A schematic of Co-NAGDIS is shown in figure 2.1. Length of the discharge region is ~74.5 cm. Sample can be installed from the side of the device by a sample manipulator. The background pressure of the chamber is ~1×10^{-4} Pa. He plasma is generated by a direct current (DC) arc discharge with a discharge power of 1750 W. The cathode is a meander LaB_6 and the anode is made of copper. During the plasma irradiation, the neutral gas pressure will raise up to 2.0–3.0 Pa. Diameter of the plasma column is ~20 mm which is much smaller than the diameter of the vessel (stainless steel). The magnetic field at the center of plasma column is ~12.5 mT. The typical electron density and temperature were ~1×10^{18} m^{-3} and 6 eV, respectively. As shown in figure 2.2, during the plasma irradiation, the electron temperature, electron density, and ion flux were measured by a cylindrical Langmuir probe, which is set 20 mm in front of the sample. The sample temperature can be adjusted by an air-cooling system and monitored by a thermometer. Sample is biased with a DC power supply.

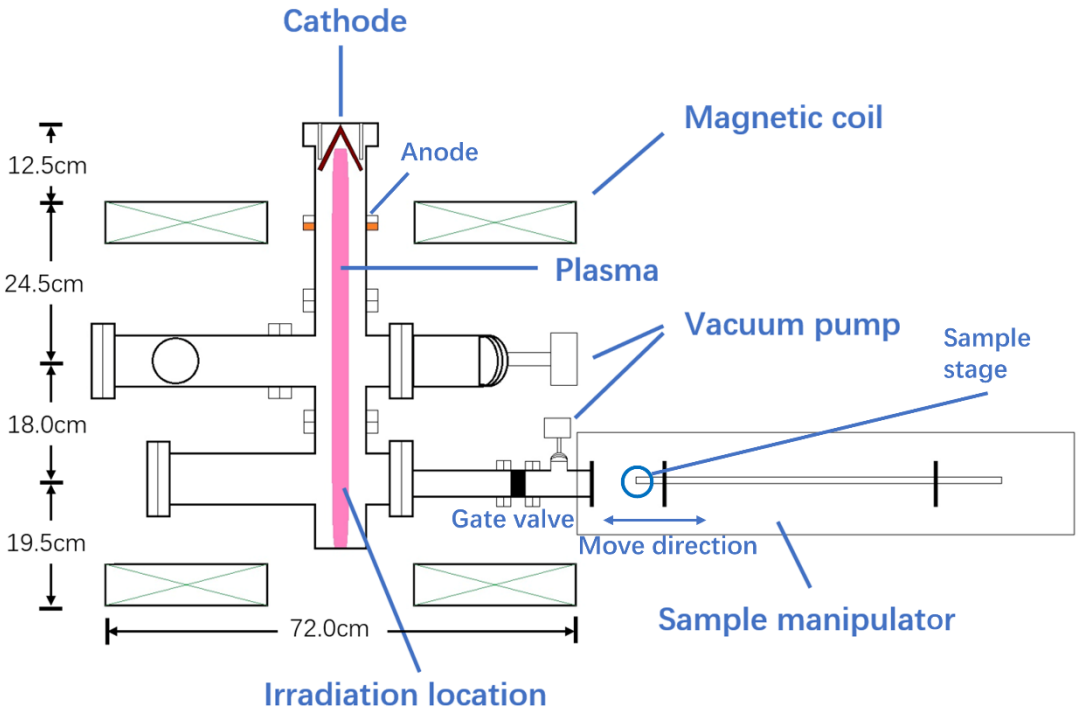

Figure 2.1 A schematic of the linear plasma device Co-NAGDIS from bird-eye view.

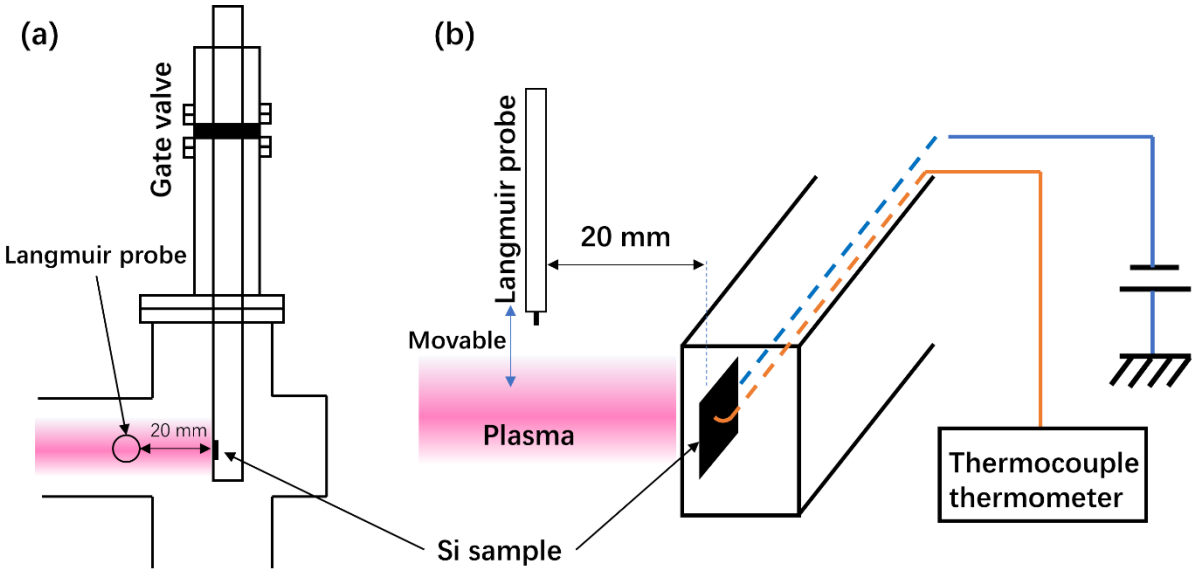

Figure 2.2 A schematic of irradiation position of Co-NAGDIS from (a) the top view and (b) the side view.

2.2 Single Langmuir probe

Figure 2.3 (a) is the design of the single Langmuir probe used in Co-NAGDIS. V_1 shows the bias on the probe, V_2 shows the bias on a resistance for the measurement of probe current I_p. When the tip of the probe contacts with plasma, the bipolar power supply provides variational bias V_p to the probe. In our study, the range of bias change is from -100 V to 20 V. Then we can obtain the $I_p - V_p$ curve which can be separated in three regions (A, B and C), as shown in figure 2.3 (b).

2.2.1 Electron density

In the region A, because V_p is much lower than the plasma space potential V_{sp}, all the electrons cannot reach the surface of the probe due to the electric field in the sheath. On the contrary, all the ions which accessed in the sheath will be collected by the probe. Thus, the current shown in section A is called ion saturation current I_{si} which is given as

$$I_{si} = Sen_{is}C_s . \tag{2.1}$$

Here, n_{is} is the ion density at the sheath edge, which is equal to the electron density at the sheath edge n_{es}, S is the area of the probe, and C_s is the ion acoustic speed. n_{es} can be found from the Boltzmann relation

$$n_{es} = n_e \exp\left(\frac{-e\Phi_0}{kT_e}\right), \tag{2.2}$$

where $\Phi_0 = kT_e / 2e$ is the potential at the edge of sheath due to the Bohm sheath criterion, k is the Boltzmann constant, and T_e is the electron temperature, n_e is the electron density in the bulk plasma region. By substituting equation (2.2) to (2.1), we can rewrite the ion saturation current as

$$I_{si} = n_e \exp\left(\frac{-e\Phi_0}{kT_e}\right) eSC_s = n_e \exp(-1/2) eSC_s \approx 0.61 n_e eSC_s . \tag{2.3}$$

The condition in the region C is similar to A. V_p is much higher than V_{sp}, all electrons which accessed in the sheath can reach the probe surface. The electron saturation current can be expressed by

$$I_{se} = \frac{1}{4} e n_e S \left(\frac{8kT_e}{\pi m_e} \right)^{1/2}, \tag{2.4}$$

where m_e is the mass of electron. Thus, electron density can be deduced from both equations (2.3) and (2.4). In this research, n_e is calculated via the electron saturation current. According to the research in [4], the magnetic field of 12.5 mT is strong enough to form plane sheath for electrons on the probe. Hence, S is the projection area of the probe.

2.2.2 Electron temperature

In the transition region (region B), the probe current is dominated by the number of electrons which reach the surface of the probe. The electron current I_e will increase as the V_p closing to V_{sp}. Assuming the electron energy distribution is Maxwellian, the probe current can be expressed as

$$I_e = I_p - I_{si} = I_{se} \exp\left[\frac{e(V_p - V_{sp})}{kT_e} \right], \tag{2.5}$$

Taking the logarithm of equation (2.5), the electron temperature can be expressed as

$$T_e = \frac{e(V_p - V_{sp})}{k(\ln I_e - \ln I_{se})}. \tag{2.6}$$

Thus, the electron temperature can be obtained from the slope of the line of V_p – ln I_e in the transition region.

2.2.3 Ion flux

Because the testing point of the probe is close to the irradiation location of the sample, assuming that the ion flux, Γ, on the sample is same as the flux on the probe. Ion flux can be obtained via the ion saturation current as follow:

$$\Gamma = \frac{I_{si}}{eS}. \tag{2.7}$$

Note that a metal sample holder was biased together with the Si sample. Therefore, this study did not use the sample current to calculate the ion flux directly.

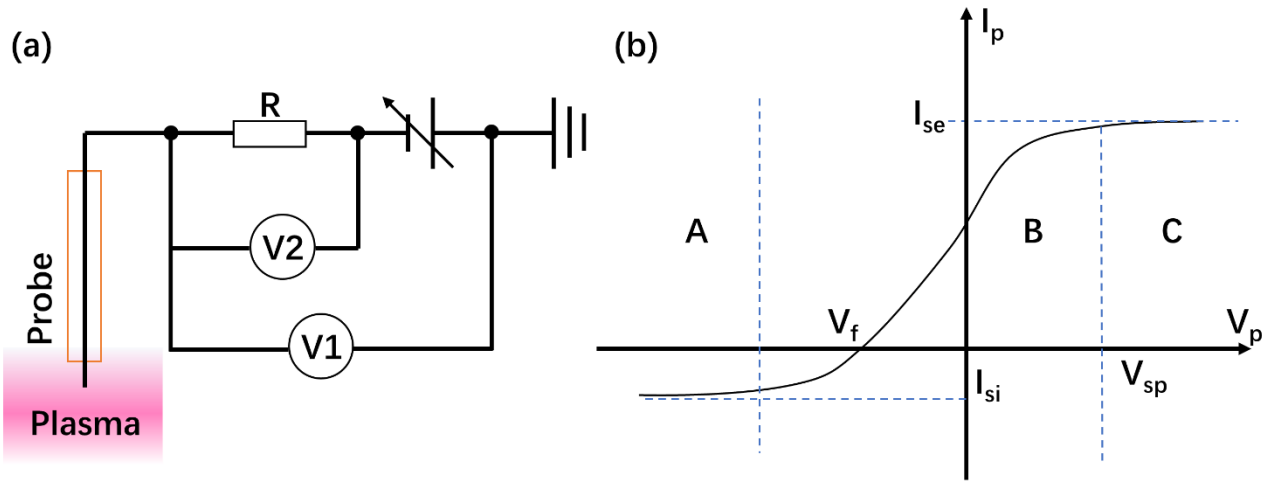

Figure 2.3 (a) Design of the single Langmuir probe. (b) A typical current-voltage curve output from the probe. The curve has been separated into three sections: ion saturation region (A), transition region (B), and electron saturation region (C).

2.3 Sputtering

When ion impacts on a solid surface, it will transfer the energy to collided atoms on the surface layer, leading to a serial cascade movement of atoms. If the atom is moving towards the outside of the surface with an energy that exceeds the surface binding energy, it will be ejected out of the surface. This phenomenon is called physical sputtering which was first reported by Grove who found that the composition of the metallic deposition on the inner wall of a gas discharge vessel was the same as the cathode [5]. In 1969, Sigmund built an atomic cascade-collision model and proposed the equation of sputtering yield based on numerous experiment studies [6]. The calculation of sputtering yield is based on the theory proposed by Eckstein in [7]. Sine angular distribution [8] and Thompson energy distribution [9] are served as the kinetic information of sputtered atoms.

2.3.1 Energy distribution of sputtered species

The energy distribution of sputtered atoms can be described in a first order approximation by the Thompson distribution:

$$\Phi(E)\,dE = \frac{E}{(E+E_b)^3}\,dE\,, \tag{2.8}$$

where $\Phi(E)$ is the flux of sputtered atom with energy E, and E_b is the surface binding energy [10]. Applying this distribution, the energy E can be determined by a random number r due to the formula

$$\frac{E}{E_s} = \frac{1}{(1+1/a)\sqrt{1/r}-1}, \tag{2.9}$$

where a is the maximum transferred energy divided by the surface binding energy

$$a = \frac{4m_1m_2}{(m_1+m_2)^2}\frac{E_0}{E_s}. \tag{2.10}$$

Here m_1 and m_2 are the mass of projectile and target particle, E_0 is the incident energy. One can see that the energy distribution of sputtered atoms is primarily determined by the surface binding energy. In chapter 5, the average energy of sputtered Mo atoms is treated as the same for different He ion energy on sputtering wire.

2.4 Simulation method

2.4.1 SURO code

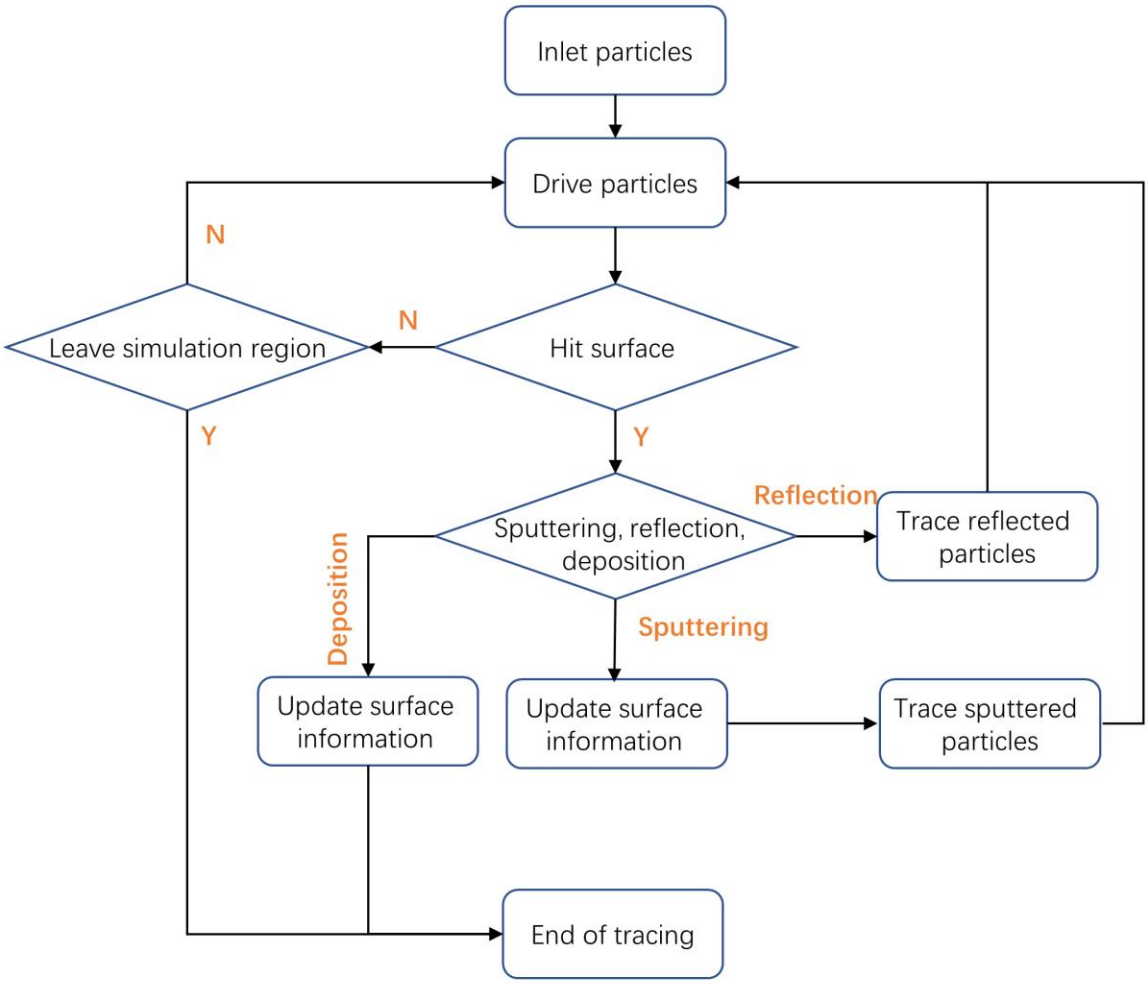

Figure 2.4 Schematic of SURO code.

The simulation code employed in Chapter 4 is called SURO abbreviated from “surface roughness” [11]. It was designed for the investigation of the interaction between plasma and materials including sputtering, deposition, and surface evolution in three dimensions. It has been used to simulate the surface evolution on limiter and divertor in fusion relevant environment. A schematic of SURO code is shown in figure 2.4.

(1) First, particles such as ions and atoms are injected to the top of the simulation region.
(2) Movement of particles are driven by a distribution of energy and angle due to the source of particles.

(3) If particles hit the surface which can be customized by user, they will either be reflected or deposit on the surface, which depends on the reflection coefficient [12, 13]. Calculation of the sputtering process has been introduced in section 2.3.
(4) Surface information such as component, height, and surface normal will be updated according to the event in (3).
(5) Sputtered or reflected particles are traced and treated from (2) again until they will deposit or leave the simulation region.

2.4.2 A-CAT code

The Monte Carlo program A-CAT [14] was developed to determine the total sputtering yields and angular distributions of sputtered atoms in physical processes. From computer results of the incident energy dependent sputtering for various ion-target combinations the mass ratio dependence and the bombarding angle dependence of sputtering threshold was obtained with the help of the Matsunami empirical formula for sputtering yields. The mass ratio dependence of sputtering thresholds is in good agreement with theoretical results. The threshold of light ion sputtering is a slightly increasing function of angle of incidence, while that of heavy ion sputtering has a minimum value near 60°.

The angular distributions of sputtered atoms are also calculated for heavy ions, medium ions, and light ions, and reasonable agreements between calculated angular distributions and experimental results are obtained.

2.4.3 Monte Carlo method

Monte Carlo method is an extensive algorithm, which relies on repeated random sampling to obtain numerical results. Its basic idea is to use randomness to solve the problem that may be deterministic in principle. It is often used to solve physical and mathematical problems, especially when there is no other way to solve them. Monte-Carlo method is mainly applied to three kinds of problems: optimization, numerical integration, and extraction of numerical value from probability distribution [15].

In principle, Monte Carlo method can be used to solve any problem with probability interpretation. According to the law of large numbers, the integral described by the expected value of random variables can be approximated by taking the empirical mean value of independent samples of variables (also known as the sample mean value). When the probability distribution of variables is parameterized, mathematicians often use Markov chain Monte Carlo (MCMC) sampler [16–18]. The main idea is to design a Markov chain model with fixed stationary probability distribution. In other words, in the limit, the samples generated by the Markov chain Monte Carlo method will be the samples from the expected (target) distribution [19, 20]. According to the ergodic theorem, the stationary distribution is approximated by the empirical measurement of the random state of Markov chain Monte Carlo samples.

In SURO, Monte Carlo method was used to simulate the behaviors of particles, such as ions impinging and sputtering of substrate atoms. For example, particles randomly sputtered from the substrate with different probability for different energy refer to the Thompson's theory. Sputtering information of a single particle was not calculated from physical processes, but the energy distribution of particles was reasonable if the number of particles is large enough. In chapter 4, ion flux was separated into ten thousand segments.

2.5 Optical emission spectrum analysis

2.5.1 Photon emissivity coefficient

Because the election density n_e and temperature T_e in this study is low, the amount of the ionized Mo can be ignored. Photon emission in a spectrum line ε (p, q) is dominant by the emission from atoms. It can be expressed as

$$\varepsilon(p,q) = A(p,q)\sum_{\sigma=0} R_\sigma^{(exc)}(p) n_e n_\sigma \quad , \tag{2.11}$$

where A (p, q) is fraction of the spontaneous transmission probability, n_σ denote the population density of the specified ion in the metastable state σ. The $R_\sigma^{(exc)}$ (p) is the effective contribution to the population of the upper excited level p of the transition by the excitation from the ground state and metastables. Then, the excitation photon emissivity coefficient is written as

$$PEC_\sigma^{(exc)}(p,q) = A(p,q) R_\sigma^{(exc)}(p). \tag{2.12}$$

2.5.2 Collisional-radiative (CR) models

The spectral line radiation emitted by a plasma is a powerful source of information about the conditions inside the plasma. The line intensities are proportional to the population densities of the excited levels. The distribution functions of atoms and ions over their excited states can be described by CR models. In these models, the densities of the various excited of a specific atom or ion are expressed as functions of a number of relevant parameters, such as the ground state density n_0 and the ion density n_i, the election temperature T_e and density n_e. The name of the models indicates that the densities of the excited states are determined by collisional and radiative processes and that transport phenomena can be neglected for these species.

With all these processes included, the rate at which the population density n (p) of level p changes is given by the differential equation

$$\begin{aligned} \frac{dn(p)}{dt} &= -n(p)\left\{ n_e\left[\sum_{q\neq p} C(p,q) + K(p,c)\right] + \sum_{p<q} A(p,q)\right\} \\ &+ n_e \sum_{q\neq p} n(q) C(q,p) + \sum_{q>p} n(q) A(q,p) + n_e n_i\left[\alpha(p) + \beta(p) + \beta_d(p)\right] \end{aligned} \quad , \tag{2.13}$$

where C (p, q) and K (p, c) are the rate coefficients for electron impact excitation or de-excitation and ionization, α (p), β (p), and β_d (p) are the rate coefficients for three-body, radiative and dielectronic recombination, respectively.

The complete description of the system would involve the variation with time of the population density of every bound level from a particular set of initial conditions. But in practice, the time in which the population densities of the excited levels come into equilibrium with a particular population density of the ground level, free electrons and bare nuclei is so short that it is sufficient to express these equilibrium population densities as functions of the ground level population density. This is called the quasi-steady-state-solution which allows the equation (2.13) set as zero. Then n (p) can be obtained by solving a series of coupled liner equations in terms of n_0.

In the condition of this study, the excited level population density n (p) can be expressed as

$$n(p) = R(p) n_e n_0, \tag{2.14}$$

where $R(p)$ is a function of n_e and T_e. And the photon emission rate of the $p \rightarrow q$ transition can be written as

$$A(p,q) n(p) = A(p,q) R(p) n_e n_0 = PEC(p,q) n_e n_0, \tag{2.15}$$

combined with (2.9). Thus, the photon emission coefficient can be calculated via the CR model.

2.6 Optical characterization

2.6.1 Complex refractive index

Reflectance of light from vacuum to a matter can be described as follow

$$\mathrm{R} = \left| \frac{1-n}{1+n} \right|^2, \tag{2.16}$$

where n is the refractive index of matter. The refractive index (real part) of an optical medium expresses the ratio of the speed of light in the vacuum, c, to the phase velocity in the medium v,

$$n = c / v. \tag{2.17}$$

To understand the reflection of light from a matter, it is necessary to discuss the interaction between electromagnetic wave and the matter.

In vacuum, the propagation of wave in x direction can be described by the wave equation

$$c^2 \frac{\partial^2 E(x,t)}{\partial x^2} = \frac{\partial^2 E(x,t)}{\partial t^2}, \tag{2.18}$$

where E is the electric field, and t is the time. One of the solutions of this equation can be

$$E(x,t) = E_0 \exp i(kx - \omega t), \tag{2.19}$$

where E_0 is the amplitude of the wave and k is the wave vector which is given by

$$k = 2\pi / \lambda = \omega / c, \tag{2.20}$$

where λ is the wavelength and ω is the angular frequency which is the frequency times 2π.

In matter, however, the interaction between wave and the charges (especially electrons) should be considered. The wave in matter can be described as a dampened wave. Assuming that the material of matter has no magnetic response, then the wave equation changes to

$$c^2 \frac{\partial^2 E(x,t)}{\partial x^2} = \varepsilon \frac{\partial^2 E(x,t)}{\partial t^2} + \frac{\sigma}{\varepsilon_0} \frac{\partial E(x,t)}{\partial t}, \tag{2.21}$$

where ε and ε_0 is the permittivity of the medium and vacuum, respectively, and σ is the conductivity of the medium. In equation (2.21), the second term on the left describes the damping of wave due to the friction. By substituting (2.17) and (2.20) into (2.19), the expression of wave in a medium should be

$$E(x,t) = E_0 \exp i\left(\frac{\omega n}{c} x - \omega t \right). \tag{2.22}$$

After substituting (2.22) into (2.21), the refractive index can be given by

$$n^2 = \tilde{\varepsilon}_r = \varepsilon + i\frac{\sigma}{\varepsilon_0 \omega} = \left(n_0 + i\kappa\right)^2, \tag{2.23}$$

where $\tilde{\varepsilon}_r$ is the complex relative permittivity, n_0 is the real part of the complex reflective index and κ is the imaginary part called extinction coefficient which reflect the loss of wave in the material. Thus, the reflectance of a matter can also be calculated as

$$\mathrm{R} = \frac{\left(n_0 - 1\right)^2 + \kappa^2}{\left(n_0 + 1\right)^2 + \kappa^2}. \tag{2.24}$$

2.6.2 Permittivity in dielectrics: Lorentz Model

Material can be polarized due to the motion of electrons in medium in response to the electromagnetic wave. The motion can be described by Lorentz oscillator model as follow:

$$m_e{}^2 \frac{\partial^2 r}{\partial t^2} + m_e \Gamma \frac{\partial r}{\partial t} + m_e \omega_0{}^2 r = -qE. \tag{2.25}$$

Here, the first term on the left describes the acceleration force, where r is the distance of electron which is displaced from its equilibrium position. The second term is the force from friction, where Γ is the damping rate with a unit of s^{-1}. The third term represents the restoring force during the oscillation, where ω_0 is the natural frequency. The term on the right of the equation is the electric force, where q is the charge of electron. By applying Fourier transform on (2.25), the solution of r can be given by:

$$r\left(\omega\right) = -\frac{q}{m_e}\frac{E\left(\omega\right)}{\omega_0^2 + \omega^2 + i\omega\Gamma}. \tag{2.26}$$

The polarization per unit volume $P(\omega)$ is given by

$$P\left(\omega\right) = n_e q r\left(\omega\right), \tag{2.27}$$

which also can be written by

$$P\left(\omega\right) = \varepsilon_0 \chi\left(\omega\right) E\left(\omega\right), \tag{2.28}$$

where $\chi(\omega)$ is called the electric susceptibility and is a measure of how easily an electric field can polarize the material. This leads to an expression of the electric susceptibility:

$$\chi\left(\omega\right) = \frac{\omega_p}{\omega_0^2 + \omega^2 + i\omega\Gamma}, \tag{2.29}$$

where $\omega_p = \dfrac{n_e q^2}{\varepsilon_0 m_e}$ is the plasma frequency.

For dielectrics, material polarization should be incorporated into the electric constitutive relation as follow:

$$D = \varepsilon_0 E\left(\omega\right) + P\left(\omega\right) = \varepsilon_0\left(1 + \chi\left(\omega\right)\right)E\left(\omega\right), \tag{2.30}$$

where D is the displacement field which also can be written in terms of the complex relative permittivity

$$D = \varepsilon_0 \tilde{\varepsilon}_r . \tag{2.31}$$

Then, $\tilde{\varepsilon}_r$ is obtained by combining (2.30) and (2.31)

$$\tilde{\varepsilon}_r = 1 + \frac{\omega_p^2}{\omega_0^2 + \omega^2 + i\omega\Gamma} . \tag{2.32}$$

Split (2.32) into real and imaginary parts:

$$\tilde{\varepsilon}_r = \varepsilon_r'(\omega) + i\varepsilon_r''(\omega) = 1 + \omega_p^2 \frac{\omega_0^2 - \omega^2}{\left(\omega_0^2 - \omega^2\right)^2 + \omega^2\Gamma^2} + i\omega_p^2 \frac{\omega\Gamma}{\left(\omega_0^2 - \omega^2\right)^2 + \omega^2\Gamma^2} .$$

Thus, the real part and the imaginary part of the complex refractive index can be written by:

$$n_0 = \sqrt{\frac{|\tilde{\varepsilon}_r| + \varepsilon_r'}{2}} , \quad \kappa = \sqrt{\frac{|\tilde{\varepsilon}_r| - \varepsilon_r'}{2}} .$$

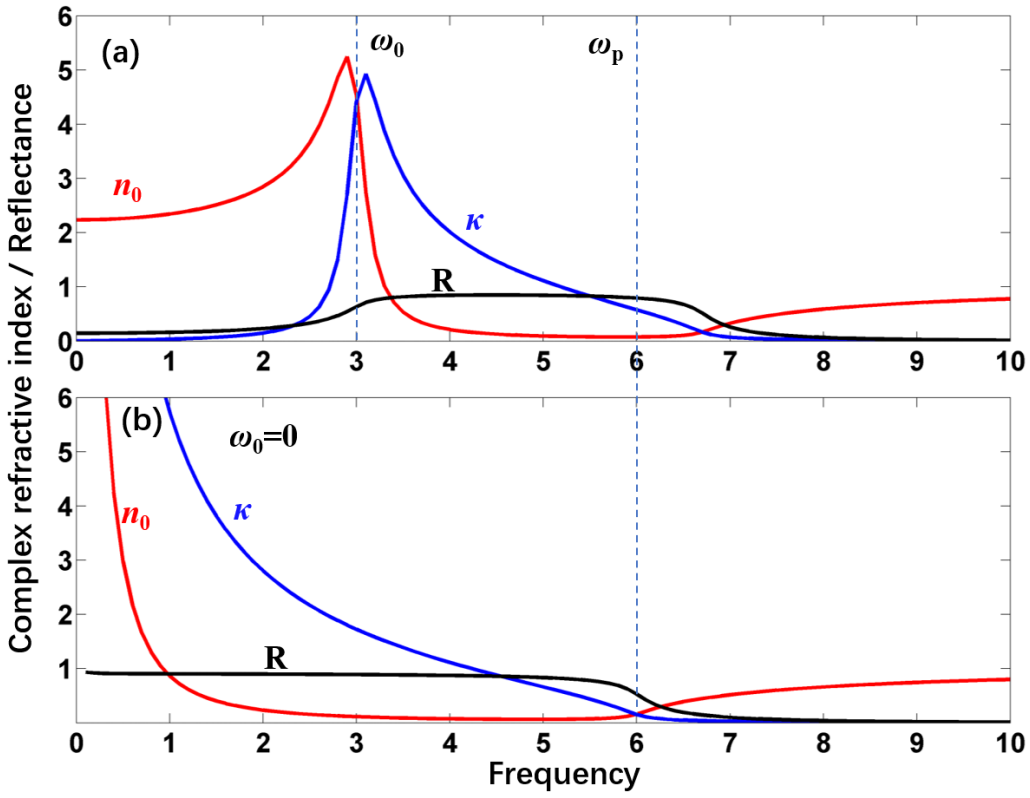

Figure 2.5 Real (red) and imaginary (blue) part of the complex refractive index and the reflectance (black) as a function of the frequency of incident light with ω_p=6, Γ=0.3, ω_0=3 in (a), and ω_0=0 in (b).

Figure 2.5 (a) shows the real and imaginary part of the complex refractive index and the reflectance curve for dielectric. High reflectance of dielectric appears at the region of frequency between ω_0 and ω_p.

In metal, because electrons are almost free, there is no restoring force. The ω_0 can be treated as zero, as shown in Figure 2.5 (b). It shows that, the reflectance of metal close to 1 below the plasma frequency but acts like vacuum above the plasma frequency.

Moreover, the interband transition of dielectric should be considered in real reflection case. For insulators, the band gap is so large that the transition only become important at very high energy. However, for semiconductors, the optical absorption due to the interband transition of elections just occurs at the energy of visible light. Two peaks of reflection curve of Si at 287 and 360 nm, shown in Chapter 5, are corresponding to the interband transition of Si in (100) and (111) direction, respectively.

2.6.3 Morphology effect on optical scattering

Scattering of light is a function of wavelength and the size of object. For sphere object, the size of project can be expressed by the ratio

$$a = \frac{2\pi r}{\lambda}, \tag{2.33}$$

where r is the radius of the particle, λ is the wavelength of light. When a is much smaller than 1, the intensity of scattering light is proportional to the inverse of fourth power of the wavelength, which called Rayleigh scattering. When a is close to 1, the phenomenon shifts to the Mie scattering, which means most of the light scattered continue along the incident direction. When a is much larger then 1, the scattering can be explained by geometric analysis.

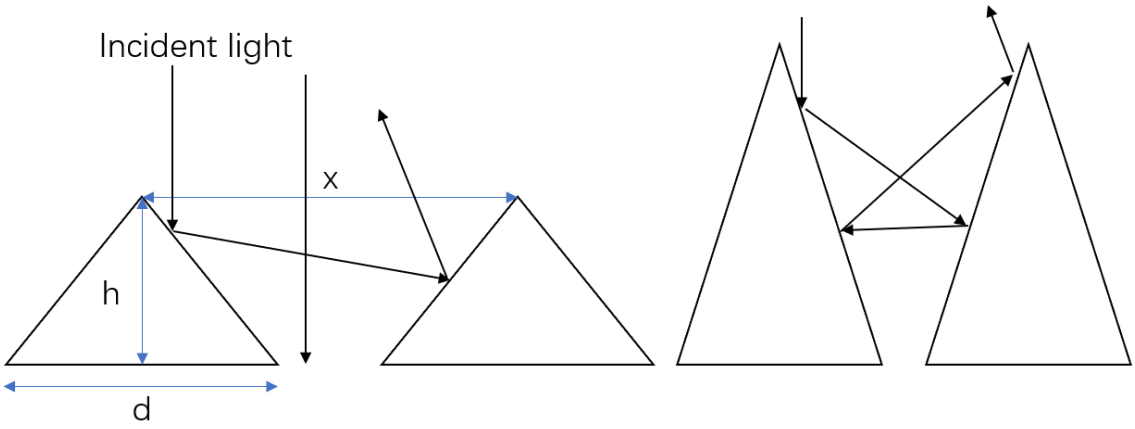

Figure 2.6 Schematic of optical reflection between cones with different geometry. h, d, and x are the heigh, diameter, distance of cones, respectively.

In this study, despite the shape of objects on the Si surface is cone, the phenomenon of optical reflection can be partially understood according to the scattering theory above. When the diameter is smaller than 100 nm, the interaction between light and cones should be considered as Mie scattering. When the diameter of cone is larger than 100 nm, the geometry of nanocone should be taken into account. Light incident on the Si surface reflects multiply between cones leading to the low reflection. In this condition, the reflection of light is influenced by the heigh and diameter of the cone, as well as the distance between cones, as shown in Figure 2.6.

References

[1] Q. Shi, S. Kajita, N. Ohno, M. Tokitani, D. Nagata, & S. Y. Feng, The Influence of Impurities on the Formation of Nanocone Structures on Silicon Surface Irradiated by Low Energy Helium Plasma, Journal of Applied Physics **128** (2020) 023301.

[2] K. Asai, N. Yoshida, N. Ohno, S. Kajita, H. Tanaka, M. Yajima, & D. Nagata, Microstructure and Retention in He-W Co-Deposition Layer, Plasma and Fusion Research: Rapid Communication **15** (2020) 1201004.

[3] K. Miyaguchi, S. Kajita, H. Tanaka, & N. Ohno, Fabrication of Nanostructure Ti Thin Film with Ti Deposition in He Plasma, Japanese Journal of Applied Physics **60** (2021) 038004.

[4] S. Kajita, S. Kado, A. Okamoto, & S. Tanaka, Application of Eclipse Laser Photodetachment Technique to Electron Sheath Thickness and Collection Region Measurements, Physical Review E **70** (2004) 066403.

[5] W.R. Grove, VII. On the Electro-chemical Polarity of Gases, Philosophical Transactions of the Royal Society of London **142** (1852) 87–101.

[6] P. Sigmund, Theory of sputtering. I. Sputtering Yield of Amorphous and Polycrystalline Targets, Physical Review **187** (1969) 383–416.

[7] W. Eckstein, C. Garcla-Rosales, J. Roth, & W. Ottenberger, Sputtering Data, Report IPP 9/82, Max-Planck-Institut f'tir Plasmaphysik: Garching, Germany, 1993.

[8] H. Gnaser, Energy and Angular Distributions of Sputtered Species Sputtering by Particle Bombardment, In: Sputtering by Particle Bombardment, Topics in Applied Physics **110**, Springer: Berlin, Heidelberg, 2007, 231–328.

[9] W. Eckstein, & V. Philipps, Physical Sputtering and Radiation-enhanced Sublimation, In: W.O. Hofer, J. Roth (Eds.), Physical Processes in the Interaction of Fusion Plasmas with Solids, Academic Press: San Diego, 1996, 93–133.

[10] W. Eckstein, Calculated Sputtering, Reflection and Range Values, Report IPP 9/132, Max-Planck Institut für Plasmaphysik: Garching, Germany, 2002.

[11] S. Dai, S. Liu, J. Sun, A. Kirschner, G. Kawamura, D. Tskhakaya, R.Ding, G. Luo, & D. Wang, Modelling of Surface Evolution of Rough Surface on Divertor Target in Fusion Devices, Journal of Nuclear Materials **464** (2015) 372–376.

[12] K. Ohya, Y. Kikuhara, K. Inai, A. Kirschner, D. Borodin, A. Ito, H. Nakamura, & T. Tanabe, Simulation of Hydrocarbon Reflection from Carbon and Tungsten Surfaces and Its Impact on Codeposition Patterns on Plasma Facing Components, Journal of Nuclear Materials **390** (2009) 72–75.

[13] Y. Yamamura, N. Matsunami, & N. Itoh, Theoretical Studies on an Empirical Formula for Sputtering Yield at Normal Incidence, Radiation Effects and Defects in Solids **71** (1983) 65–86.

[14] Y. Yamamura, & Y. Mizuno, Low-energy Sputterings with the Monte Carlo Program Acat, IPPJ-AM-40, Institute of Plasma Physics, Nagoya University, 1985.

[15] D. P. Kroese, T. Brereton, T. Taimre, & Z. I. Botev, Why the Monte Carlo Method is so Important Today, WIREs Computational Statistics **6** (2014) 386–392.

[16] N. Metropolis, A. W. Rosenbluth, M. Rosenbluth, A. H. Teller, & E. Teller, Equation of State Calculations by Fast Computing Machines, Journal of Chemical Physics **21** (1953) 1087–1092.

[17] W. K. Hastings, Monte Carlo Sampling Methods Using Markov Chains and Their Applications, Biometrika **57** (1970) 97–109.

[18] J. S. Liu, F. Liang, & W. H. Wong, The Multiple-Try Method and Local Optimization in Metropolis Sampling, Journal of the American Statistical Association **95** (2000) 121–134.

[19] J. C. Spall, Estimation via Markov Chain Monte Carlo, IEEE Control Systems Magazine **23** (2003) 34–45.
[20] S. D. Hill, & J. C. Spall, Stationarity and Convergence of the Metropolis-Hastings Algorithm: Insights into Theoretical Aspects, IEEE Control Systems Magazine **39** (2019) 56–67.

Chapter 3. Influence of impurities on the formation of nanocones structure on silicon surface irradiated by low energy helium ions

3.1 Introduction

Black silicon (Si) is a prominent material in solar cell applications [1, 2]. Because of the nanostructures formed on an Si surface, photons can be captured, leading to the movement of electrons or vacancies in the substrate. Moreover, the array of high aspect ratios of vertical Si nanocones allows the black Si to be the field emitter [3]. However, conventional methods of fabricating black Si (for example, the reactive ion etching) are relatively complicated, because of the usage of different species such as oxygen and fluorine with high energy and the need for some masks [3, 4]. Recently, by using helium (He) plasma irradiation on doped silicon with a relatively low ion energy (approximately 50 eV), nanocones were obtained on an Si substrate [5].

Several studies have investigated the formation of Si nanostructures by He plasma irradiation. At the surface temperature of ~600 °C and ion energy of 55 eV, Takamura obtained different characters of nanocones, which resulted in the appearance of black and whitish-blue Si surfaces [6]. At the same sample temperature with higher incident ion energy (100 eV), nanocones were formed on the Si surface with different crystal orientations, (111) and (100) [7]. From field emission scanning electron microscope (FE-SEM) observations, there was no evidence to prove that crystal orientation affected the configuration of Si nanostructures. Moreover, a reduction in the sample temperature appeared to decrease the size of cones. Thomson conducted irradiation on Si at a much lower energy of ~30 eV [8]. Some nanostructures other than cone shape were formed, but only when the sample temperature was higher than 630 °C. While various nanostructures have been observed in a wide range of experimental conditions, the relationship between the parameter of the irradiation condition and the behavior of Si nanostructure formation has not been discussed. Moreover, the formation of the nanostructures has yet to be fully understood.

In this study, to understand the formation mechanism including the impurity effects, He plasma irradiations on Si samples were performed using the linear plasma generator Compact Nagoya University DIvertor Simulator (Co-NAGDIS) [9]. The experimental conditions (such as sample temperature and flux) were investigated independently. Nanocone structures formed on Cr materials by plasma irradiation in PISCES-A, PSI-2, and NAGDIS-II, were reported by Nishijima [10]. Impurities such as molybdenum (Mo) and tantalum (Ta), which are thought to originated from the sample holding cap or cover, have been considered as the main reason of the nanocones formation. Herein, two types of sample mask with different materials were used: (Mo) and tungsten (W) to change the amount of impurities. The relationship between morphology changes and the amount of impurities on surfaces will be shown in this study.

3.2 Experimental setup

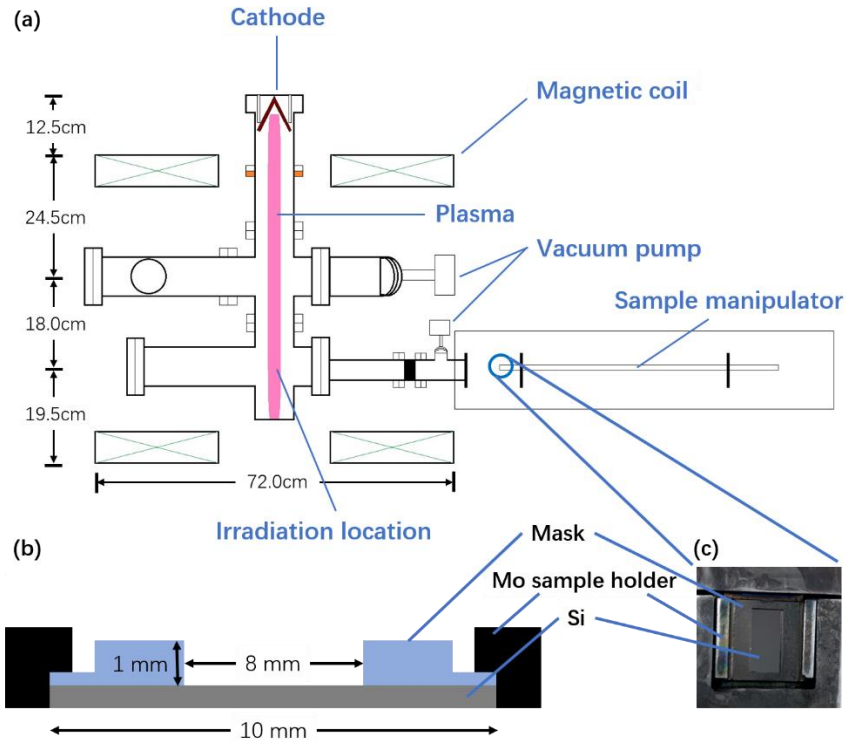

Figure 3.1 Schematic of Co-NAGDIS (a) and sample mask (b, c).

A schematic of Co-NAGDIS is shown in Figure 3.1. The location of the sample with respect to the sample mask and holder is shown in Figure 3.1 (b, c). The sample and mask were fixed by sample holders and faced the plasma flow at the irradiation location. A meander (LaB_6) was used for the cathode and the background pressure was 9×10^{-5} Pa before the discharge. N-type Si (111) samples with a thickness of 0.5 mm and resistivity of 1000 Ωcm were cut into 10 mm × 10 mm squares and installed on the sample manipulator. The mask of the Si sample is shown as the inset in Figure 3.1. In this study, the He ion flux was in the range of 4 to 9×10^{21} $m^{-2}s^{-1}$. To control the sample temperature, electron heating was used to increase the sample temperature to the target value before irradiation. Then, the sample was negatively biased at -54 V; considering the space potential of 3 V, the ion energy was approximately 57 eV. The sample temperature was measured by a thermal couple touching the back of the sample at the center. The airflow beneath the sample could be used to adjust the sample temperature during irradiation. A Langmuir probe was used to measure the parameters of the plasma condition 30 mm away from the sample.

3.3 Results and discussion

3.3.1 Black and white Si

SEM micrographs of two typical nanocone structures on the irradiated Si surface are shown in Figure 3.2 (a, c) for case 1 and (b, d) for case 2. Figure 3.2 (a, b) presents a tilted view at 30° from normal. Figure 3.2 (c, d) are top views of the SEM micrographs. The experimental conditions for cases 1 and 2 were set as shown in Table 1: ion fluence Φ^1_{He} = 3.30×10^{25} m^{-2}, Φ^2_{He} = 3.24×10^{25} m^{-2}, sample temperature, T_1 = 470 ℃, T_2 = 380 ℃, material of mask, Mo and W, respectively. The effects of these parameters will be discussed in Section 3.3.2. As shown in the inset of figure 3.2, case 1 shows a black appearance (black Si) to the naked eye, while case 2 corresponds to a white appearance (white Si). The

irradiated area of the samples is marked by the red dashed lines. This difference in appearance is probably due to the different sizes and distributions of the nanocones laid on the surface.

Table 3.1 Experimental conditions for cases 1 and 2.

	Φ_{He} (10^{25} m^{-2})	T (°C)	Mask	Appearance
Case 1	3.30	470	Mo	Black Si
Case 2	3.24	380	W	White Si

To illustrate the difference between black and white Si more specifically, we analyzed the SEM images in Figure 3.2 (c, d) were analyzed using the Image–J program [11]. As shown in Figure 3.2 (c, d), the cone structures display a lighter color (i.e., a larger gray value) than the substrate region. Figure 3.3 (a) is the fraction distribution of the gray value for black and white Si. The high peak for the white Si case means that less area has been changed by nanocones than the black case. The nanocones can be identified by setting a threshold for the gray value refer to Figure 3.3 (a) in Image–J analysis. The threshold values used in this study were 135 and 105 for the black and white Si cases, respectively. The number density distribution of nanocones as a function of the area of cone was obtained as shown in Figure 3.3 (b). It can be observed that the size of the nanocones is widely distributed from 0.0001 to > 1 μm^2 for the white Si sample. Conversely, the size of nanocones is concentrated in a narrow range for black Si. This indicates, the surface morphology for black Si is more uniform than that of white Si. Moreover, the distribution of nanocones on black Si is denser compared to white Si.

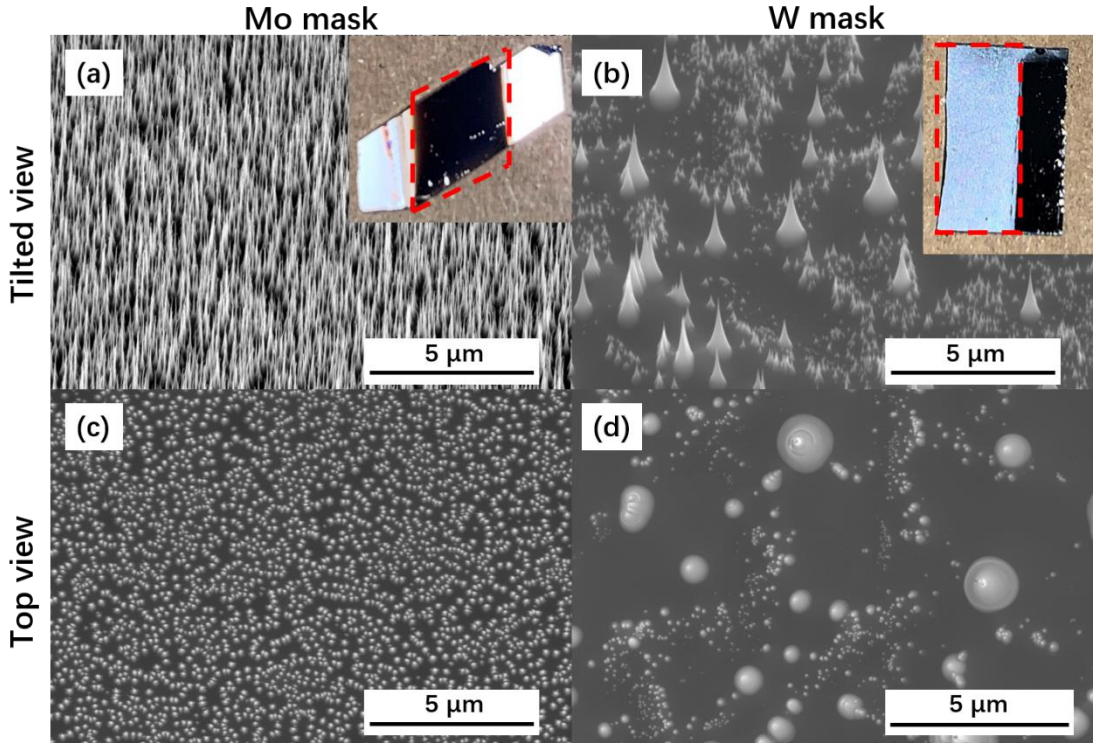

Figure 3.2 The nanocone structure of case 1 (a, c) and case 2 (b, d) Si observed form SEM in tilting view of 30° (a, b) and top view (c, d). The irradiation region of case 1 and case 2 are shown inset (a) and

(b), respectively. For case 1, He ion fluence Φ^1_{He} = 3.3×10^{25} m^{-2}, sample temperature T_1 = 470 ℃. For case 2, Φ^2_{He} = 3.24×10^{25} m^{-2}, T_2 = 380 ℃.

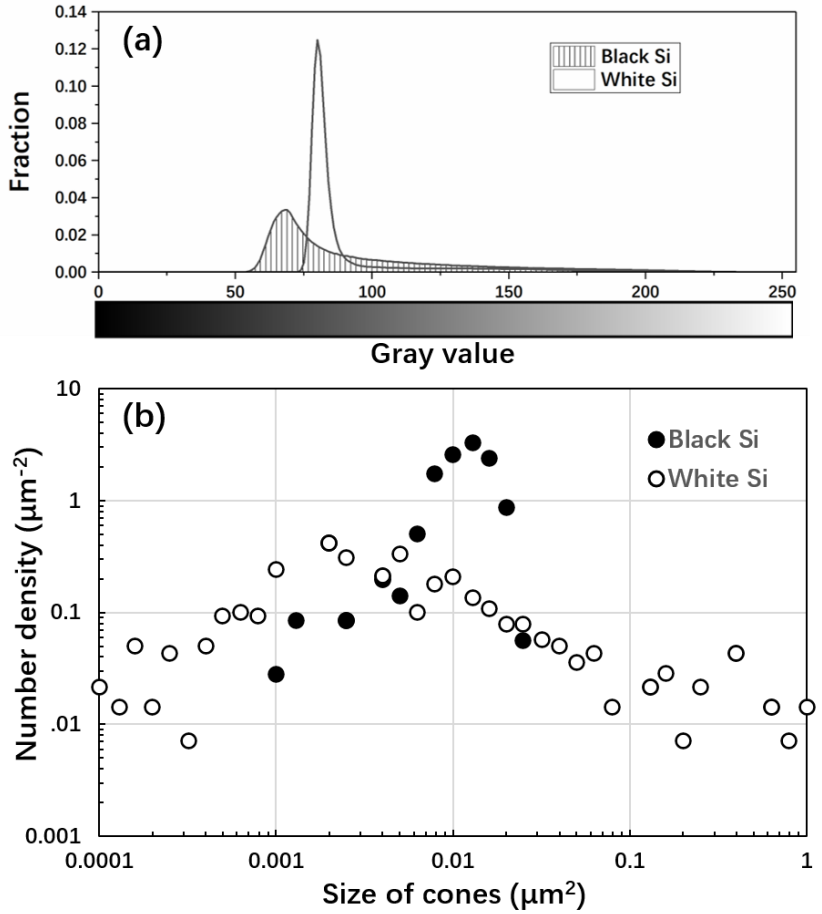

Figure 3.3 (a) The fraction of gray value distribution of black Si (figure 3.2 (c)) and white Si (figure 3.2 (d)). (b) The density distribution of the different sizes of cones from the top view for black (solid dots) and white Si (open dots).

The reflectance of black and white Si was measured with an Ultraviolet–visible (UV–VIS) spectrophotometer, as shown in Figure 3.4. The white Si had a slightly lower reflectance than the non-irradiated sample. However, the reflectance of black Si significantly decreased. The uniformity and high density of the nanocone structures on the black Si has an effect on trapping light. This result also supports the premise that He plasma-induced black Si can be used as a photon absorption material.

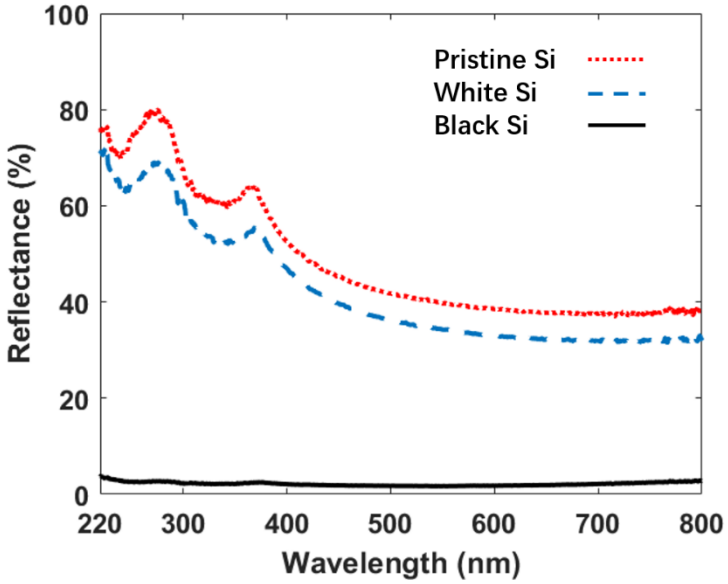

Figure 3.4 The reflectance of pristine, white (case 2) and black Si (case 1), which are shown in dot red, dashed blue, and solid black lines, respectively.

3.3.2 Dependence of impurity

Based on this cognition of black and white Si, this experiment conducted several experiments in various He ion fluences and sample temperatures with Mo and W masks. The He ion fluences and sample temperatures were in the ranges of 1.5×10^{25} m^{-2} < Φ_{He} < 4.2×10^{25} m^{-2} and T_{Si} ~330–500 °C, respectively. Figure 3.5 shows the irradiation results of Si samples with different sample temperatures and ion fluences. Even though the ion fluence and sample temperature were changed, the appearance of black and white Si only appeared to depend on the sample mask material. One exception to this, showing a brown surface, will be discussed in a later section. This dependence on the sample mask implies that the mask material (impurity) might affect the formation of nanocones.

XPS was used to detect the species of impurities on the Si surface. Figure 3.6 shows the XPS survey spectra for pristine, white, and black Si. Only O, C, and Si are observed on pristine Si, while clear Mo signals are found on the black Si. For white Si with a W mask, a small W was identified at the binding energy of 32 eV. Usually, the amount of Mo or W atoms sputtered by He ions could be ignored at an energy of 57 eV. However, considering the ratio of background to the operational pressure, the proportion of impurities was approximately 0.05%. That level of impurity gas (presumably O, which has a sputtering yield of 2×10^{-2} at the same energy) might contributed to the sputtering, in the cases identified in NAGDIS-II for the formation of nano tendril bundles [12]. It should be noted that the sputtering yield for O on Mo material is 20 times larger than that on W at the same energy. Additionally, the smaller peak of Si for black Si compared with pristine and white Si cases manifests that the surface of the sample is massively covered by Mo.

Figure 3.7 shows the ratios of impurities, which are Mo and W, as a function of the number density of nanocones on Si sample surfaces. As mentioned in section 3.1, the number density of nanocones for black Si was much higher than white Si. Moreover, the impurity ratio increased with the number density of nanocones. The appearance of black and white Si after the exposure by He plasma could probably be explained by the ratios of impurities deposited on the Si surface.

For the previously mentioned brown Si case, which had high density but a non-uniform nanocones structure, Mo was also detected on the surface. These additional impurities may cause more nanocones. Although the origin of Mo was ambiguous, one possibility was that Mo was deposited somewhere on the W mask. Since the condition is ambiguous and difficult to discuss further for the brown case, this study only focus on black and white cases.

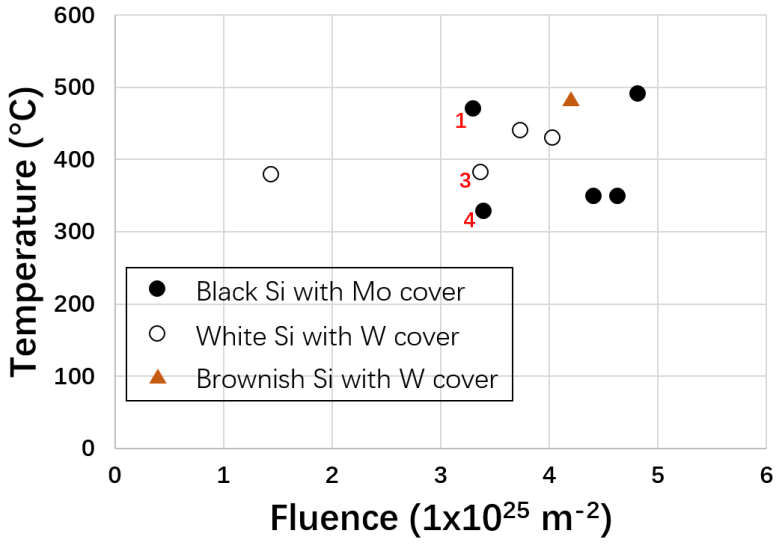

Figure 3.5 Results of Si samples with Mo and W masks irradiated by He plasma in different sample temperatures and ion fluence. The ion flux and incident ion energy are $10 \pm 1\times10^{21}$ $m^{-2}s^{-1}$ and 57 ± 1 eV, respectively, for all these cases. Some of the cases mentioned in other sections are marked in red numbers.

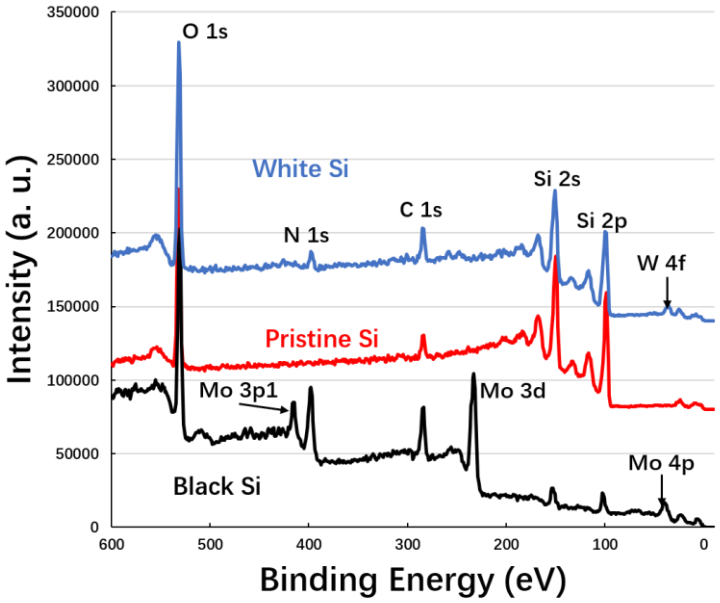

Figure 3.6 XPS survey spectra for pristine, white and black Si.

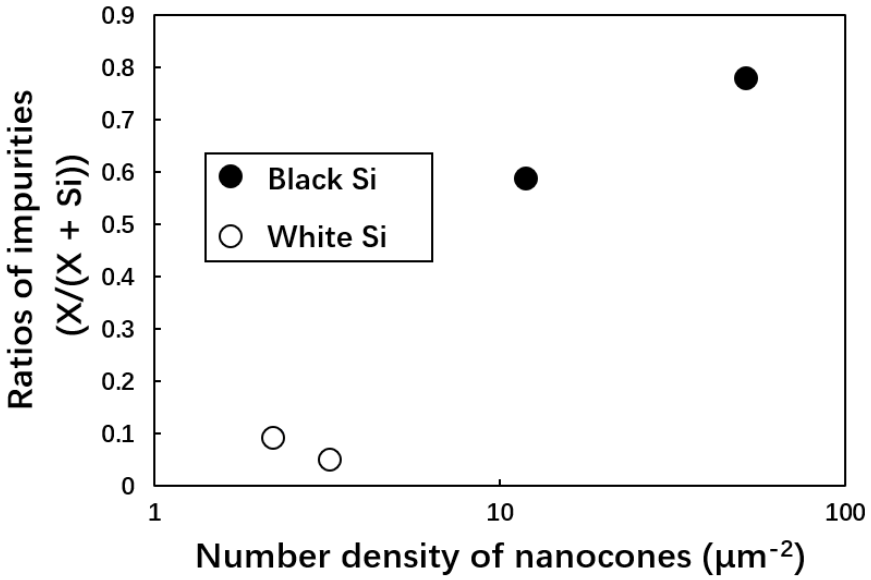

Figure 3.7 Ratios of impurities as a function of the number density of nanocones on black and white Si surface. Black and white Si cases are shown in solid and open dots, respectively. The ratios of impurities are deduced by (X / (X + Si)), which X means species of impurities. Number density is calculated in the same way as figure 3.3.

3.3.3 Sputtering yield reduction

Figure 3.8 shows the height distribution of the irradiated region of white (case 3) and black (case 4) Si samples measured by a laser microscope (VK-9710, Keyence, Japan). The ion fluence and sample temperature for the cases 3 and 4 were $\Phi_{He} = 3.36\times10^{25}$ m^{-2}, and T = 380 °C, and $\Phi_{He} = 3.4\times10^{25}$ m^{-2}, and T = 330 °C, respectively, as shown in Table 3.8. The height of the initial surface was set at the same level for a convenient comparison of the erosion depth. Considering the incident ion energy and fluence were nearly the same for these two cases, the erosion depth, d, should be close. However, the erosion depth for black Si was approximately 3 μm, which was much shallower than that for white Si (7 μm). Because the erosion depth is much larger than the height of cone, the volume of nanocones was ignored when calculating the real sputtering yield. The fluence of sputtered Si can be simply deduced by $\Phi_{Si} = d\times\rho_{Si}\times NA/M_{Si}$, where ρ_{Si} = 2328.3 kg×m^{-3} is the density of Si, M_{Si} = 28.1 g×mol^{-1} is the molar mass of Si, and NA is mole number. Thus, the fluences of sputtered Si atoms for black and white cases were estimated to be 1.5×10^{23} and 3.5×10^{23} m^{-2}, respectively. The real sputtering yield deduced from $Y = \Phi_{Si} / \Phi_{He}$ were obtained for cases 3 and 4 as $Y_{Black} \approx 4.5\times10^{-3}$ and $Y_{White} \approx 1.0\times10^{-2}$. The theoretical sputtering yield is $Y_{A\text{-}CAT} = 1.9\times10^{-2}$ as calculated by the Monte Carlo code A-CAT [13] under an ion energy of 57 eV. The significant decrease of sputtering yield for the black Si case was probably because of the large amount of Mo (which has a lower sputtering yield compared with Si) impurities deposited on its surface. When using the W mask, the density of W was much lower than the Mo mask; white Si has a sputtering yield close to the theoretical value. The sputtering yield will decrease to a saturated state as a function of time, as reported in [9]. This indicates that the surface morphology may affect the actual sputtering yield due to the angular dependence of sputtering yield or line-of-sight deposition [12, 14].

Table 3.2 Experimental conditions for cases 1 and 2.

	Φ_{He} (10^{25} m^{-2})	T (°C)	Mask	Appearance
Case 3	3.36	380	W	White Si
Case 4	3.4	330	Mo	Black Si

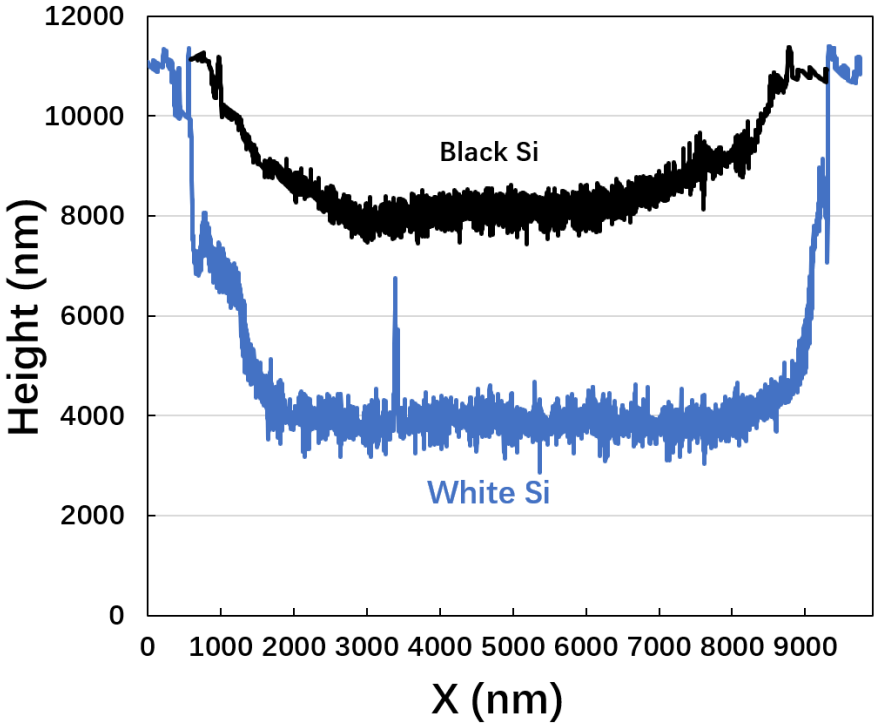

Figure 3.8 Height distribution of the Si sample after He plasma irradiation form one boundary between exposure region and cover to the other. The He ion energy is 57 eV for both cases, and the ion fluences are almost the same as shown in figure 3.5 cases 3 (white Si) and 4 (black Si).

3.3.4 TEM observation

As shown in Figure 3.9, a transmission electron microscope (TEM) was applied to examine the positions where impurities were deposited. Black dots, which can be observed on the upper part (especially on the tip) of the cone, are likely resulted from impurities. From Figures 3.9 (b) and (c), though the main domain of the cone remains crystal nature, some black stripes resulted from amorphous indicate the probable surface defects and diffusion. Furthermore, He bubbles are observed at the bottom of only few cones.

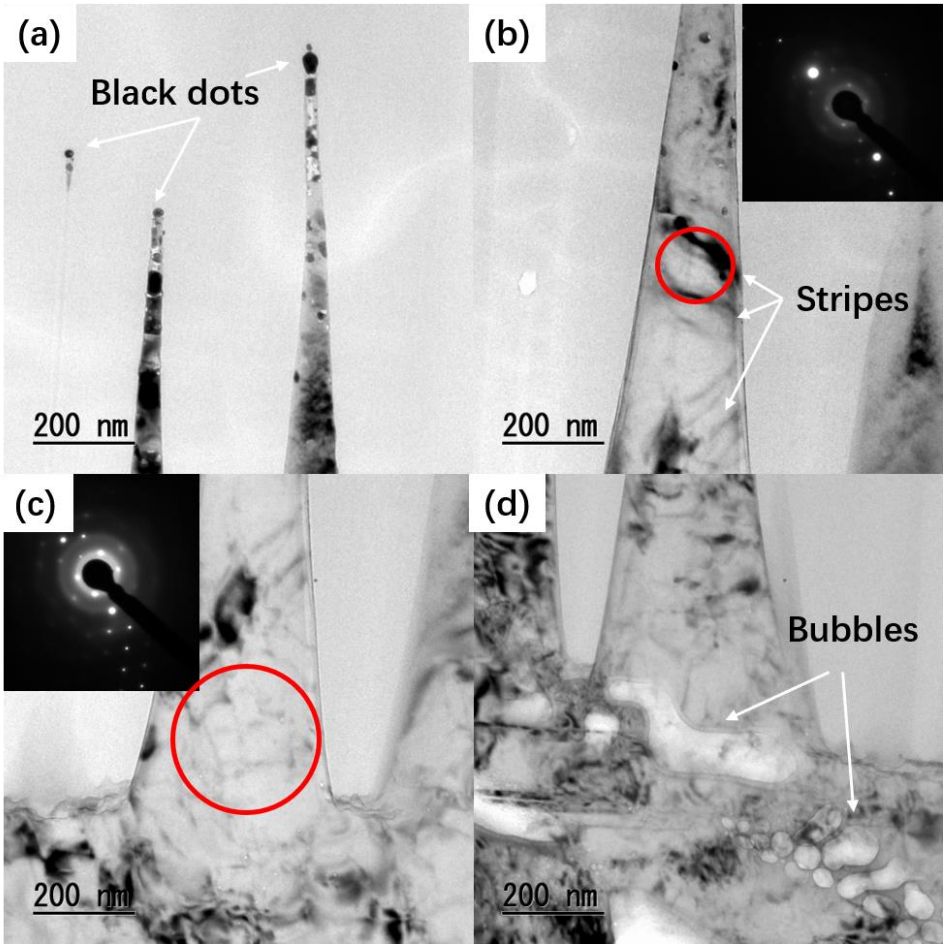

Figure 3.9 Transmission electron micrographs of different segments of nanocones. The inset in (b) and (c) are showing the electron diffraction pattern of which circled in red.

3.3.5 Discussion of the mechanism on the cone formation

The formation of nanostructures on Si surfaces bombarded with various ion species have been reported over the decades. Usually, impurity seeds are considered an essential factor for fabricating nanostructures. For example, nanostructures can only be observed after impurity atoms are introduced during the ion bombardment at room temperature [15, 16]. Oxides or carbon compounds, which have a lower sputtering yield than the pure material, may result to form nanocones. After He plasma exposure, a slightly shifting of the Si 2p peak of region XPS scan manifests the presence of SiC on the surface [17]. Although a similar result, was found in this study (was not presented), here the effect of impurities is taken into consideration as a major cause of nanocones, since the ratio of impurities shows a dependence on the number density of cones, As mentioned in Section 3.3.2.

The reduction of sputtering yield for an abundant impurity case is in good agreement with Nishijima's results, which indicated that the intensity of sputtered target atoms decreased rapidly when heavier impurities were supplied by the sample cover or cap of the top [9]. Thus, impurities can shield the substrate surface, leading to roughness at the initial stage.

The development of nanocones is well known driven by Bradley-Harper (BH) instability [18], which means the erosion for a normal ion incident on the convex is slower than that of the concave, and the

angular dependence of sputtering yield [19]. Starting from a simple convex structure, a cone was obtained by simulation works taking various sputtering yield and ion reflection into account.

Surface stress is another candidate that can result in cone-like structures. As discussed in [20], protuberances on the surface were caused by the increasing of ion-induced surface stress, at which point the crystal structures were ruined by the implantation of impurities. From a stress study of an Si sample, in [16] it was suggested that the surface tensile stress would be enhanced by Mo seeding, resulting in instability and the formation of nanodots. Because of the relatively low incident energy, the cone retained good crystalline nature in both our case and in [6]. However, the presence of He bubbles and amorphous stripes indicates that He ions are capable of penetrating the substrate, prompting surface diffusion [21]. From the theoretical method, the displacement energy E_m can be deduced as follows:

$$E_m = E_i \frac{4M_1M_2}{(M_1+M_2)^2}\cos^2\theta\,. \tag{3.1}$$

Here, E_i is the ion energy, M_1 and M_2 are the ions and substrate atoms, and θ is the local incident angle. Taking E_m as 12.5 eV [22], the maximum local angle to displace an Si atom in the experiment is ~56°, which is smaller than the angle for the maximum sputtering yield (~70° [23]). Under this condition, the tip of the cone shrinks [19], driven by the surface diffusion flow. This is in good agreement with the previous results shown in Figures 3.2 and 3.9. Accordingly, the cone will not be diminished during continuous ion bombardment, because the smaller nanocones existing on the white Si surface are recently formed.

Based on the previous discussions, we can take inspect the schematic of nanocones formation. Figure 3.10 showing the evolution of the surface morphology for white and black Si. For white Si, the whole process is described as follows: First, insufficient W impurities sputtered from the sample mask by O deposited on the Si surface (Figure 3.10 (a)). Second, due to the lower sputtering yield of He on W compared with Si, small protuberances are formed (Figure 3.10 (b)). Then, the effect of BH instability and the angular dependence of sputtering yield reshape the protuberances into nanocones (Figure 3.10 (c)). The tip of the cone is then sharpened by the surface diffusion flow of Si. Because continuously arriving impurities result in new nanocones formation, the surface shows the coexistence of both large and small sizes of cones (Figure 3.10 (d)). For black Si, because of the covering of the abundant Mo impurities, the formation of nanocones is saturated at an early stage. Therefore, uniform and dense nanocones are displayed after plasma irradiation for 60 min.

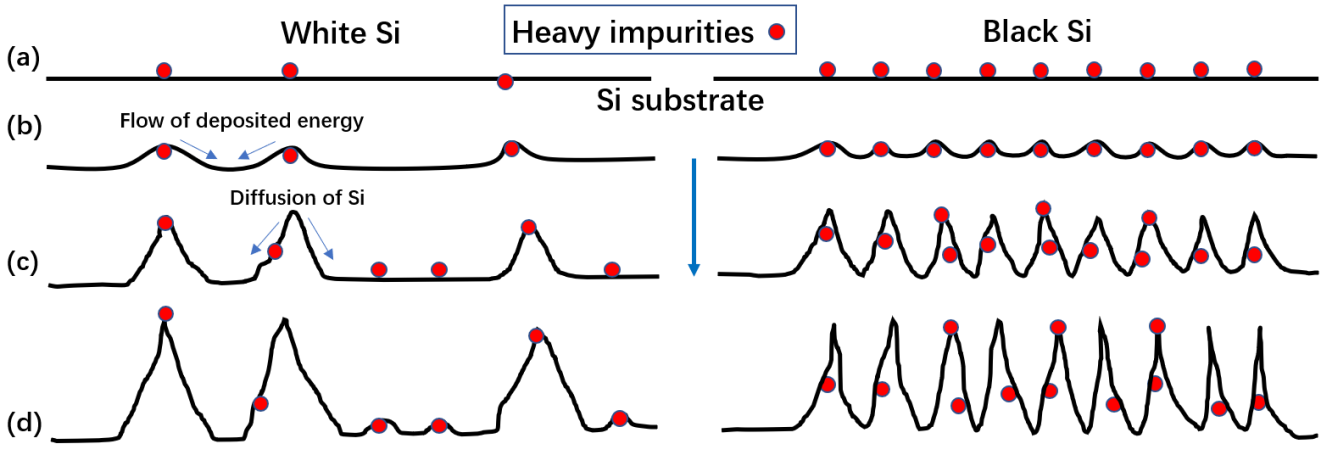

Figure 3.10 Schematic of the nanocones formation for white and black Si as the time evolution from (a) to (d).

3.4 Summary

In this study, N-type Si samples, partially covered with Mo or W, were irradiated by low energy He plasma. This resulted in turning the exposed region either black or white. The distribution of nanocone structures formed on the surface and the optical properties of the rough surface were both analyzed to identify the black and white Si. While these two types of results have no clear dependence on the sample temperature or ion fluence, they were influenced by the material of the sample mask. Impurities of Mo and W were detected on the black and white Si samples, respectively. The ratios of impurities have a relationship with the number density of nanocones, resulting in the different appearance of surface morphology (i.e., black and white Si). Moreover, measurements of erosion depth of black and white Si cases revealed that the real sputtering yield for black Si is less than half of the theoretical value, while white Si demonstrates slightly smaller results. Thus, the mechanism of nanocone formation is considered a result of the impurity shield effect and BH instability.

Further studies are required to confirm this conclusion. For an example, a map of impurity distribution on nanocones measured by EDX could help to confirm the behavior of impurities. The black spots (if verified as impurities) are more likely to be agglomerate clusters, which should be affected by sample temperature. However, the range of sample temperatures in those cases was relatively narrow due to the capacity of Co-NAGDIS. The effect of temperature cannot be neglected when the range of temperature is increased. Section 5 will discuss further about the impurity flux dependence with a biased Mo wire in front of the Si target, similar to the situation done using W target [24]. Moreover, the approximate calculation of sputtering yield in this study is expected to be improved. Section 4 will discuss this by simulation approach using a three-dimensional Monte-Carlo code SURO [25, 26], which involves factors such as surface evolution, particle reflection, redeposition, and effect of angular dependence on sputtering yield. This will allow us to reproduce nanocone formation and calculate the real sputtering yield.

References

[1] M. Kanechika, N. Sugimoto, & Y. Mitsushima, Control of Shape of Silicon Needles Fabricated by Highly Selective Anisotropic Dry Etching, Journal of Vacuum Science & Technology B: Microelectronics and Nanometer Structures **20** (2002) 1298–1302.

[2] J. Oh, H.-C. Yuan, & H. M. Branz, Black Silicon with Controllable Macropore Array for Enhanced Photoelectrochemical Performance, Nature Nanotech **7** (2012) 743–748.

[3] S.A. Guerrera, & A.I. Akinwande, Nanofabrication of Arrays of Silicon Field Emitters with Vertical Silicon Nanowire Current Limiters and Self-aligned Gates, Nanotechnology **27** (2016) 295302.

[4] M. Steglish, T. Kasebier, M. Zilk, T. Pertsch, E.-B. Kley, & A. Tunnermann, The Structural and Optical Properties of Black Silicon by Inductively Coupled Plasma Reactive Ion Etching, Journal of Applied Physics **116** (2014) 173503.

[5] S. Takamura, Y. Kikuchi, K. Yamada, S. Maenaka, K. Fujita, & Y. Uesugi, Nanostructure Formation on Silicon Surfaces by Using Low Energy Helium Plasma Exposure, Japanese Journal of Applied Physics **55** (2016) 120301.

[6] S. Takamura, T. Aota, H. Iwata, S. Maenaka, K. Fujita, Y. Kikuchi, & Y. Uesugi, Black Silicon with Nanostructured Surface Formed by Low Energy Helium Plasma Irradiation, Applied Surface Science **487** (2019) 755–765.

[7] T. J. Novakowski, J. K. Tripathei, & A. Hassanein, Silicon Nanocone Formation via Low-energy Helium Ion Sputtering, Journal of Vacuum Science & Technology B **36** (2018) 051202.

[8] M. Thompson, L. Magyar, & C. Corr, Nanoscale Modification of Silicon and Germanium Surfaces Exposed to Low-energy Helium Plasma, Scientific Reports **9** (2019) 10099.

[9] K. Asai, N. Yoshida, N. Ohno, S. Kajita, H. Tanaka, M. Yajima, & D. Nagata, Microstructure and Retention in He-W Co-Deposition Layer, Plasma and Fusion Research: Rapid Communication **15** (2020) 1201004.

[10] D. Nishijima, A. Kreter, M. J. Baldwin, D. Borodin, A. Eksaeva, D. Hwangbo, S. Kajita, M. Miyamoto, N. Ohno, M. Patino, A. Pospieszczyk, M. Rasinski, T. Schlummer, A. Terra, & R. P. Doerner, Influence of Heavier Impurity Deposition on Surface Morphology Development and Sputtering Behavior Explored in Multiple Linear Plasma Devices, Nuclear Materials and Energy **18** (2019) 67–71.

[11] J. Schindelin, I. Arganda-Carreras, E. Frise, V. Kaynig, M. Longair, T. Pietzsch, S. Preibisch, C. Rueden, S. Saalfeld, B. Schmid, J.-Y. Tinevez, D. J. White, V. Hartenstein, K. Eliceiri, P. Tomancak, & A. Cardona, Fiji: An Open-source Platform for Biological-image Analysis, Nature Methods **9** (2012) 676–682.

[12] D. Hwangbo, S. Kajita, N. Ohno, P. McCarthy, J. W. Bradley, & H. Tanaka, Growth of Nano-tendril Bundles on Tungsten with Impurity-rich He Plasmas, Nuclear Fusion **58** (2018) 096022.

[13] Y. Yamamura, & Y. Mizuno, Low-energy Sputterings with the Monte Carlo Program Acat, IPPJ-AM-40, Institute of Plasma Physics, Nagoya University, 1985.

[14] D. Nishijima, M. J. Baldwin, R. P. Doerner, & J. H. Yu, Sputtering Properties of Tungsten 'Fuzzy' Surfaces, Journal of Nuclear Materials **415** (2011) S96–S99.

[15] G. K. Wehner, Cone Formation as a Result of Whisker Growth on Ion Bombarded Metal Surfaces, Journal of Vacuum Science & Technology A **3** (1985) 1821–1835.

[16] G. Ozaydin, K. F. Ludwig, H. Zhou, & R. L. Headrick, Effects of Mo Seeding on the Formation of Si Nanodots during Low-energy Ion Bombardment, Journal of Vacuum Science & Technology B: Microelectronics and Nanometer Structures Processing, Measurement, and Phenomena **26** (2008) 551–558.

[17] T. J. Novakowski, J. K. Tripathi, & A. Hassanein, Silicon Nanocone Formation via Low-energy Helium Ion Sputtering, Journal of Vacuum Science & Technology B **36** (2018) 051202.
[18] R. M. Bradley, & J. M. E. Harper, Theory of Ripple Topography Induced by Ion Bombardment, Journal of Vacuum Science & Technology A **6** (1988) 2390.
[19] Auciello, Ion Interaction with Solids: Surface Texturing, Some Bulk Effects, and Their Possible Applications, Journal of Vacuum Science and Technology **19** (1981) 841.
[20] L. B. Begrambekov, A. M. Zakharov, & V. G. Telkovsky, Peculiarities and Mechanism of the Cone Growth under Ion Bombardment, Nuclear Instruments and Methods in Physics Research Section B: Beam Interactions with Materials and Atoms **115** (1996) 456–460.
[21] M. A. Makeev, & A. L. Barabási, Ion-induced Effective Surface Diffusion in Ion Sputtering, Applied Physics Letters **71** (1997) 2800–2802.
[22] E. Holmström, A. Kuronen, & K. Nordlund, Threshold Defect Production in Silicon Determined by Density Functional Theory Molecular Dynamics Simulations, Physical review B **78** (2008) 045202.
[23] V. I. Shulga, Angle-dependent Sputter Yield of Rippled Surfaces, Applied Surface Science **458** (2018) 18–23.
[24] S. Kajita, S. Kawaguchi, N. Ohno, & N. Yoshida, Enhanced Growth of Large-scale Nanostructures with Metallic Ion Precipitation in Helium Plasmas, Scientific Reports **8** (2018) 56.
[25] S. Dai, S. Liu, J. Sun, A. Kirschner, G. Kawamura, D. Tskhakaya, R.Ding, G. Luo, & D. Wang, Modelling of Surface Evolution of Rough Surface on Divertor Target in Fusion Devices, Journal of Nuclear Materials **464** (2015) 372–376.
[26] Q. Shi, S. Dai, A. Kirschner, & D. Wang, Numerical and Analytic Study of Rough Surface Morphology on the Angular Distribution of Eroded Impurity, Contributions to Plasma Physics **57** (2017) 329–335.

Chapter 4. Modeling of the impurity-induced silicon nanocone growth by low energy helium plasma irradiation

4.1 Introduction

Silicon with a high density of nanocone morphology, known as black silicon (Si), is one of the promising materials for the solar cell and field emitter [1, 2]. Various technics have been conducted to fabricate nanocones on the Si surface such as reactive ion etching, wet chemical etching, and laser pulses [3–5]. Helium (He) plasma irradiation, which is relatively simple and economical, is another method to form nanostructure on the surface of material. Kajita have observed cone structure, of which He bubbles on the tip, on titanium and stainless steel [6, 7]. As for the Si material, dense nanocone was formed with crystal nature remained at low energy (< 100 eV) of He plasma [8–10]. Recently, the formation of nanocone structure was strongly affected by the deposition of impurity on the Si surface was found [11]. On Si material, impurity-induced nanostructure was broadly reported with argon (Ar) plasma irradiation. Nanorods have formed at various temperatures with the supply of molybdenum (Mo) seed atoms. Ozaydin and Tanemura reported that nanodot structure could not be identified without Mo impurity introduced [12, 13].

However, the mechanism of impurity-induced Si nanocone is still in discussion. Iron and chromium (Cr) impurities are seemed as melted catalytic-sphere to lead the nanocone growth in the 1500 eV of Ar plasma environment [14]. At a lower Ar ion energy (300 eV), Ozaydin concluded that the tensile stress is playing a dominant role in driving the nanodot formation [12]. The shielding effect of impurity was also considered to contribute to the formation of cone structure on both Si [15] and Cr [16] substrates, because impurities were observed on the tip of the cone.

Simulation is a persuasive method to verify the mechanism of nanocone formation. Time development of cone-like shape has been produced with pure Ar ion bombardment [17]. In that model, the cone structure was initially developed from a small protuberance, which represents the asperity on the surface, and finally eroded. However, the nanocone structures in the previous study [11] were steady for long-time irradiation and the original surface was smooth in nanoscale. Moreover, a black dot, which was likely to be the impurity shield, was observed on the tip of cone. Thus, it is meaningful to simulate the cone formation based on the shielding effect.

Several issues related with plasma surface interaction have been investigated with the 3-dimensional Monte Carlo code SURO [18, 19]. In this work, SURO code was upgraded to develop the formation of Si nanocone. Redeposition of Si was found to be another important process during the irradiation.

4.2 Modeling procedure

4.2.1 Impurity distribution

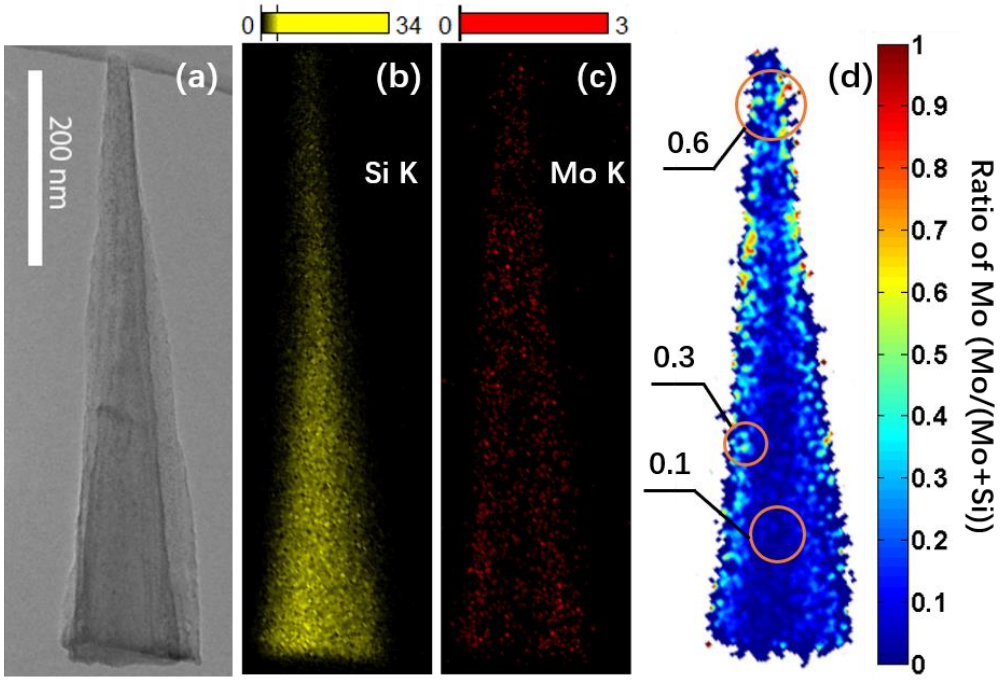

Figure 4.1 (a) TEM of a single nanocone. The EDX mapping of (b) Si and (c) Mo on the nanocone in (a). The distribution of Mo atoms ratio which calculated by Mo atoms / (Mo atoms + Si atoms). Three specific regions of the Mo ratio were marked.

In our previous study [11], Si nanocone was fabricated with He plasma at 57 eV as a result of the Mo seeding from the sample mask. To support the simulation model, electron dispersive X-ray spectroscopy (EDX) mapping was used to examine the distribution of impurities of the cone, as shown in figure 4.1. The observed cone was shown by transmission electron microscopy (TEM) in figure 4.1 (a). Figures 4.1 (b) and (c) show the intensity of Si and Mo respectively for Kα line. The intensity of Si was found higher at the bottom than that of the top region. Moreover, size of Si presenting region, is smaller than Mo. With the datum from figures 4.1 (b) and (c), the atomic concentration of Mo, C_{Mo} was deduced from

$$\frac{C_{Mo}}{C_{Si}} = k_{Mo,Si}\frac{I_{Mo}}{I_{Si}}, \tag{4.1}$$

$$C_{Mo} + C_{Si} = 1, \tag{4.2}$$

where C_{Si} is the atomic concentration of Si, $k_{Mo,Si}$ is a constant that accounts for the relative detection efficiency which is approximately 4 according to [20], I_{Mo} and I_{Si} are the X-ray intensity for Mo and Si, respectively. The distribution of the Mo concentration is shown in figure 4.1 (d). One can see that the average concentration of Mo is high (about 0.3) at the profile of the nanocone. This phenomenon suggests the present of a Mo deposition layer, mixed with Si, corresponding to the profile region of the cone with higher transparency shown in figure 4.1 (a). On the tip, the ratio of Mo in the deposition layer is even

higher (about 0.6) which indicates the surface diffusion or adatoms. This result is in agreement with the hypothesis of the shielding effect. The atomic concentration of Mo on the tip of cone was set as an input factor in the following simulation model.

4.2.2 Simulation model

In SURO code, the size of the simulation region is 0.5 × 0.5 μm^2 separated into 50 × 50 meshes. To perform the impurity effect, Mo impurities are set initially at the center of the entire region occupying 4 meshes as shown in figure 4.2 (b). The fraction of Mo in those meshes were simply set as 0.6, while the rest of the meshes were pure Si. Information on height, species of particles, number of particles, the slope of the local region, etc. are stored in each mesh. The information continues to be updated after a single time loop of 0.01 seconds.

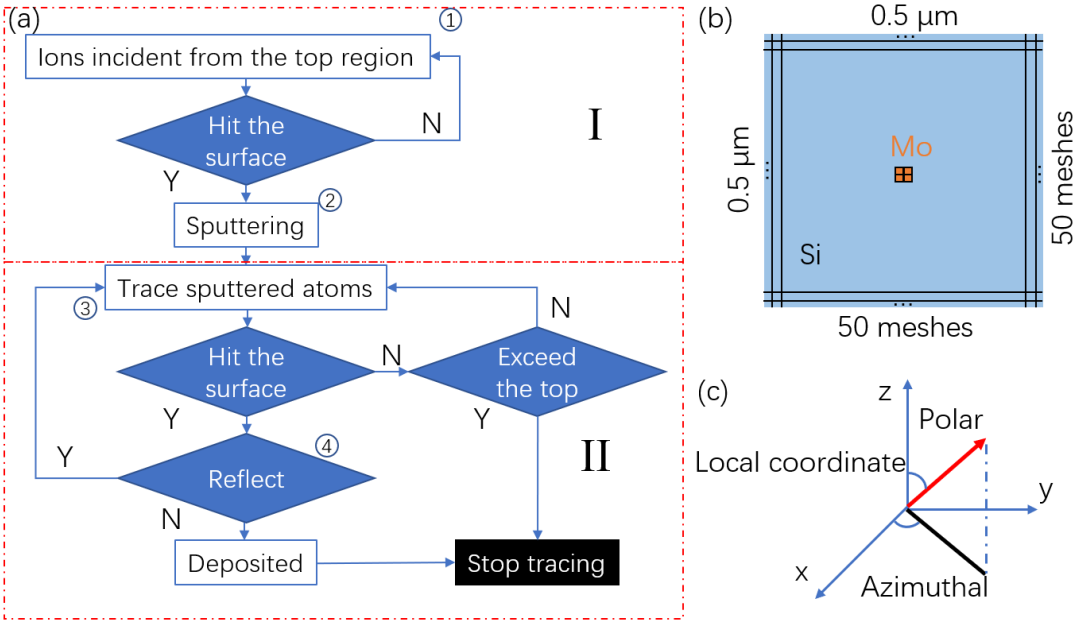

Figure 4.2 (a) A schematic of SURO code, (b) simulation region set up from top view, and (c) the polar angle and azimuthal angle used in the local coordinate.

The code can be mainly separated into two segments, i.e., sputtering and redeposition, as shown in figure 4.2 (a). First, He ions randomly incident from the top in a vertical direction towards the Si surface. Sputtering happens when ions hit the Si surface which belongs to a certain mesh. Then the changes in surface height at that mesh will be calculated based on the sputtering information. The results in section 3.1 were deduced from only the first part.

In the second part, the sputtered Si atoms leave the surface at a certain angle and energy. In the local coordinate, as shown in figure 4.2 (c), the polar angle and the azimuthal angle are assumed as the cosine [21] and uniform distribution, respectively. The energy of sputtered Si follows the Thompson distribution [22]. The simulation code traces the sputtered Si atoms until they re-deposit on the surface or exceed the simulation region.

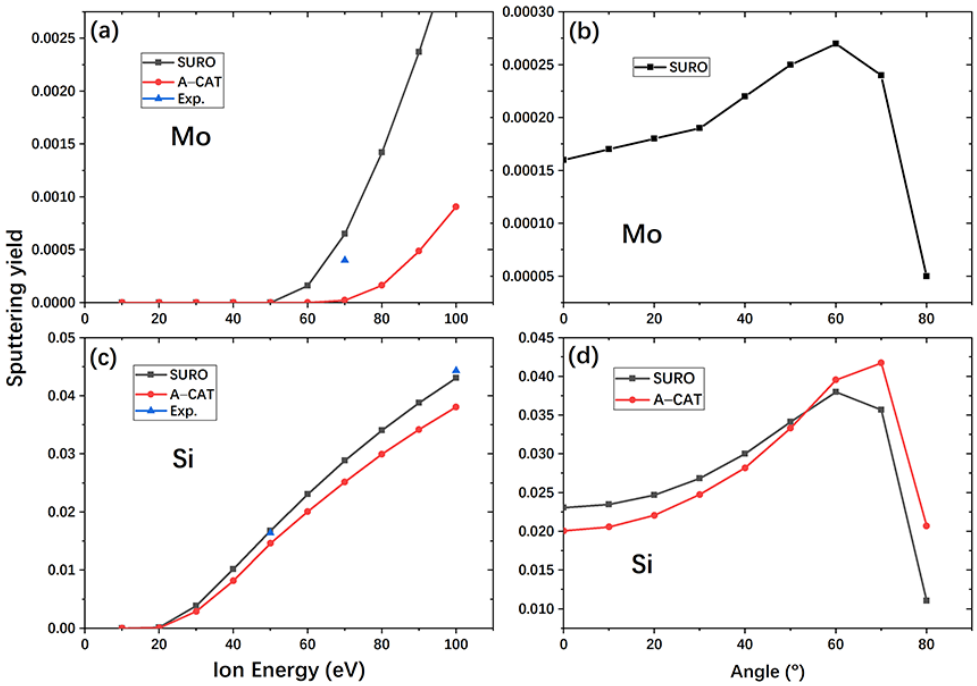

Figure 4.3 Energy (a, c) dependence of sputtering yield for the normal incident and angle (b, d) dependence of sputtering yield at He ion energy of 60 eV on Mo (a, b) and Si (c, d), respectively, from SURO, A-CAT code, and experimental results.

Because sputtering is the most important process, the simulation tests the energy and angular dependence of sputtering yield for both Si and Mo materials and compared with the results from A-CAT [23] code and some experiments [24] as shown in figure 4.3. The sputtering yield is deduced from the following equations:

$$Y(E_0,\alpha) = Y(E_0,\alpha = 0^\circ)(\cos\alpha)^{-f} \exp(f[1-(\cos\alpha)^{-1}]\cos\alpha_{opt}). \quad (4.3)$$

Here, E_0 is the projectile energy, α is the angle of incident ion to the surface normal, f and α_{opt} are used as fitting parameters.

Figures 4.3 (a) and (c) are the energy dependence of sputtering yield at the normal incident direction on Mo and Si, respectively. The sputtering yield calculated in SURO code is slightly higher than the A-CAT code. However, the results are consistent with the experimental data well. It shows that the sputtering yield of Mo is much smaller than Si. Because the He ion energy in our previous experiment was ~60 eV, all the results presented in Section 3 were obtained at the ion energy of 60 eV. Moreover, the angular dependence of sputtering yields has been considered as an important factor that leads to the formation of conical structure in the research [17]; thus, a benchmark was performed with respect to the angular dependence of sputtering yields for Mo and Si as shown in figures 4.3 (b) and (c). In order to approach the experiment result in [11], the angular dependence of sputtering yields for Mo and Si are calculated under 60 eV of He ion energy. The sputtering yield for Mo is zero in the A-CAT calculation at 60 eV. On Si material, the result calculated from SURO has a similar profile with that from A-CAT.

4.3 Results and discussion

4.3.1 Nanocone formation

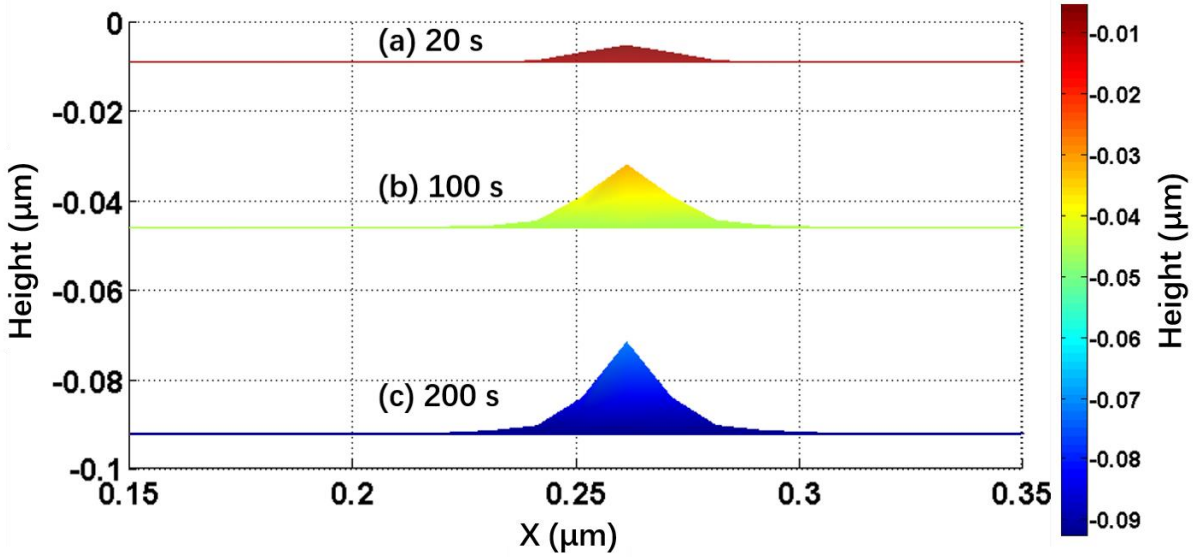

Figure 4.4 Cone structure evolution at (a) t = 20 s, (b) t = 100 s, (c) t = 200 s, from the side view.

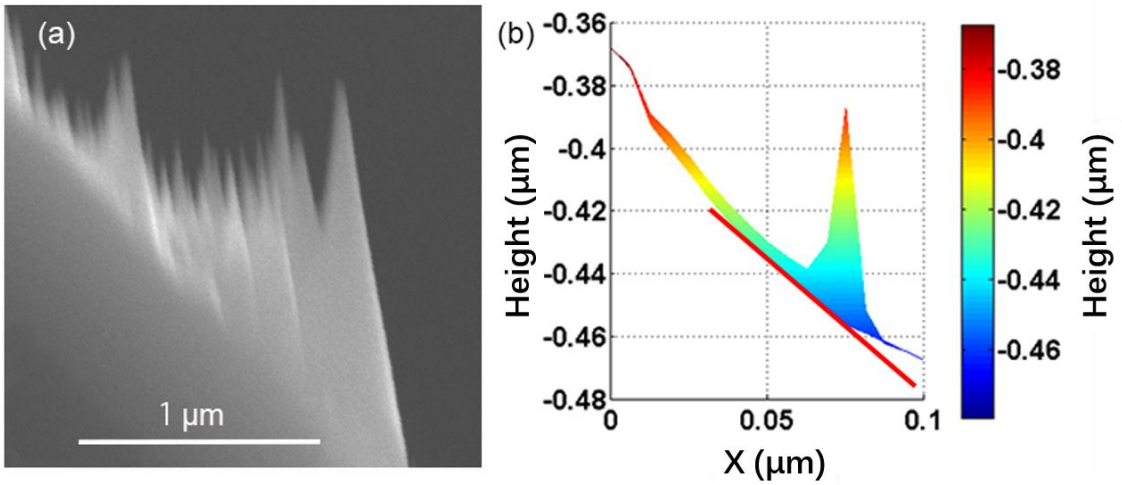

Figure 4.5 (a) Rotated image of nanocone formed on the surface with oblique incident He ion in the experiment. (b) Nanocone formed on the tilted surface by simulation. The direction of incident ions in (a) and (b) are set the same for convenient comparison.

Figure 4.4 shows the formation process of Mo-induced Si nanocone. Cone structures at 20, 100, and 200 seconds are shown in figures 4.4 (a), (b), and (c), respectively. The original height of the surface was 0 μm. Because the sputtering yield of Mo is smaller than Si, a small protuberance formed from the flat surface where Mo impurities located. As the erosion goes deeper, the cone shape forms and the height gradually becomes larger. The angular dependence of sputtering yield was thought to be an important

factor for the formation of nanocone [17]. Besides, the incident angle for a maximum sputtering yield was considered to significantly influence the cone shape [25, 26]. However, a similar result was not shown in this research. The height of the cone will keep increasing as the irradiation time pass, while the diameter, i.e., the width of the bottom of the cone, was not clearly extended and only consistent with the Mo covered region. It is probably because protuberance without the coverage of Mo is sputtered immediately, due to the higher sputtering yield at a tilted incident angle. Hence, the shielding effect of Mo is considered as a primary reason for the nanocone formation. The diameter of the cone will be discussed again in section 4.3.2 with redeposition effect.

The direction of Si nanocone pointed was found to be followed the incident ion in our previous study [11]. As shown in figure 4.5 (a), the cone structures are inclined to the surface. Generally, the direction of the incident ion is perpendicular to the target surface because of the sheath layer. However, the configuration of the sheath was changed close to the sample mask which was made of Mo. With the influence of the mask, the direction of the electric field was inclined away from the mask. In figure 4.5 (a) rotation of the image makes the direction of incident ion perpendicular to the horizontal for a convenient comparison with the simulation result in figure 4.5 (b).

In this study, the angle between the incident He ions and the surface was parameterized. Because only unique value of height is allowed for one (x, y) coordinate in model, the surface was tilted while keeping the incident ions parallel to the z axis instead of inclining the incident direction. As shown in figure 4.5 (b), the 'growth' of the cone structure follows the incident ion other than perpendicular to the surface marked with red line. This result suggested that the direction of the cone is strongly affected by the angle of the incident ion.

4.3.2 Redeposition effect of sputtered Si atoms

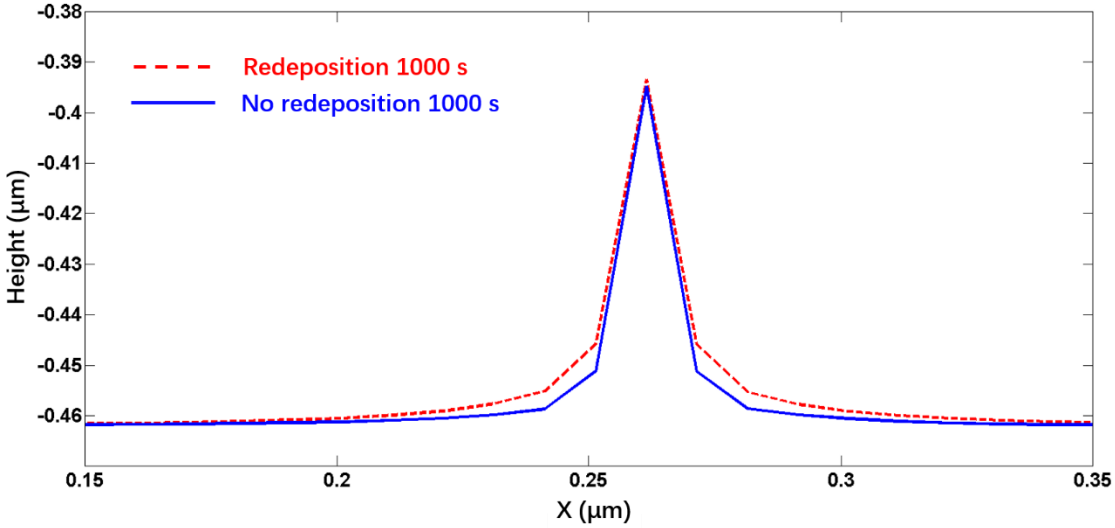

Figure 4.6 Cross-section of the nanocone with (red dash line) and without (blue solid line) redeposition effect after 1000 s.

Figure 4.6 shows the cross-section of the nanocone with and without redeposition effect after He ions irradiation for 1000 s. At the base of the surface and the tip of the cone, the height of the redeposition

(the second part introduced in section 2.2) case is almost the same as the case without the redeposition effect. At the bottom of the cone, however, the height of the former is much higher than that of the latter. Thus, the redeposition is more likely to occur at the bottom of the cone other than uniformly on the whole surface. This is because sputtered Si atom left the surface at a certain angle which avoid it to redeposit at the same position where it had been sputtered. However, it possibly hit the cone which protruded from the surface. Assumed that if the hit energy is smaller than the surface binding energy, deposition occurs at the impinging place. Consequently, the height of the surface at the hit point is increased according to the number of deposited atoms. Considering the structure of the cone, the upper region was too small for the sputtered atoms to reach, while the bottom can receive the atoms from the ground region of the surface. This phenomenon can be considered as one of the processes to increase the cone diameter. Moreover, the heavier redeposition of Si at the bottom region diluted the concentration of Mo which explains the lower Mo ratio at the bottom of the deposition layer observed in the EDX mapping in figure 4.1.

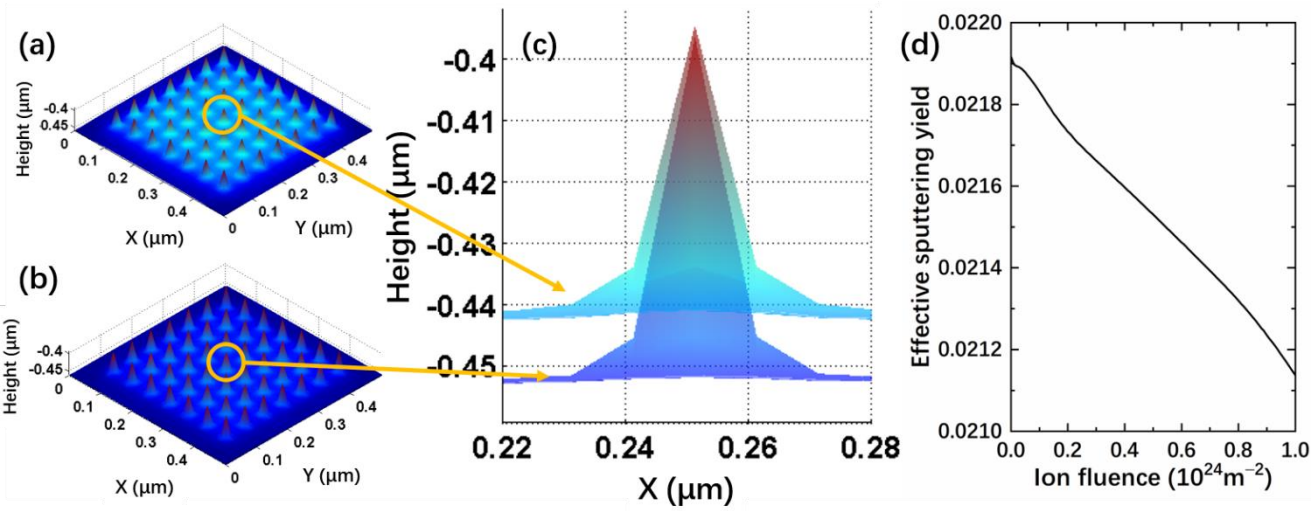

Figure 4.7 Surface morphology with 49 nanocones structures with (a) and without (b) redeposition effect after 1000 s. (c) Comparison in the cross-section view of the nanocone at the center of (a) and (b). (d) Effective sputtering yield with redeposition effect as a function of ion fluence.

In the former study, the effective sputtering yield for black Si was found to be significantly decreased compared with that on the flat surface [11]. Here, a nanocones array with 49 cones was calculated to approach the black Si case. Morphologies of Si surface developed with and without the redeposition effect are shown in figures 4.7 (a) and (b), respectively. By comparing the erosion depth of (a) and (b) at the center of the sample as shown in figure 4.7 (c), one can recognize that the redeposition effect becomes heavier than the single cone case in figure 4.6. This can be explained by the enhanced redeposition from the surrounding cone. Moreover, the redeposition effect is one of the important process leading to the reduction of the effective sputtering yield which was observed in [11]. Without the redeposition process, the sputtering yield is roughly 2.3×10^{-2} which is almost the same as the value (2.31×10^{-2}) calculated on the flat Si surface in figure 4.3 (c).

However, this reduction in sputtering yield is still far from the real condition in which the effective sputtering yield of black Si was 80% less than that on a pristine surface. This is probably because the surface in this simulation model almost consists of pure Si other than the tip of cones. While in the actual

irradiation, even if not as much as tips, the Si substrate is also mixed with Mo. The effective sputtering yield of Cr cone surface exposed to a He plasma at an incident ion energy of 80 eV has been measured during the irradiation [16]. The decrease of effective sputtering yield can be separated into two phases: (1) a rapid decrease by 50% up to an ion fluence of 5×10^{24} m^{-2} at the beginning; (2) a linear mild decrease of 1.3% per the ion fluence of 1×10^{24} m^{-2}. Considering the measurement of the atomic concentration of the Si nanocone surface performed by Qiu et al. [14], the deposition of impurities on the sample was saturated in a very low ion fluence. Thus, we believe that the first phase of the sputtering yield reduction is because of the impurity accumulation on the surface. Considering the second phase, from the changes of the sputtering yield with the increasing of ion fluence shown in figure 4.7 (d). The reduction rate was 3.6% pzer 1×10^{24} m^{-2} of the fluence which is on the same order of magnitude as the result in [16]. This result suggests that the formation of dense nanocone will reduce the effective sputtering yield due to the enhanced line-of-sight redeposition.

4.4 Summary

The distribution of Mo on the Si nanocone formed by He plasma irradiation was measured. A high-density Mo zone, which is considered as a shield for the seed of nanocone formation, with a Mo fraction of 0.6 was observed on the tip of cone. Based on the shield effect model, the development of cone structure with time initiated from a flat Si surface can be reproduced by SURO code. The direction of the cone structure follows the incident ion in a tilted substrate case, which is consistent with the experimental result. Sputtered Si atoms are redeposited and contribute another important process in the formation of nanocone. The redeposition effect will enlarge the diameter of the cone. The reason for the gentle decrease of the sputtering yield during the long period of irradiation was revealed.

References

[1] M. Kanechika, N. Sugimoto, & Y. Mitsushima, Control of Shape of Silicon Needles Fabricated by Highly Selective Anisotropic Dry Etching, Journal of Vacuum Science & Technology B: Microelectronics and Nanometer Structures **20** (2002) 1298–1302.

[2] X. Ao, X. Tong, D. Sik Kim, L. Zhang, M. Knez, F. Müller, S. He, & V. Schmidt, Black Silicon with Controllable Macropore Array for Enhanced Photoelectrochemical Performance, Applied Physics Letters **101** (2012) 111901.

[3] M. Steglish, T. Kasebier, M. Zilk, T. Pertsch, E.-B. Kley, & A. Tunnermann, The Structural and Optical Properties of Black Silicon by Inductively Coupled Plasma Reactive Ion Etching, Journal of Applied Physics **116** (2014) 173503.

[4] Y. Xia, B. Liu, J. Liu, Z. Shen, & C. Li, A Novel Method to Produce Black Silicon for Solar Cells, Solar Energy **85** (2011) 1574–1578.

[5] T. H. Her, R. J. Finlay, C. Wu, S. Deliwala, & E. Mazur, Microstructuring of Silicon with Femtosecond Laser Pulses, Applied Physics Letters **73** (1998) 1673–1675.

[6] S. Kajita, T. Yoshida, D. Kitaoka, R. Etoh, M. Yajima, N. Ohno, H. Yoshida, N. Yoshida, & Y. Terao, Helium Plasma Implantation on Metals: Nanostructure Formation and Visible-light Photocatalytic Response, Journal of Applied Physics **113** (2013) 134301.

[7] S. Kajita, D. Kitaoka, N. Ohno, R. Yoshihara, & N. Yoshida, Surface Modification of Titanium Using He Plasma, Applied Surface Science **303** (2014) 438–445.

[8] S. Takamura, Y. Kikuchi, K. Yamada, S. Maenaka, K. Fujita, & Y. Uesugi, Nanostructure Formation on Silicon Surfaces by Using Low Energy Helium Plasma Exposure, Japanese Journal of Applied Physics **55** (2016) 120301.

[9] S. Takamura, T. Aota, H. Iwata, S. Maenaka, K. Fujita, Y. Kikuchi, & Y. Uesugi, Black Silicon with Nanostructured Surface Formed by Low Energy Helium Plasma Irradiation, Applied Surface Science **487** (2019) 755–765.

[10] M. Thompson, Q. Shi, S. Kajita, N. Ohno, & C. Corr, Effect of Temperature and Incident Ion Energy on Nanostructure Formation on Silicon Exposed to Helium Plasma, Plasma Process Polym **17** (2020) e2000126.

[11] Q. Shi, S. Kajita, N. Ohno, M. Tokitani, D. Nagata, & S. Y. Feng, The Influence of Impurities on the Formation of Nanocone Structures on Silicon Surface Irradiated by Low Energy Helium Plasma, Journal of Applied Physics **128** (2020) 023301.

[12] G. Ozaydin, K. F. Ludwig, H. Zhou, & R. L. Headrick, Effects of Mo Seeding on the Formation of Si Nanodots during Low-energy Ion Bombardment, Journal of Vacuum Science & Technology B: Microelectronics and Nanometer Structures Processing, Measurement, and Phenomena **26** (2008) 551–558.

[13] M. Tanemura, H. Yamauchi, Y. Yamane, T. Okita, & S. Tanemura, Controlled Fabrication of Mo-seeded Si Microcones by Ar^+-ion Bombardment, Nuclear Instruments and Methods in Physics Research Section B: Beam Interactions with Materials and Atoms **215** (2004) 137–142.

[14] Y. Qiu, H. C. Hao, J. Zhou, & M. Liu, A Close to Unity and All-solar-spectrum Absorption by Ion-sputtering Induced Si Nanocone Arrays, Optics Express **20** (2012) 22087–22094.

[15] X. L. Ma, N. G. Shang, Q. Li, C. S. Lee, I. Bello, & S. T. Lee, Microstructural Characterization of Si Cones Fabricated by Ar+-sputtering Si/Mo Targets, Journal of Crystal Growth **234** (2002) 654–659.

[16] D. Nishijima, A. Kreter, M. J. Baldwin, D. Borodin, A. Eksaeva, D. Hwangbo, S. Kajita, M. Miyamoto, N. Ohno, M. Patino, A. Pospieszczyk, M. Rasinski, T. Schlummer, A. Terra, & R. P.

Doerner, Influence of Heavier Impurity Deposition on Surface Morphology Development and Sputtering Behavior Explored in Multiple Linear Plasma Devices, Nuclear Materials and Energy **18** (2019) 67–71.

[17] R. S. Robinson, & S. M. Rossnagel, Ion-beam-induced Topography and Surface Diffusion, Journal of Vacuum Science & Technology **21** (1982) 790.

[18] S. Dai, S. Liu, J. Sun, A. Kirschner, G. Kawamura, D. Tskhakaya, R.Ding, G. Luo, & D. Wang, Modelling of Surface Evolution of Rough Surface on Divertor Target in Fusion Devices, Journal of Nuclear Materials **464** (2015) 372–376.

[19] Q. Shi, S. Dai, A. Kirschner, & D. Wang, Numerical and Analytic Study of Rough Surface Morphology on the Angular Distribution of Eroded Impurity, Contributions to Plasma Physics **57** (2017) 329–335.

[20] J. I. Goldstein, D. B. Williams, & G. Cliff, Quantitative X-ray Analysis, In: D. C. Joy, A. D. Romig, J. I. Goldstein, (Eds.) Principles of Analytical Electron Microscopy, Springer: Boston, MA, 1986, 155–217.

[21] H. Gnaser, Energy and Angular Distributions of Sputtered Species Sputtering by Particle Bombardment, In: Sputtering by Particle Bombardment, Topics in Applied Physics **110**, Springer: Berlin, Heidelberg, 2007, 231–328.

[22] W. Eckstein, & V. Philipps, Physical Sputtering and Radiation Enhanced Sublimation, Rep. KFA-IPP 02/96, KFA-IPP, Julich, 1996.

[23] Y. Yamamura, & Y. Mizuno, Low-energy Sputterings with the Monte Carlo Program Acat, IPPJ-AM-40, Institute of Plasma Physics, Nagoya University, 1985.

[24] W. Eckstein, C. Garcla-Rosales, J. Roth, & W. Ottenberger, Sputtering Data, Report IPP 9/82, Max-Planck-Institut f'tir Plasmaphysik: Garching, Germany, 1993.

[25] G. K. Wehner, Cone Formation as a Result of Whisker Growth on Ion Bombarded Metal Surfaces, Journal of Vacuum Science & Technology A **3** (1985) 1821–1835.

[26] L. B. Begrambekov, A. M. Zakharov, & V. G. Telkovsky, Peculiarities and Mechanism of the Cone Growth under Ion Bombardment, Nuclear Instruments and Methods in Physics Research Section B: Beam Interactions with Materials and Atoms **115** (1996) 456–460.

Chapter 5. The dependence of Mo ratio on the formation of uniform black silicon by helium plasma irradiation

5.1 Introduction

Silicon (Si) is playing an important role in terms of solar cells and many other photonic applications [1, 2]. To minimize the reflection losses from the surface, Si with dense nanocone morphology (known as black Si) have been fabricated with various methods. Moreover, the nanocone structure allows Si to be the potential material of field emitter [3, 4]. Si nanocone is also of interest in the thermophotovoltaic system as a selective emitter [5]. A conventional method to fabricate nanostructures on Si is reactive ion etching (RIE) [5–9]. Steglich et al. produced black Si with SF_6 and O_2 mixture gas by RIE. After 5 min etching, the reflectance was nearly completely suppressed by the formation of nanocone structures [10]. However, RIE may cause surface damage due to the high power of the radio frequency source. Wet chemical etching can avoid the damage from ions; however, the usage of ultrathin Si wafer or film (smaller than 200 μm) limits application for an industrial concern [11, 12]. Conical structure has been also obtained by the laser pulse and ion beam. Such kind of technic usually gives rise to a nonuniform surface because of the Gaussian spatial profile of the laser or ion beam [13, 14].

Recently, to fabricate black silicon, plasma irradiation has been employed with some distinct advantages such as simple process, economical, and soft for the Si substrate [15, 16]. Nonetheless, the morphology and the uniformity of the Si surface are still difficult to control [17–19]. Because the reflectance depends on many features of the surface morphology, such as density, size, and height of the nanostructure, it is desired to tailor the morphology with uniformity in a larger area by plasma irradiation. In our previous work, impurity seed, deposited on the silicon surface, was considered as a key factor for the nanocone formation [20]. Co-deposition experiment is an effective method to introduce additional species simultaneously with the plasma irradiation [21]. In the present study, uniform black silicon with nanocone structures was formed after irradiating Si samples in helium (He) plasma with auxiliary molybdenum (Mo) co-deposition. A relationship was found between the aspect-ratio of the nanocone and the quantified Mo ratio. The role of Mo was discussed through the transmission electron microscope (TEM) and the energy dispersive X-ray spectroscopy (EDX) observation and a comparison experiment between discontinue and full-time Mo co-deposition. Finally, from the optical reflectance measurement, it is shown that the Si surface exhibits good suppression of reflectance in visible light with a large diameter and height of nanocones.

5.2 Preparation

5.2.1 Experimental setup

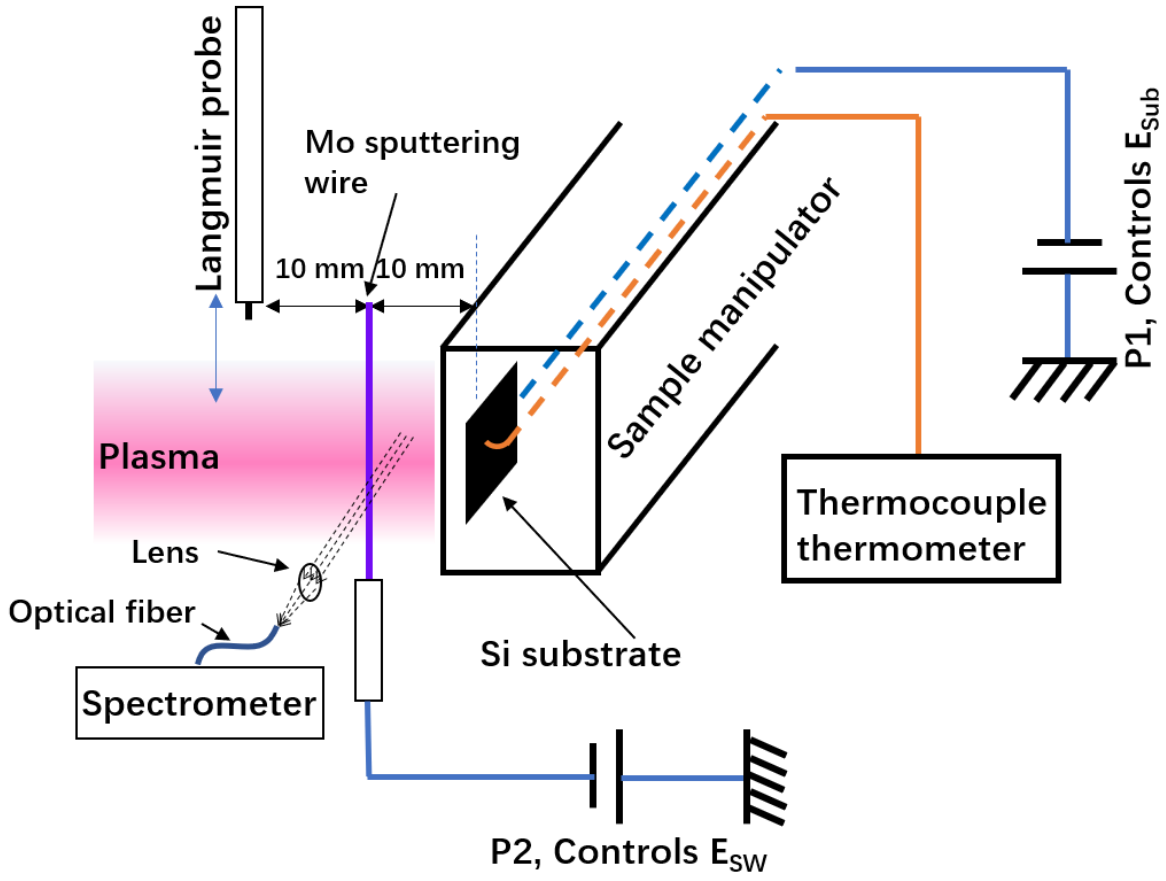

Figure 5.1 Schematic of the experimental setup from the side view. The emission light from the plasma is monitored by a spectrometer. Ion energies on the Si substrate, E_{Sub}, and the Mo sputtering wire, E_{SW}, are controlled by power supplies P1, and P2, respectively.

Experiments were conducted by a linear plasma device Compact-Nagoya University divertor simulator (Co-NAGDIS) [20, 22]. The electron density and temperature were ~1×10^{18} m^{-3} and 6 eV, respectively. The Si (100) wafers (N-type, one side polished) with the thickness of 0.5 mm were cut into 10 mm × 10 mm squares and set in the middle of the He plasma. For all the cases in this study, samples were preheated up to 500 °C by electron heating and the sample temperature was maintained during the plasma irradiation up to an ion fluence of 2.5×10^{25} m^{-2} in total. Because a metal sample holder was biased together with the Si sample, He ion flux was measured via the electron saturation current on a cylindrical Langmuir probe. Planer sheath will be formed on the probe according to [23], we used the projection area of the probe for the calculation. This kind of measurement has been verified by Thomson scattering in [24]. He ion energy was estimated from the bias on the Si substrate or the Mo sputtering wire after taking the plasma potential of ~3 V into account. A schematic of the experimental setup in figure 5.1 shows the relative position of Mo wire with respect to the Si sample, Mo wire, and the plasma column in Co-NAGDIS. The ratio of sputtered Mo and the energy of incident He ions on the Si surface can be modified by changing the bias on the Mo wire and the Si sample, respectively. The light from plasma at

the region between the Mo wire and Si sample was monitored by a spectrometer through the window. Oxide layer on the Si surface can be sputtered rapidly according to the previous experiment [20]. After the irradiation, samples were restored in a vacuum container to avoid contamination or oxidization.

5.2.2 Quantification of Mo flux

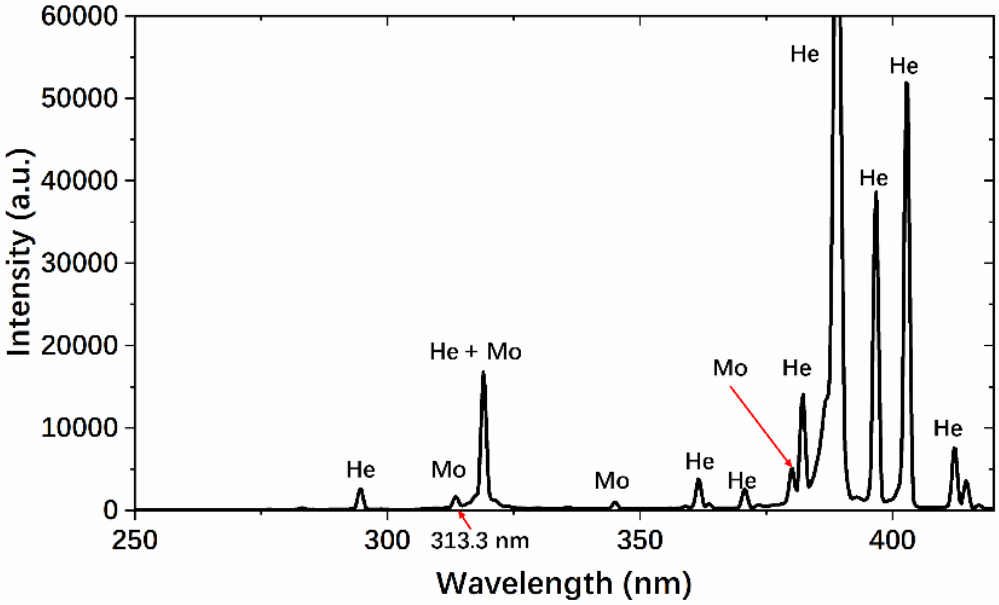

Figure 5.2 The spectrum of He plasma with Mo wire sputtering.

The relative intensity of Mo emission light was recorded for each co-deposition experiment. To quantify the amount of Mo flux for each experiment, a reference case with acquirable Mo deposition flux was required. Thus, we deposited Mo on the glass for a certain time, t, as the reference case. The Mo flux for the reference case, Γ_{ref}, was obtained from the thickness of the deposition layer, measured by a surface profilometer, over *t*. The flux can be expressed as

$$\Gamma_{ref} \propto v_{Mo} \times n_{Mo} . \tag{5.1}$$

Here, v_{Mo} is the average velocity of Mo atoms sputtered from the wire and n_{Mo} is the atomic density of Mo. On the other hand, the corresponding spectrum, as shown in figure 5.2, was recorded by a spectrometer. The intensity of Mo light emission, *I*, which is used in the following calculation was deduced by the Voigt profile-fitting at the wavelength of 313.3 nm. The light intensity is proportional to the density of the Mo atoms, n_{Mo}, i.e.,

$$I \propto n_{Mo} \times n_e \times PEC(T_e, n_e) , \tag{5.2}$$

where n_e is the electron density and PEC (T_e, n_e) is the photon emissivity coefficient which depends on both electron density and temperature, T_e. PEC (T_e, n_e) was calculated based on the database in the atomic data analysis structure (ADAS) data base [25]. Here we neglected the excitation due to He metastable states because of the lack of data. Because the density of He metastable is much lower than that in recombining plasmas, where the metastable state density was ~1% of the electron density [26], in the linear plasma device NAGDIS-II, which is similar to Co-NAGDIS device, the above assumption is likely

valid. Thus, the relationship between the intensity of excited Mo for each case, I_{Mo}, and the reference case, I_{ref} can be depicted as follows:

$$\frac{I_{Mo}}{I_{ref}} = \frac{n_{Mo,i} \times n_{e,i}}{n_{Mo,ref} \times n_{e,ref}}. \tag{5.3}$$

Because v_{Mo} is primarily determined by the surface binding energy of the sputtered material, which is constant for Mo, according to Thompson's theory [27], the flux of Mo for each case, Γ_{Mo}, is obtained from (1) and (3) as

$$\Gamma_{Mo} = \Gamma_{ref} \frac{I_{Mo} \times n_{e,ref}}{I_{ref} \times n_{e,i}}. \tag{5.4}$$

The ratio of Mo flux, $\Gamma_{Mo} / \Gamma_{He}$, can be calculated by Mo flux, Γ_{Mo}, over He flux, Γ_{He}, which was obtained from a Langmuir probe. Note that biases on the Mo wire were basically larger than -50 V which is not low enough for He to knock Mo atoms out. Oxygen, which is the primary impurity gas that exists in the vessel, was assumed as the particle that prompts the Mo sputtering [28]. Thus, we did not calculate the Mo ratio simply from the sputtering yield.

5.3 Deposition experiments

5.3.1 Uniform formation of nanocone

Samples with and without the Mo co-deposition are shown in figure 5.3 to compare the uniformity. The surface of the case without Mo co-deposition shows roughly two regions of brown (I) and dark (II) as shown in figure 5.3 (d). Nanostructures corresponding to those two regions are shown in figures 5.3 (a) and (b), respectively. It can be seen that nanocones in the dark region are denser and about 75 nm in diameter which is approximately then times smaller than those in the brown region. The incident He ion energy loaded on the Si substrate, E_{sub}, was 60 eV. The non-uniform morphology probably caused by impurities which were sputtered from the sample holder and biased deposited on the Si surface [20]. When a biased Mo wire was introduced during the plasma irradiation, the surface became complete black and uniform as shown in figure 5.3 (e). The SEM image of figure 5.3 (e) is corresponding to figure 5.3 (c). Here E_{sub} was 40 eV to minimize the influence of sputtered species from the sample holder and the parameter dependences are shown next.

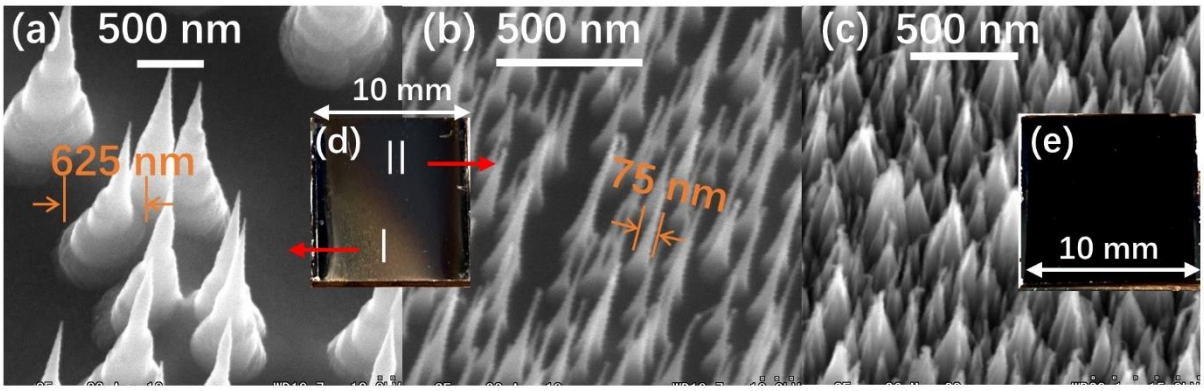

Figure 5.3 (a, b) SEM images of (d) a nonuniform Si surface at different regions which pointed by red arrows. The ion fluence is 2.5×10^{25} m^{-2} and the energy, E_{sub}, is 60 eV. (c) SEM image of (e) a uniform

black Si surface with Mo deposition. The ion fluence is 2.5×10^{25} m^{-2} and E_{sub} is 40 eV. Ion energy loaded on the Mo sputtering wire, E_{SW}, is 40 eV.

5.3.2 Parameter dependence

Figure 5.4 shows a series of sample morphology from the SEM in tilted view of 30°. Both of the ion energy loaded on the Mo sputtering wire, E_{SW}, and the Si sample, E_{sub}, was in the range of 30 to 50 eV. In all the cases, the morphology change occurs uniformly. The nanostructure is affected by both Mo flux and ion energy. Comparing cases between figures 5.4 (a–c) and (d–f), it seems that higher ion energy leads to larger nanocones formation. This dependence, however, is not sustained when comparing figures 5.4 (e, f) and (h, i). When E_{sub} = 40 eV (figures 5.4 (d–f)), the aspect ratio, which represents the height divided by the diameter, of the nanocone decreases as increasing E_{SW}. Moreover, fiber form structures can be found on the tip of the cone in some cases (figures 5.4 (e–i)). Those fiber form structures are probably consisting of Mo by surface diffusion which will be further discussed in section 5.4.3.

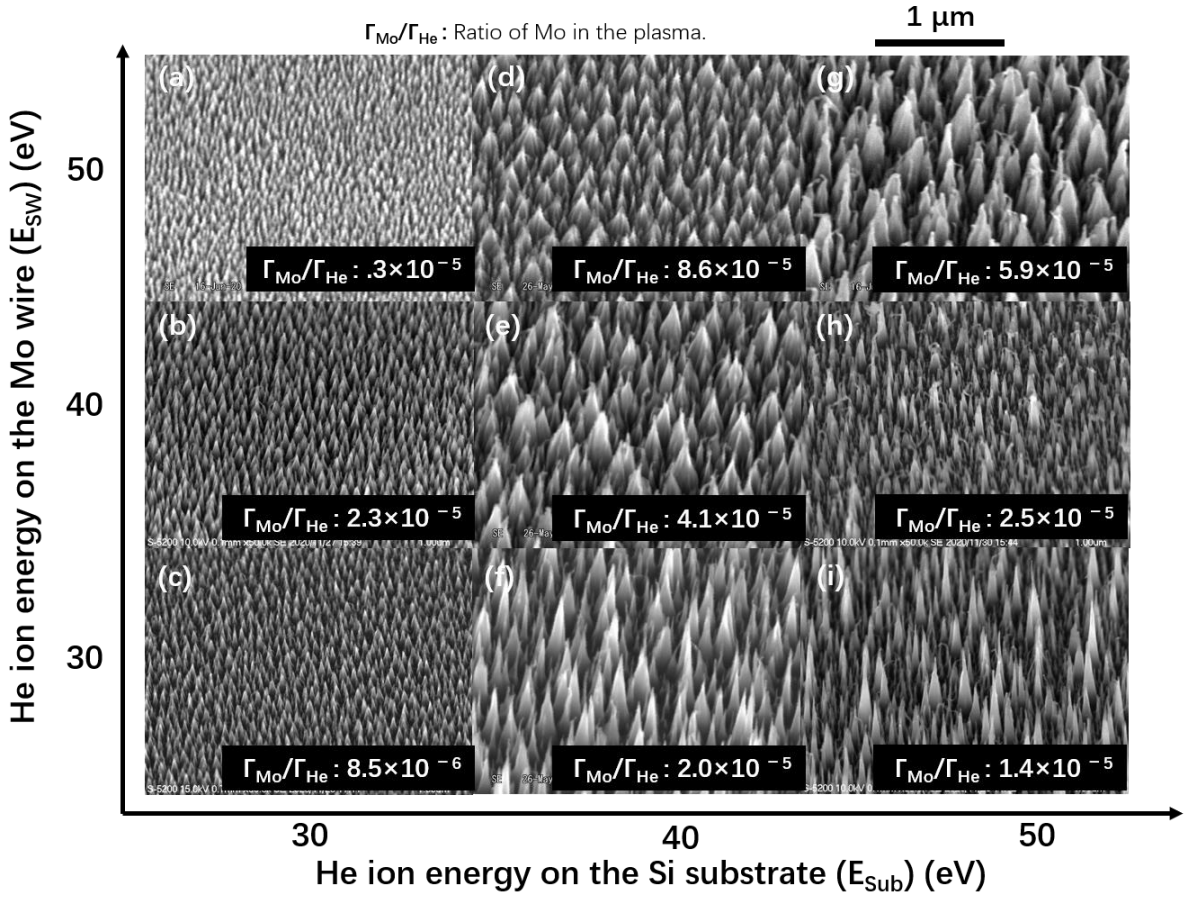

Figure 5.4 Morphologies of black Si at a tilted view of 30° for different E_{sub} and E_{SW}. The Mo flux ratios in different conditions were written on the corresponding images.

5.3.3 Characteristics of nanocone

To quantitatively investigate the influence of Mo flux and ion energy on the characteristic of nanocone, the average height and the aspect ratio of nanocones was measured from the SEM images in a cross-section view. In figure 5.5, heights and aspect ratios of nanocone under different incident ion energies are shown as a function of $\Gamma_{Mo} / \Gamma_{He}$ which is calculated by equation (4). From figure 5.5 (a), one can see that the height of the nanocone is smaller than 300 nm when E_{sub} = 30 eV. That is because the nanocone is formed by sputtering and the sputtering yield at 30 eV ($\sim 3\times10^{-3}$ between He and Si) is too low to generate a high cone structure. Nanocones become lower when the $\Gamma_{Mo} / \Gamma_{He}$ increases. Because heavier deposition of Mo suppresses the sputtering process. When the E_{sub} is 40 and 50 eV, the highest cone for each group does not appear at the lowest $\Gamma_{Mo} / \Gamma_{He}$. This is probably because the "growth" of the nanocone requires protection of the sufficient Mo deposition from the ion bombardment. Some other evidence that supports this point of view will be shown in section 5.4.

Although the height of the cone is not simply affected by $\Gamma_{Mo} / \Gamma_{He}$, the aspect ratio of the nanocone exhibits a clear relation with $\Gamma_{Mo} / \Gamma_{He}$ as shown in figure 5.5 (b). The aspect ratio shows a linear dependence on the logarithm of $\Gamma_{Mo} / \Gamma_{He}$. Those three lines are almost of the same slope for different E_{sub}. Higher ion energy tends to form nanocones with a larger aspect ratio at the same level of $\Gamma_{Mo} / \Gamma_{He}$. Although the height of nanocones changed in a wide range, as shown in figure 5.5 (a), the relationship between the aspect ratio and $\Gamma_{Mo} / \Gamma_{He}$ was not influenced. This relation raises a potential method to tailor the nanostructure on silicon by adjusting the ratio of impurity.

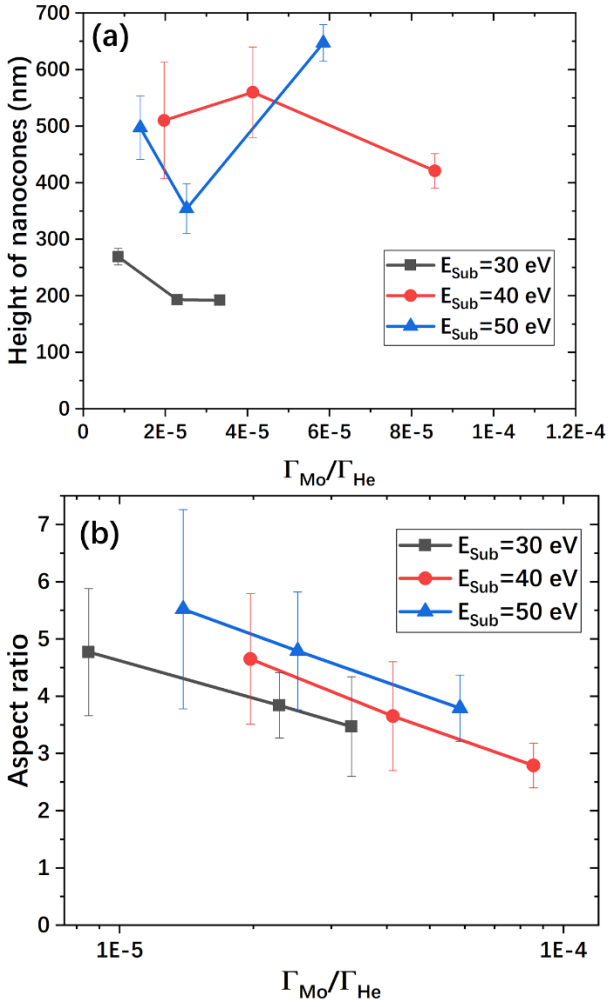

Figure 5.5 (a) Height and (b) aspect ratio of nanocones at different E_{sub} (30, 40, and 50 eV) for Si sample as a function of Γ_{Mo} / Γ_{He}. The error bar here means the standard deviation of the height and the aspect ratio of nanocone in (a) and (b), respectively.

5.4 Function of deposition

5.4.1 EDX and TEM analyses

In order to understand how the deposition of Mo affects the formation of nanocones, the distribution of Mo was investigated through the EDX mapping for two additional cases with E_{SW} at 50 eV (case A) and 70 eV (case B). He ion fluence for the Si sample, E_{sub}, and the sample temperature is 2.5×10^{25} m^{-2}, 40 eV, and 500 °C, respectively, for both of the two cases. SEM micrographs of cases A and B from the SEM are shown in figures 5.6 (a) and (b), respectively. Although the Mo flux has not been quantified as it had been treated in section 3, it is acceptable to assume that the ratio of Mo flux, Γ_{Mo} / Γ_{He}, for case A is lower than B, since He governs the sputtering of Mo at the ion energy of 70 eV. One can see from the SEM images in Figure 5.6 that the aspect ratio decreases with the increase of Γ_{Mo} / Γ_{He}.

Figures 5.6 (c) and (d) are EDX mapping of the nanocones scraped from the samples shown in figures 5.6 (a) and (b), respectively. It shows that the intensity of Si on the tip is smaller than that at the bottom. The tip of the cone consists of mostly Mo. In order to quantitatively compare the Mo distribution

of cases A and B, the height dependences of the Mo fraction, F_{Mo}, in figures 5.6 (c) and (d) are shown in figures 5.6 (e) and (f), respectively.

$$F_{\mathrm{Mo}} = \frac{N_{\mathrm{Mo}}}{N_{\mathrm{Si}} + N_{\mathrm{Mo}}}, \tag{5.5}$$

where, N_{Mo} and N_{Si} is defined by the number density of Mo atoms and Si atoms, respectively. It can be seen that F_{Mo} in the upper region for case B is higher than A. This large fraction of Mo is probably provided by the large Γ_{Mo} / Γ_{He} during the plasma irradiation. On the other hand, the larger Γ_{Mo} / Γ_{He} provides a larger area of protection on nanocone. As shown in Figures 5.6 (e) and (f), assuming that F_{Mo} ≥ 0.4 is effective for Mo protects Si from sputtering, the coverage depth for E_{SW} = 50 eV (~50 nm) is smaller than that of E_{SW} = 70 eV (~120 nm).

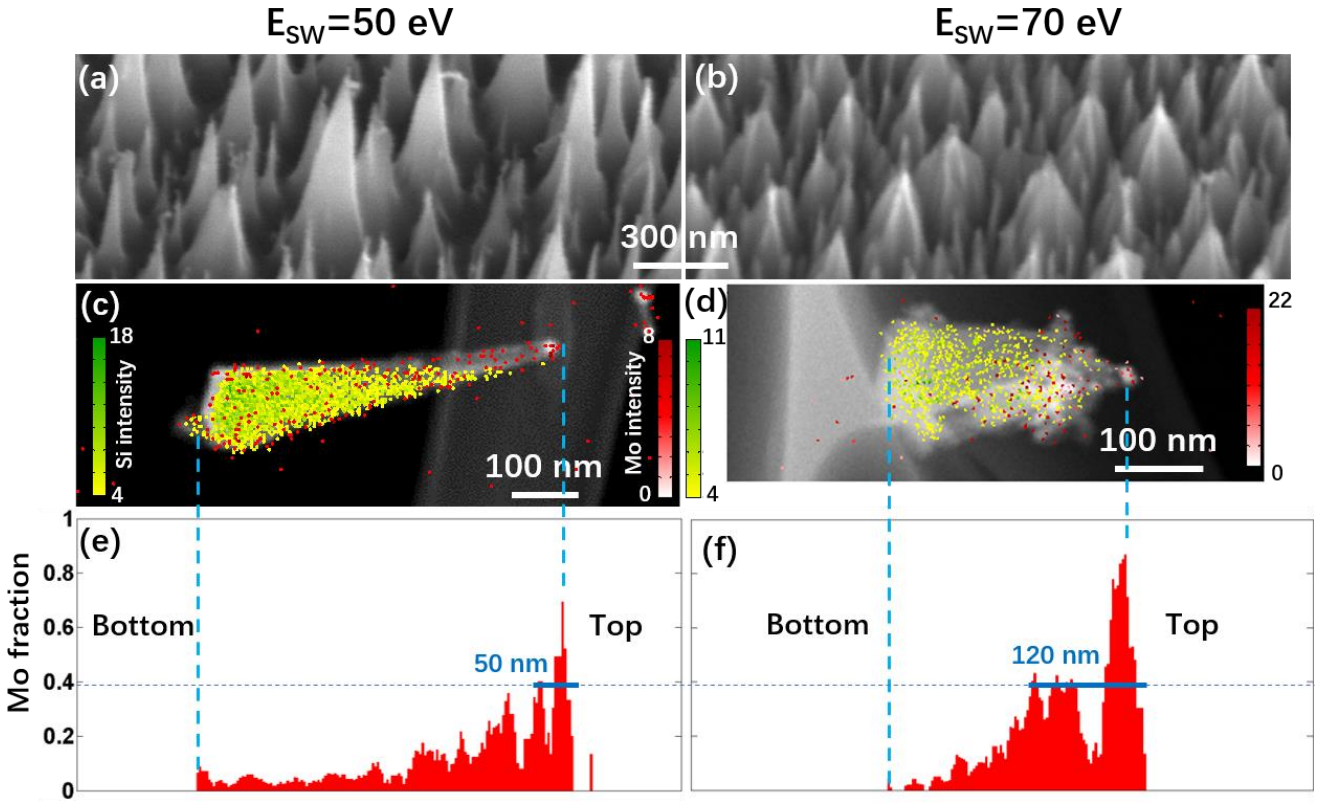

Figure 5.6 (a, b) SEM images of cases with E_{SW} = 50 eV and 70 eV, respectively. (c, d) EDX mappings of the nanocone in (a) and (b), respectively. (e, f) the height dependences of the Mo fraction of the nanocone in (c) and (d), respectively.

Figure 5.7 shows a TEM image of the nanocone in figure 5.6 (c) in a larger magnification. Various sizes of dark dots can be seen on the cone. The upper region of the cone was magnified in figure 5.7 (b). A black dot on the tip of the cone represents a high fraction of Mo, as was observed in the EDX mapping. At the bottom region, the side of the cone shows higher transparency than the core. This region should be the Si redeposition layer. The deposition layer gradually becomes thinner towards the tip. Also, black lines, which mean the high density of Mo, can be observed under the redeposition layer other than the

profile of the cone. Limited by the resolution of the EDX device, the corresponding line of Mo was not clearly shown in figure 5.6 (c).

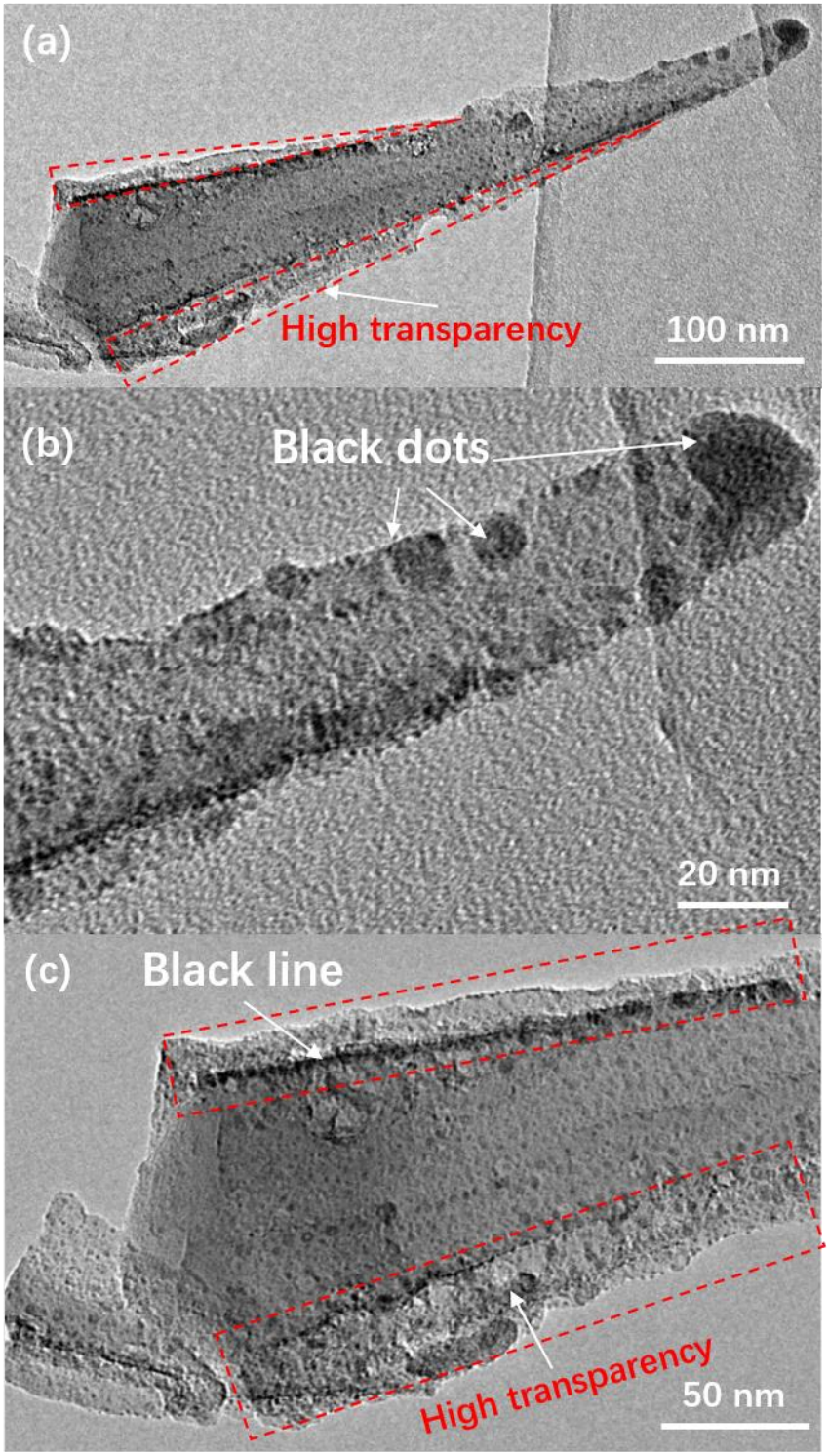

Figure 5.7 (a) TEM images of the nanocone in figure 5.6 (c). Enlarged view of tip (b) and the bottom part (c) of (a).

5.4.2 Dependence of Mo sputtering time on cone formation

To investigate the function of Mo deposition, experiments with different exposure time and deposition time were performed. For all following cases, E_{sub} is 40 eV and E_{SW} is 50 eV. In figures 5.8 (a) and (b), the surface was exposed to the He plasma for 30 and 60 min, respectively, with continuous Mo deposition. Comparing between those two cases, it can be seen that the diameter of nanocones increases from ~70 to ~140 nm as the irradiation time increase. However, when exposing the Si sample for 60 min in the plasma while the supply of Mo at only the initial 30 min, the nanostructure on the surface becomes needle-like, as shown in figure 5.8 (c). From the structure in figure 5.8 (a), growth in height and diameter (figure 5.8 (b)) occurred with Mo deposition, while they shrink and stop growing without Mo deposition (figure 5.8 (c)). Hence, we conclude that the deposition of Mo plays an important role for the cone structure to maintain the growth. Without the protection of Mo, the existed nanocone can be sputtered again. The high fraction of Mo on the tip of the cone as discussed in section 4.1 probably protects the needle structure from sputtering.

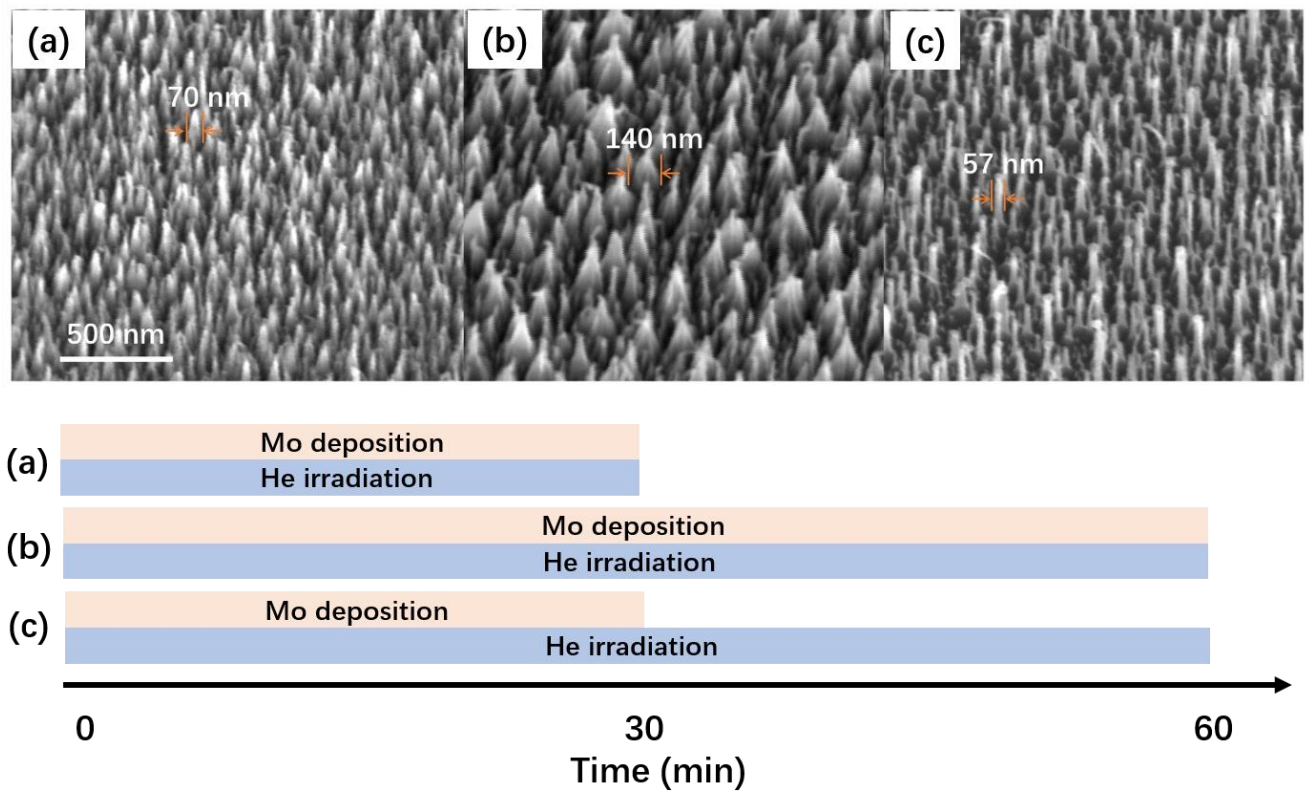

Figure 5.8 (a) Surface morphology after He irradiation with Mo deposition for 30 minutes, and (b) 60 min. (c) Surface morphology after He irradiation for 30 min with Mo deposition and another 30 min without Mo deposition. Experiment procedures for (a), (b), and (c) are shown below.

5.4.3 Discussion

Based on the Si nanocone experiments in the previous section, a schematic that explains the function of Mo co-deposition and how it affects the aspect ratio of nanocone is shown in Figure 5.9. Figure 5.9 (a) shows the co-deposition process of Mo ions and atoms. The deposited Mo will diffuse on the Si surface and eventually aggregate at the position probably with a high surface potential well determined

by the local crystal structure [29]. The high density of Mo observed on the tip of the cone (figure 5.7) was considered as the shield formed initially and cause the formation of nanocone due to the preferential sputtering. Moreover, a numerical study demonstrated the formation of nanocone based on this shielding effect [30].

Figure 5.9 (b) shows the difference of the nanocone "growth" process at large and small $\Gamma_{Mo} / \Gamma_{He}$. After a short time, Δt, of He ion irradiation and Mo co-deposition, the size of the nanocone will extend in both radial (Δr) and vertical (Δh) directions. As shown in figure 5.5 (b), the aspect ratio of nanocone increases with the He ion energy. Thus, Δh is primarily depending on the sputtering effect between He ion and Si. As for the radial direction, the size of the Mo covered region will increase during the co-deposition of Mo, i.e., Δr_1 is larger than Δr_2. In fact, as shown in figure 5.8, the nanocone shrunk to a needle-like structure without a thin Mo deposition layer. That is, a structure can protrude from the surface only when it is covered by heavier impurities (Mo). Considering the angular dependence of sputtering yield of Si, protrusions will be sputtered by He ions faster than in a normal angle, and, consequently, the uncovered region will be flattened again, as shown in the "cutting off Mo" case of figure 5.9 (b). Thus, we think that Δr is determined by F_{Mo} which is affected by $\Gamma_{Mo} / \Gamma_{He}$. When increasing $\Gamma_{Mo} / \Gamma_{He}$, Δr increases, and consequently, the aspect ratio of nanocone decreases, as shown in figure 5.9(c).

The distribution of Mo, which shows a high fraction on the tip and a low fraction at the bottom of the cone, observed in section 4.1 can be explained by the surface diffusion and accumulation of the deposited Mo as discussed above. Moreover, surface diffusion of tungsten was considered as one of the mechanisms of the tungsten fuzzy structure growth [31]. Thus, the surface diffusion of Mo also results in the growth of fiber form structure on the tip of the cone as we observed in figure 5.4. Another reason for the lower Mo fraction at the bottom is the redeposition of the sputtered Si from the surface. Line-of-sight redeposition, as shown in figure 4.6 usually occurred in sputtering processes on a rough surface [32]. Because the size of the cone tip is too small for particles to meet, redeposition, leading to reduce the concentration of Mo, mainly occurs at the bottom of the cone. Because the fraction of deposited Mo is smaller than 0.2 on the most region of Si nanocone as shown in figure 5.6. Considering that the He ion energy (40 eV) on Si sample was too small to sputter Mo, the redeposition of Mo can be ignored. A Monte-Carlo simulation of Si nanocone formation based on the shielding effect model has been conducted in our recent work [30]. Sputtered Si atoms could be traced after they were sputtered by He ions until the Si atoms redeposited on the surface or leave the simulation region. Compared with a non-redeposition case, the diameter of the cone distinctly increased at the bottom region, however, barely changed at the top region. This feature is in agreement with the observation of the redeposition layer in figure 5.7.

There are still some questions remains unsolved. For example, the height of nanocones as a function of $\Gamma_{Mo} / \Gamma_{He}$ in figure 5.5 (a) shows quite different tendency at different E_{sub}. In the shielding effect model above, the height of cone mainly depends on the different sputtering yield between the tip and the surrounding region of the cone. This difference probably related to multiple factors such as Mo flux, temperature affected surface diffusion, and ion energy. Investigation of the linear dependence in figure 5.5 (b) can help to understand the behavior of Mo on the Si surface. It is of interest to evolve an equation to find the parameters which control the aspect ratio quantitively in the future work.

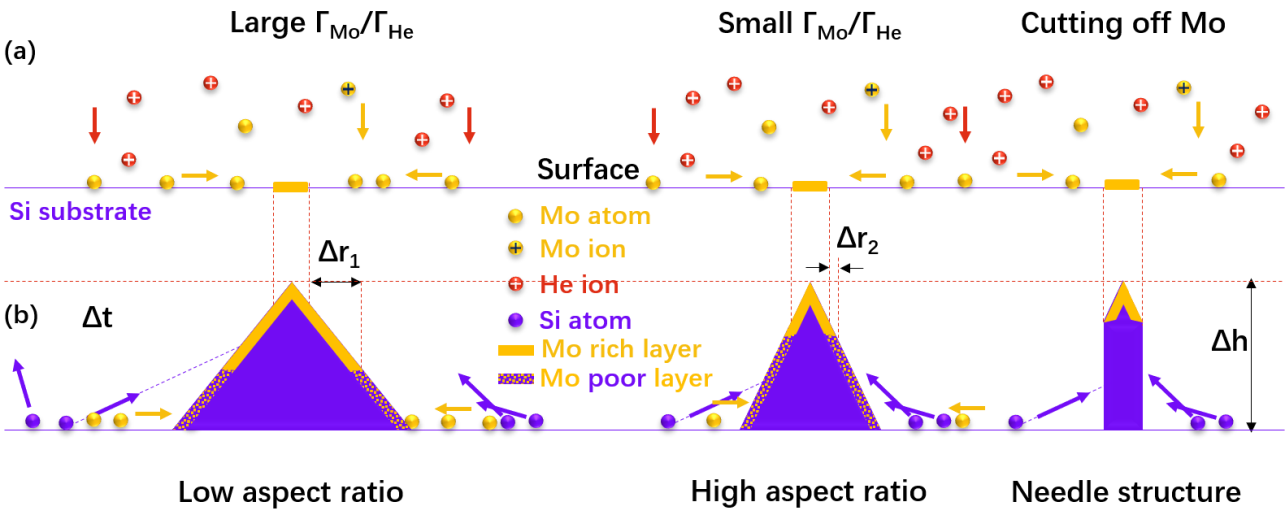

Figure 5.9 Schematic of the Si nanocone formation process for low and high aspect ratio and needle structure cases.

5.5 Optical characterization

The ability of antireflection of the Si surface is of primary concern for the industrial application. The reflectance for the nine cases in section 5.3.2 at the wavelength from 200 to 800 nm are shown in figures 5.10 (a), (b), and (c). Figure 5.10 (a) exhibits the reflectance of Si and Mo in the handbook [33, 34]. Samples at E_{sub} = 40 eV (figure 5.10 (c)) suppress the optical reflectance to ~2% through the whole wavelength range. From figure 5.10 (a), there are two characteristic peaks (at ~280 and ~360 nm) of the reflectance for Si, which resulted from the low carrier density compared with metal. However, those peaks disappeared when E_{SW} was 50 eV and 40 eV in figure 5.10 (c) and 50 eV in figure 5.10 (d). This is because nanocones on those three cases were heavily covered by Mo. Those cases are of the highest three $\Gamma_{Mo} / \Gamma_{He}$, larger than 5×10^{-5} in figure 5.5 (a). Comparing between the nine cases, the effect of the amount of Mo deposition on the reflectance did not show a consistent tendency. Here, the reflectance with the characteristics of the nanocone was not determined by the Mo amounts.

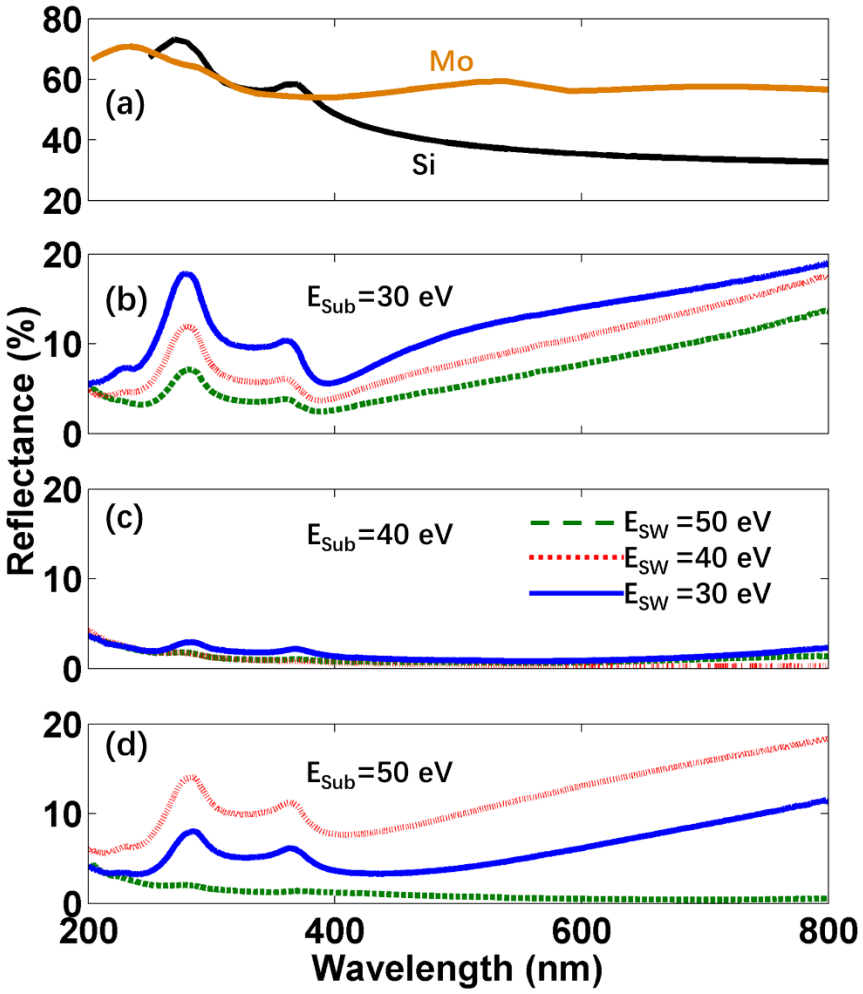

Figure 5.10 (a) The Reflectance of Si (black line) and Mo (brown line) in the handbook value at the light wavelength from 200 to 800 nm [33]. Reflectance of Si samples with E_{SW} at 50 eV (green dash line), 40 eV (red dotted line), and 30 eV (blue solid line) when E_{sub} is 30 eV (b), 40 eV (c), and 50 eV (d), respectively, at the light wavelength from 200 to 800 nm.

Figure 5.11 (a) shows the reflectance of those nine cases at the wavelength of 370 nm as a function of the average height and the aspect ratio of nanocone. When the average height of the nanocone is larger than 400 nm and the aspect ratio is smaller than 5, the reflectance is low (< 2%). Generally speaking, structures with a high aspect ratio are easier to trap the light. Figure 5.11 (b) shows the reflectance at various wavelength as a function of the diameter of nanocones. As the diameter of the cone decreases from ~170 to ~40 nm, the reflectance significantly increases 1.5, 2.5, and 7.5 times at the wavelength of 250, 370, and 800 nm, respectively. In other words, if the cone is smaller than the wavelength, the ability of the cone to trap the light is weak. This is because the objects can be considered optically flat for the light when the size is too small. In conclusion, the diameter of the nanocone on the surface is a dominant parameter on the influence of the reflectance. When the diameter of the cone is large enough to affect the optical wave, a higher cone performs better on the light trapping.

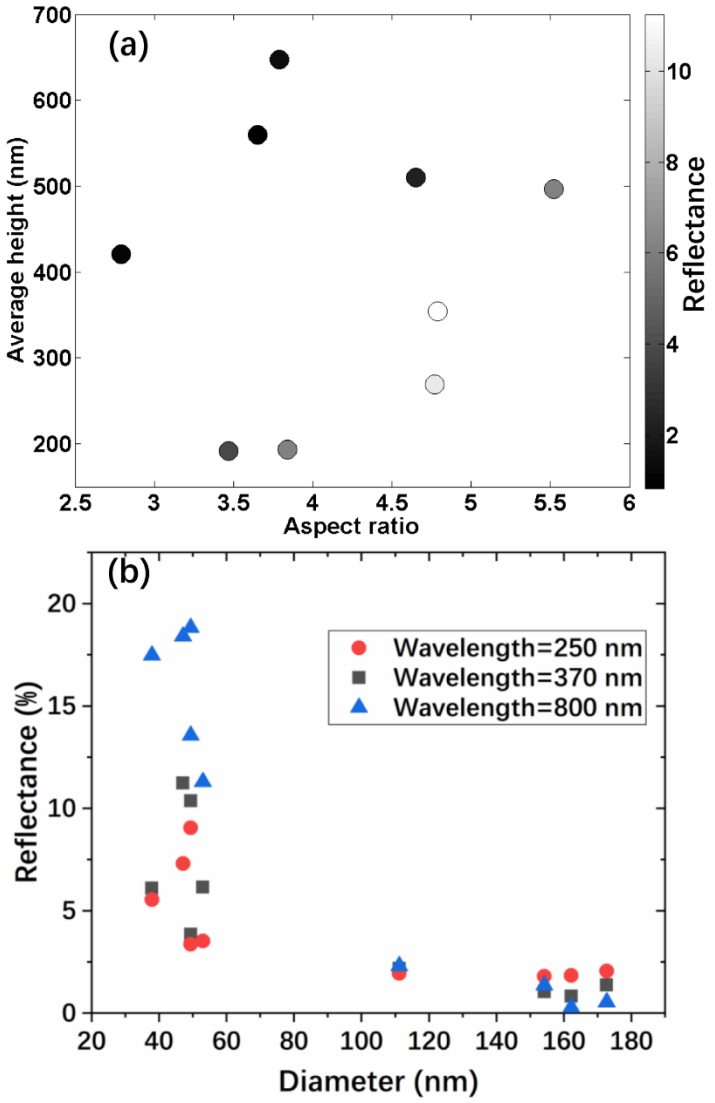

Figure 5.11 (a) The reflectance of surfaces with various heights and aspect ratios of nanocone at the light wavelength of 370 nm. (b) The reflectance of surfaces as a function of the nanocone diameter at the light wavelength of 250 (red circle), 370 (black rectangle), and 800 nm (blue triangle).

5.6 Conclusions

Uniform black silicon can be fabricated by He plasma irradiation with the co-deposition of Mo. Mo deposited on the Si surface was sputtered from a biased wire and quantified by a spectrometer. By changing the ion energy loaded on Mo wire, E_{SW}, and the Si sample, E_{sub}, different features of nanocone surface was obtained. When increasing the ratio of Mo flux, $\Gamma_{Mo} / \Gamma_{He}$, the aspect ratio of the nanocone will linearly decrease.

To investigate the relation between the aspect ratio of nanocone and $\Gamma_{Mo} / \Gamma_{He}$, EDX mapping was applied on high and low $\Gamma_{Mo} / \Gamma_{He}$ cases. The fraction of Mo, F_{Mo}, was found large at the tip region of the nanocone and small on the bottom. At the tip region, F_{Mo} was larger (0.8) when $\Gamma_{Mo} / \Gamma_{He}$ was high. The high F_{Mo} region on the tip of the cone was also confirmed in TEM images. Moreover, a Si redeposition layer was observed on the bottom and gradually became thinner towards the tip. This phenomenon was

explained by our previous numerical work based on the line-of-sight redeposition. When cutting off the Mo co-deposition during the middle of plasma irradiation, nanocones formed in the former half time cannot grow larger but was sputtered into a needle-like structure. It was suggested that the formation of different aspect ratio of nanocones is affected by F_{Mo} which determined by Γ_{Mo} / Γ_{He}. Larger F_{Mo} will protect larger area of Si from sputtering and consequently lead to a larger diameter of the nanocone formation. On the other hand, the height of the nanocone mainly depends on E_{sub}. Thus, at the same E_{sub}, a high Γ_{Mo} / Γ_{He} will lead to the formation of low aspect ratio nanocone.

Although Si has a natural high reflectance in the visible light region, the reflectance was significantly suppressed by the nanocone morphology. Especially when the height of nanocones larger than 400 nm and the diameter of nanocones larger than 100 nm the optical reflections smaller than 2%. Because when the diameter of nanocones close to or greater than the wavelength of light, the the geometry of nanocone should be taken into account. Reflection of light is suppressed by the multireflection between cone sturctures.

References

[1] J. Oh, H. C. Yuan, & H. Branz, An 18.2%-efficient Black-silicon Solar Cell Achieved through Control of Carrier Recombination in Nanostructures, Nature Nanotech **7** (2012) 743–748.

[2] Marcel Di Vece, 3-Cluster-assembled Devices for Solar Energy Conversion, Frontiers of Nanoscience **25** (2020) 59–86.

[3] S. A. Guerrera, & A. I. Akinwande, Nanofabrication of Arrays of Silicon Field Emitters with Vertical Silicon Nanowire Current Limiters and Self-aligned Gates, Nanotechnology **27** (2016) 295302.

[4] Q. Wang, J. J. Li, Y. J. Ma, X. D. Bai, Z. L. Wang, P. Xu, C. Y. Shi, B. G. Quan, S. L. Yue, & C. Z. Gu, Field Emission Properties of Carbon Coated Si Nanocone Arrays on Porous Silicon, Nanotechnology **16** (2005) 2919–2922.

[5] H. Savin, P. Repo, G. von Gastrow, P. Ortega, E. Calle, M. Garin, & R. Alcubilla, Black Silicon Solar Cells with Interdigitated Back-contacts Achieve 22.1% Efficiency, Nature Nanotech **10** (2015) 624–628.

[6] H. Jansen, M. de Boer, R. Legtenberg, & M. Elwenspoek, The Black Silicon Method: A Universal Method for Determining the Parameter Setting of a Fluorine-based Reactive Ion Etcher in Deep Silicon Trench Etching with Profile Control, Journal of Micromechanics and Microengineering **5** (1995) 115–120.

[7] D. Payne, M. Abbott, A. C. Lopez, Y. Zeng, T. H. Fung, K. McIntosh, J. Cruz-Campa, R. Davidson, M. Plakhotnyuk, & D. Bagnall, Rapid Optical Modelling of Plasma Textured Silicon, In the 33rd European Photovoltaic Solar Energy Conference and Exhibition **2CV.2.48** (2017) 897–901.

[8] M. Plakhotnyuk, R. S. Davidson, M. S. Schmidt, R. Malureanu, E. Stamate, & O. Hansen, Lifetime of Nano-structured Black Silicon for Photovoltaic Applications, In the 32nd European Photovoltaic Solar Energy Conference and Exhibition **2AV.2.34** (2016) 764–767.

[9] R. S. Davidson, H. Li, A. To, X. Wang, A. Han, J. An, J. Colwell, C. Chan, A. Wenham, M. S. Schmidt, A. Boisen, O. Hansen, S. Wenham, & A. Barnett, Black Silicon Laser-doped Selective Emitter Solar Cell with 18.1% Efficiency, Solar Energy Materials and Solar Cells **144** (2016) 740–747.

[10] M. Steglish, T. Kasebier, M. Zilk, T. Pertsch, E.-B. Kley, & A. Tunnermann, The Structural and Optical Properties of Black Silicon by Inductively Coupled Plasma Reactive Ion Etching, Journal of Applied Physics **116** (2014) 173503.

[11] Y. Xia, B. Liu, J. Liu, Z. Shen, C. Li, A Novel Method to Produce Black Silicon for Solar Cells, Solar Energy **85** (2011) 1574–1578.

[12] J. Li, H. Y. Yu, Y. Li, F. Wang, M. Yang, & S. M. Wong, Low Aspect-ratio Hemispherical Nanopit Surface Texturing for Enhancing Light Absorption in Crystalline Si Thin Film-based Solar Cells, Applied Physics Letters **98** (2011) 021905.

[13] T. H. Her, R. J. Finlay, C. Wu, S. Deliwala, & E. Mazur, Microstructuring of Silicon with Femtosecond Laser Pulses, Applied Physics Letters **73** (1998) 1673–1675.

[14] M. Tanemura, H. Yamauchi, Y. Yamane, T. Okita, & S. Tanemura, Controlled Fabrication of Mo-seeded Si Microcones by Ar^+-ion Bombardment, Nuclear Instruments and Methods in Physics Research Section B: Beam Interactions with Materials and Atoms **215** (2004) 137–142.

[15] S. Takamura, Y. Kikuchi, K. Yamada, S. Maenaka, K. Fujita, & Y. Uesugi, Nanostructure Formation on Silicon Surfaces by Using Low Energy Helium Plasma Exposure, Japanese Journal of Applied Physics **55** (2016) 120301.

[16] M. Thompson, Q. Shi, S. Kajita, N. Ohno, & C. Corr, Effect of Temperature and Incident Ion Energy on Nanostructure Formation on Silicon Exposed to Helium Plasma, Plasma Process Polym **17** (2020) e2000126.
[17] S. Takamura, T. Aota, H. Iwata, S. Maenaka, K. Fujita, Y. Kikuchi, & Y. Uesugi, Black Silicon with Nanostructured Surface Formed by Low Energy Helium Plasma Irradiation, Applied Surface Science **487** (2019) 755–765.
[18] M. Thompson, L. Magyar, & C. Corr, Nanoscale Modification of Silicon and Germanium Surfaces Exposed to Low-energy Helium Plasma, Scientific Reports **9** (2019) 10099.
[19] Y. Qiu, H. C. Hao, J. Zhou, & M. Liu, A Close to Unity and All-solar-spectrum Absorption by Ion-sputtering Induced Si Nanocone Arrays, Optics Express **20** (2012) 22087–22094.
[20] Q. Shi, S. Kajita, N. Ohno, M. Tokitani, D. Nagata, & S. Y. Feng, The Influence of Impurities on the Formation of Nanocone Structures on Silicon Surface Irradiated by Low Energy Helium Plasma, Journal of Applied Physics **128** (2020) 023301.
[21] S. Kajita, K. Asai, N. Ohno, H. Tanaka, N. Yoshida, D. Nagata, & M. Yajima, Helium-W Co-deposition Layer: TEM Observation and D Retention, Journal of Nuclear Materials **540** (2020) 152350.
[22] K. Asai, N. Yoshida, N. Ohno, S. Kajita, H. Tanaka, M. Yajima, & D. Nagata, Microstructure and Retention in He-W Co-Deposition Layer, Plasma and Fusion Research: Rapid Communication **15** (2020) 1201004.
[23] S. Kajita, S. Kado, A. Okamoto, & S. Tanaka, Application of Eclipse Laser Photodetachment Technique to Electron Sheath Thickness and Collection Region Measurements, Physical Review E **70** (2004) 066403.
[24] A. Okamoto, S. Kado, Y. Iida, & S. Tanaka, Comparison of Langmuir Probe and Laser Thomson Scattering Methods in the Electron Temperature Measurement in Divertor Simulator MAP-II, Contributions to Plasma Physics **46** (2006) 416–421.
[25] H. P. Summers, Atomic Data and Analysis Structure-User Manual, Rep. JET-IR (94), JET Joint Undertaking, Abingdon, 1994.
[26] S. Kajita, T. Tsujihara, M. Aramaki, H. Meiden, H. Oshima, N. Ohno, H. Tanaka, R. Yasuhara, T. Akiyama, K. Fujii, & T. Shikama, Behavior of 2^3S Metastable State He Atoms in Low-temperature Recombining Plasmas, Physics Plasmas **24** (2017) 073301.
[27] M. W. Thompson, The Energy Spectrum of Ejected Atoms during the High Energy Sputtering of Gold, Philosophical Magazine **18** (1968) 377–414.
[28] K. Miyaguchi, S. Kajita, H. Tanaka, & N. Ohno, Fabrication of Nanostructure Ti Thin Film with Ti Deposition in He Plasma, Japanese Journal of Applied Physics **60** (2021) 038004.
[29] S. M. Rossnagel, Effects of Surface Impurities and Diffusion on Ion Bombardment-Induced Topography Formation. In: G. Kiriakidis, G. Carter, J. L. Whitton, (Eds.) Erosion and Growth of Solids Stimulated by Atom and Ion Beams, NATO ASI Series (E: Applied Sciences) **112** Springer: Dordrecht, 1986.
[30] Q. Shi, S. Kajita, S. Y. Dai, S. Y. Feng, & N. Ohno, Modeling of the Impurity-induced Silicon Nanocone Growth by Low Energy Helium Plasma Irradiation, Plasma Science and Technology **23** (2021) 045503.
[31] S. Kajita, W. Sakaguchi, N. Ohno, N. Yoshida, & T. Saeki, Formation Process of Tungsten Nanostructure by the Exposure to Helium Plasma under Fusion Relevant Plasma Conditions, Nuclear Fusion **49** (2009) 095005.
[32] D. Hwangbo, S. Kajita, N. Ohno, P. McCarthy, J. W. Bradley, & H. Tanaka, Growth of Nano-tendril Bundles on Tungsten with Impurity-rich He Plasmas, Nuclear Fusion **58** (2018) 096022.

[33] M. A. Green, & M. J. Keevers, Optical Properties of Intrinsic Silicon at 300 K, Progress in Photovoltaics: Research and Applications **3** (1995) 189–192.

[34] D. W. Lynch, & W. R. Hunter, Comments on the Optical Constants of Metals and an Introduction to the Data for Several Metals, In: E. D. Palik, Editor(s), Handbook of Optical Constants of Solids, Academic Press, 1985, 275–367.

Chapter 6. Conclusions and future works

6.1 Conclusions

The main purpose of this thesis is to understand mechanism of the impurity-induced silicon (Si) nanocones formation with the helium (He) plasma irradiation and fabricate it in a controlled manner to meet the requirement of industrial applications, such as high aspect ratio of cone structures and low reflectance of Si surface.

In this thesis, Si samples were exposed in He plasma. Two typical surface morphologies have been observed on Si surfaces: small (~0.01 μm^2) and high density of nanocones with low (~2%) optical reflectance (black Si), and large (~0.1 μm^2) and low density nanocones with relatively high (~40%) optical reflectance (white Si). After the surface analyzation by X-ray photoelectron spectroscopy (XPS), amount of impurities which deposit on the surface is the key factor which cause the different morphology. A large amount of impurities lead to the formation of black Si. The real sputtering yield, calculated via the erosion depth, of black Si was less than half of that of white Si. This indicated that the formation of nanocones is attribute to the shielding effect of deposited molybdenum (Mo) impurities during the ion bombardment. Observations on nanocone through transmission election microscope (TEM) revealed that low energy He plasma irradiation remains the Si nanocones and the substrate good crystalline structure.

In order to concrete the theory above, a numerical work has been developed with SURO code based on the energy dispersive spectroscopy (EDS) mapping result on a single Si nanocone. The formation process of the nanocone from a flat surface was presented. The modeling structure under an inclining ion incident direction was in good agreement with the experimental result. Moreover, the redeposition effect due to the line-of-sight was proposed as another important process of nanocone formation based on results from the comparison of the cone diameter and sputtering yield between cases with and without the redeposition effect. Increasing of the density of nanocone on the simulation region enhanced this redeposition effect.

Furthermore, a biased Mo sputtering wire was introduced in front of the Si substrate during the plasma irradiation. Uniform black Si can be easily obtained with this method at surface temperature of 500 °C and ion fluence of 2.5×10^{25} m^{-2}. Mo impurity fluxes have been quantified through the intensity of the Mo emission light. Plasma irradiation experiments were conducted under different He ion energies on the sputtering wire E_{SW} and the Si substrate E_{sub}. It was found that the averaged aspect ratio (height over diameter of cone) of nanocones has a linear dependence on the logarithm of Mo flux ratio. The slope of this linear dependence is almost constant at different E_{sub}. The reason of this relationship is strongly related with the fraction of Mo on the upper region of the cone according to the observation in EDS for different aspect ratio cases. With the assistant of TEM images of a single nanocone, the high fraction of Mo was clearly identified as black dot on the tip of cone. Moreover, a layer on the side of the bottom of the cone with high transparency was observed. This layer had the same features as the redeposition layer founded in the simulation work above. Nanostructures on the irradiated surface were also compared between a full time Mo deposition case and a half time case. The usual cone structure shrunk to needle-like structure after the Mo deposition was cut off. This phenomenon indicated that protrusion on the Si surface without the coverage of Mo can be flattened again due to the angular dependence of sputtering yield. Besides, nanocones structure with the height larger than 400 nm and the diameter larger than 100 nm contribute to the suppression of reflection smaller than 2%. Thus, the optical reflection on Si surface can be controlled by controlling the flux of deposited Mo and the incident ion energy on Si substrate.

6.2 Future works

This thesis presents numerous works to demonstrate the influence of impurity deposition on the formation of cone structure on the Si surface. However, other parameters also should be investigated systematically. Mechanism of the Si nanocone formation involves some vital hypotheses which should be verified. Thus, research contents which is expected to be conducted in the future are proposed below:

(1) Considering that surface diffusion is one of the mechanisms of cone formation, effect of surface temperature, which relevant to the energy of surface diffusion, will be investigated in a wider temperature range and systematic method.
(2) The formation of Mo cluster by the agglomeration of Mo atoms on the Si surface is a crucial hypothesis of the mechanism. It is of interest to find an evidence of the present of Mo cluster on the Si surface in the future. One method is to observe the Si surface with short exposure time before the cone structure was formed by EDS mapping.
(3) The simulation model in SURO code is relatively simple. A dynamic model which can involve the behaviors of Mo atoms form deposition to agglomeration is expected to be developed in the future.
(4) Test of the performance of the Si sample with nanocone structure for the industrial application such as solar photovoltaic cell will be carried out in the future.

Acknowledgement

My time at the Graduate School of Engineering will soon come to an end, and I would like to express my sincere gratitude to those who have helped me during my Ph.D study at Nagoya University. This work could not have been completed without their help.

Particular appreciation goes to my supervisors, Professor Kajita Shin and Professor Ohno Noriyasu, not only for their guidance on academic research, but also for the help and constructive suggestions in life. They give me generous guidance in selecting the topic, designing the research, analyzing experiment data, settling problems, and writing the final thesis. Professor Kajita Shin's dynamism, rigorous academic vision, motivation, and rich achievements have deeply inspired me. He has taught me the methodology to carry out the research and to present the works as clearly as possible. And Professor Ohno Noriyasu has provided plenty of valuable advice on my research and research career. I am grateful to Dr. Tanaka Hirohiko for his helpful suggestions. I also want to thank Professor Ishikawa, Professor Ichino, Professor Nakamura for the review of this thesis.

Secondly, I wish to express my gratitude to Takagi Makoto and Dr. Kuwabara Tatsuya who have offered great help in operating and repairing the experimental equipment which is extremely useful in my research.

Moreover, I would like to show my appreciation to my lab members for raising constructive suggestions to improve my research and for their help in the completion of my study. Thanks to my tutor Asai Kosuke, who gave me generous help when I first arrived at Nagoya. He has supported me to adapt to the new life here and integrate quickly into the research group. I am deeply grateful to Shuangyuan Feng, she has supported me in both research and daily life.

Additionally, I wish to extend my special thanks to the China Scholarship Council for their funding in supporting my research and life here in Japan.

Last but not the least, I would like to thank my parents for their unwavering love and support for all my decisions, and my girlfriend Xichu Zhu for her understanding, encouragement and accompany in my life.

List of Publications

1. Quan Shi, Shin Kajita Shuangyuan Feng, Noriyasu Ohno, "The dependence of Mo ratio on the formation of uniform black silicon by helium plasma irradiation", ***Journal of Physics D: Applied Physics***, Vol. 54, No.405202, July, 2021

2. Quan Shi, Shin Kajita, Shuyu Dai, Shuangyuan Feng, Noriyasu Ohno, "Modeling of the impurity-induced silicon nanocone growth by low energy helium plasma irradiation", ***Plasma Science and Technology***, Vol. 23, No. 045503, pp. 6, March, 2021

3. Quan Shi, Shin Kajita, Noriyasu Ohno, Masayuki Tokitani, Daisuke Nagata, Shuangyuan Feng, "The influence of impurities on the formation of nanocone structures on silicon surface irradiated by low energy helium plasma", ***Journal of Applied Physics***, Vol. 128, No. 023301, July, 2020

4. Quan Shi, Shuyu Dai, Dezhen Wang, "3D Modelling of tungsten fuzz growth under the bombardment of helium plasma", ***Fusion Engineering and Design***, Vol. 136, pp. 554-557, April, 2018

5. Quan Shi, Shuyu Dai, A. Kirschner, Dezhen Wang, "Numerical and analytic study of rough surface morphology on the angular distribution of eroded impurity", ***Contributions to Plasma Physics***, Vol. 57, pp. 329-335, August, 2017

6. Matt Thompson, Quan Shi, Shin Kajita, Noriyasu Ohno, Cormac Corr, "Effect of temperature and incident ion energy on nanostructure formation on silicon exposed to helium plasma", ***Plasma Processes and Polymers***, Vol. 17, No. 2000126, September, 2020

7. S.Y. Dai, K.R. Yang, D.H. Liu, Q. Shi, B. Cui, S.G. Liu, D.Z. Wang, "Impacts of impurity flux on erosion and deposition of carbon/tungsten rough surfaces", ***Nuclear Materials and Energy***, Vol. 26, No. 100802, October, 2020

8. Shuyu Dai, Y.P. Wang, Q. Shi, M. Wang, T. Xie, B. Liu, B. Cui, D.Z. Wang, "Effects of tungsten and carbon rough surfaces on the material mixing and impurity erosion/deposition", ***Fusion Engineering and Design***, Vol. 136, pp. 897-901, April, 2018

9. Shuyu Dai, M. Kobayashi, G. Kawamura, Q. Shi, Y. Feng, D.Z. Wang, "Effects of varying stochastic layer on edge plasma and impurity transport in 3D EMC3-EIRENE simulations of LHD", ***Fusion Engineering and Design***, Vol. 125, pp. 625-630, April, 2017

International Conference Presentations

(1) *13th International Symposium on Advanced Plasma Science and its Applications for Nitrides and Nanomaterials* **(ISplasma)**, Online, Mar. 2021. Oral

(2) *12th International Symposium on Advanced Plasma Science and its Applications for Nitrides and Nanomaterials* **(ISplasma)**, Online, Mar. 2020. Oral

(3) *The 28th International Toki Conference on Plasma and Fusion Research* **(ITC28)**, Toki, Japan, Nov. 2019. Poster

(4) *17th International Workshop on Plasma Edge Theory in Fusion Devices* **(PET)**, La Jolla, CA, USA, Aug. 2019. Poster

(5) *4th International Workshop on Models and Data for Plasma-Material Interaction in Fusion Devices* **(MoD-PMI)**, Toki, Gifu, Japan, Jun. 2019. Poster

(6) *13th International Symposium on Fusion Nuclear Technology* **(ISFNT)**, Kyoto, Japan, Sep. 2017. Poster